UNIVERSITY CARLOS III OF MADRID

School of Engineering

Doctor of Philosophy

Dual Scale Flow during Vacuum Infusion of Composites: Experiments and Modelling

by Joaquim Vilà Bramon

A thesis submitted for the degree of Doctor of Philosophy in the

Department of Material Science and Engineering and Chemical Engineering

2015

Doctoral Thesis

Dual Scale Flow during Vacuum Infusion of Composites: Experiments and Modelling

Author:
Joaquim Vilà Bramon

Supervisors:
Dr. Carlos González
Dr. Javier Llorca

Signatures of committee members:

President: Dr. Ion Aurrekoetxea Narbarte

Vocal: Dr. Drapier Sylvain

Secretary: Dr. Jon M. Molina-Aldareguia

Qualification:

Leganés, December 10^{th} of 2015

Dedicated to my family, specially to my sisters Laura and Vanessa Vilà for supporting me unconditionally and to my friend Gerard Roca

Abstract

Vacuum-assisted resin infusion has emerged in recent years as one of the most promising techniques to manufacture fiber-reinforced polymer-matrix composites. This open mold process uses vacuum as the driving force to infiltrate resin through a bagged fiber preform, leading to reduced tooling costs, as compared with the traditional closed mold process (resin transfer molding). In addition, large components can be produced with this technique. However, manufacturing defect-free components by means of vacuum-assisted resin infusion is not guaranteed due to complexity of the infiltration process and to the intricacies associated with the presence of a flexible bag. In addition, the final thickness of components manufactured by this process is not constant due to both the flexible bag and to the stress partition between the fiber bed and the fluid, leading to a greater thickness near the inlet port than near the vent.

This thesis is a contribution to understand the phenomena that control vacuum-assisted resin infusion at the mesoscopic and microscopic scales. The mesoscopic behavior was studied by means of an experimental set-up allows the use of a distribution medium on top of the fiber preform to account for in-plane and through-the thickness infiltration. Fluid pressure was measured by means of pressure gages at different locations and the evolution of the out-of-plane displacement of the vacuum bag (due to changes in the fabric compaction) was continuously measured by means of the digital image correlation. In addition, infusion at the microscale was analyzed by means of *in situ* infiltration experiments carried out in the synchrotron beam to study the mechanisms of microfluid flow and void transport within a fiber tow by means of synchrotron X-ray computer tomography using an apparatus designed and built for this purpose. This information was used to develop a level set based model to simulate fluid flow and fabric compaction during vacuum-assisted infusion. Fluid infusion through the fiber preform was modeled using Darcy's equations for the fluid flow through a porous media. The stress partition between the fluid and the fiber bed was included by means of Terzaghi's effective stress theory. These equations are only valid in the infused region and both regions (dry and wet) were separated by introducing a level set function in the partial differential equation which is defined at any given time as the distance to the flow front. Finally, the model predictions were validated against the experimental results.

Acknowledgements

First of all, I would like to express my gratitude to Prof. Josep Costa from the University of Girona who suggested this PhD to me; without his advice, this work would not even exist. I also extend my gratitude to my supervisors Prof. Javier Llorca and Prof. Carlos González for their academic support; specially to Carlos, with whom I spent a lot of time enjoying the best and the worst of science. It has been a pleasure to work with them and to work in an outstanding international environment at IMDEA Materials Institute.

I am thankful to the people of the Center for Composite Materials, University of Delaware, where I did my internship and started my PhD. Especially to my supervisor there, Prof. Dirk Heider, who helped me throughout my stage and to all my colleagues, particularly Chris Arvanite and Anton Kovalchuk for the time we enjoyed traveling together. I have special memories of my american friend Kalon Lasater, with whom I shared interests and hobbies like trial-bikes. I am glad to have met Becca Moscowitz my housemate and her boyfriend Mark Templeton who was a soccer-freak and a good player, as well.

During the beam-times in Hamburg, the support of Ricardo Fernández Gutiérrez, Hangbo Yue, Gabor Szakacs and Robert Koos is gratefully acknowledged. I enjoyed working together non-stop in the beam-line P05 of Petra III with this team and Dr. Federico Sket.

I would like to extend my gratitude to the people of IMDEA Materials Institute, especially to the people that I started with, when we were like a family. We arranged snow trips with Rafael Soler, Marcos Rodriguez, Covadonga Rosado and her husband Olivier and Claudio Lopes, and a Salamanca trip with Rocio Muñoz, Raul Muñoz and Francisca Martinez. The unforgettable discussions about politics in Madrid with Michalis Agoras and Alexis Charalambides and the "cuñañas break" with Hangbo Yue and Alex Garcia. It has been a pleasure to work with Vanesa Martínez, Juan Carlos Rubalcaba and Jose Luis Jiménez, who are really professional technicians. I am also glad to have been working with Dr. Federico Sket who is a top expert in tomography and who gave me the opportunity to work with the leading edge technology of the synchrotron beam. Finally, I am also thankful to a very impressive personal and professionally fellow, and also one of the best mathematician that I have never met, Sergio Sádaba.

I appreciate the interaction with the people of the University of Mondragón, Jon Aurrekoetxea, Iñigo Ortiz and Maider Baskaran. They are really professional and friendly people. It has been a pleasure also to share this time with Roberto Guzman, who is a really networking guy and who was one of the first PhD students of composites in Spain.

I am grateful to all the friends that I have made in Madrid during my PhD. Of those, Rodolfo Portillo was helping me constantly, and the master of universe Jesús Gil.

Special thanks to my girlfriend Tere for her unconditional emotional support during my thesis and being part of my life.

Finally I would like to thank my family for their patience especially my grandmother "iaia" Pilar Margall, who still does not understand why I need a PhD to work on the family farm. I would like to remember my grandfather Federic Vilà who passed away when I was young: he was a hard working farmer giving us all that we have at "casa la iaia" farm, which the 3rd generation will enjoy forever. And naturally my parents Joaquim Vilà Margall and Aurora Bramon Vilarnau.

Contents

List of Figures

List of Tables

Abbreviations

AFP	**A**utomated **F**iber **P**lacement
AOI	**A**rea **O**f **I**nterest
ATL	**A**utomated **T**ape **L**aying
CCD	**C**harge **C**oupled **D**evice
C-RTM	**C**ompression **R**esin **T**ransfer **M**olding
DAS	**D**ata **A**dquisition **S**ystem
DESY	**D**eutsches **E**lektronnen **SY**nchrotron
DIC	**D**igital **I**mage **C**orrelation
DM	**D**istribution **M**edium
FOV	**F**ield **O**f **V**iew
FVF	**F**iber **V**olume **F**raction
LCM	**L**iquid **C**omposite **M**olding
LSM	**L**evel **S**et **M**ethod
LVDT	**L**inear **V**ariable **D**ifferential **T**ransformer
NCM	**N**on **C**ontact **M**ethod
NDT	**N**on **D**estructive **T**echnique
PMC	**P**olimer **M**atrix **C**omposites
PMMA	**P**oly **M**ethyl **M**etha **A**crylate
RTM	**R**esin **T**ransfer **M**olding
SXCT	**S**ynchrotron **X**-ray **C**omputed **T**omography
VARI	**V**acuum **A**asisted **R**esin **I**nfusion

VaRTM	**V**acuum **a**assisted **R**esin **T**ransfer **M**olding
VI	**V**acuum **I**nfusion
XCT	**X**-ray **C**omputed **T**omography

Physical Constants

Atmospheric pressure	p_{atm}	=	$101325[Pa]$
Fiber glass density	ρ_f	=	$2540[Kg/m^3]$
Gravity acceleration	g	=	$9.81[m/s^2]$

Symbols and Nomenclature

p	Fluid pressure	$[Pa]$
p_0	Reference vacuum pressure	$[Pa]$
p_c	Capillary pressure	$[Pa]$
L	Panel length	$[m]$
W	Panel width	$[m]$
V_f	Fiber volume fraction	$[\%]$
F	Propagation velocity of Level Set	$[m/s]$
x, y	In-plane directions	$[m]$
z	Transverse direction	$[m]$
i, j, k	Discretization indexes according to the directions x,y,z	
n	Temporal discretization index	
T_f	Filling time	$[s]$
T_p	Post-Filling time	$[s]$
h_0	Initial panel thickness	$[mm]$
h	Panel thickness	$[mm]$
N	Number of layers	
$\mathbf{v}$	Fluid velocity	$[m/s]$
$\bar{\mathbf{v}}$	Average fluid velocity	$[m/s]$
$x_0(t)$	Flow front position in x-direction	$[m]$
$r_0(t)$	Flow front position in radial direction	$[m]$
D_f	Filament diameter of fiber	$[m]$

Q_m	Fluid mass flow	$[Kg/s]$
σ_{fiber}	Fiber stress	$[Pa]$
μ	Viscosity	$[Pa \cdot s]$
ϕ	Porosity	[1]
$\phi(x,t)$	Level set function	$[m]$
$\mathbf{K}$	Permeability tensor	$[m^2]$
θ	Wetting angle between solid-liquid	$[^\circ]$
γ	Surface tension	$[mJ/m^2]$
$\Delta x, y$	Spatial increment in-plane	$[m]$
Δz	Spatial increment in transverse direction	$[m]$
Δt	Temporal increment	$[m]$
Δh	Panel thickness increment	$[m]$
∇p	Gradient of pressure	$[Pa/m]$
$\nabla \phi$	Gradient of level set function	
$\lvert\nabla \phi\rvert$	Norm of gradient of level set function	
$\nabla \cdot \mathbf{v}$	Divergence of fluid velocity	$[1/s]$
∇^+	Upwind operator	
∇^-	Downwind operator	
$D^x_{i,j}$	Forward operator for x-direction	
$D^{-x}_{i,j}$	Backward operator for x-direction	
τ	Fictitious time of reinitialization	$[s]$
$S(\phi_0)$	Sign function for reinitialization scheme	
ϵ	Parameter to smooth the sign function $S(\phi_0)$	
ρ	Fluid density	$[Kg/m^3]$
ρ_f	Fiber density	$[Kg/m^3]$
ρ_A	Areal density of fabric	$[Kg/m^2]$
$K_{\lvert\rvert}$	Longitudinal permeability	$[m^2]$
$K_\perp$	Transverse permeability	$[m^2]$

"The wind at your back". My friend Chris Arvanite

Chapter 1

Introduction

Composite materials have been used since ancient times. Adobe bricks, for instance, were manufactured in Egypt and Mesopotamia and can be considered an excellent example of the synergistic contribution of two materials, mud and straw, to improve the mechanical behavior. Nowadays, modern composite materials are increasingly used in engineering applications in many industrial sectors including aerospace, petrochemical, automotive, sports, etc.

Composites are made up with at least two different materials, the matrix and the reinforcement. The matrix is the continuous phase that binds the reinforcement together and protects the reinforcement against the external environment improving the durability. The reinforcements, either fibers or particles, carry the structural load and are primarily added to increase the stiffness and the strength. Depending on the matrix material, composite materials can be classified into either metal, ceramic and polymer matrix composites.

Metal-matrix composites are manufactured to improve the mechanical properties of metallic alloys [1]. Main objectives are to increase specific properties (stiffness and strength), hardness and mechanical behavior at high temperature [2]. In addition, metal-matrix composites with tailored properties (stiffness, electrical/thermal conductivity, coefficient of thermal expansion) are manufactured for specific applications (thermal management, very low distortion components, etc.).

Ceramic-matrix composites have been develop to overcome the inherent brittleness of ceramic materials, so they can be used in structural applications at very high temperature and in aggressive environments [3]. Current applications include cutting tools, molds, dies and extrusion cones as well as heat exchangers, hot gas valves, exhaust nozzles, combustor liners, and turbine nozzle guide vanes. Carbon-carbon composites [4] are a particular type of ceramic-matrix composites made up of a pyrolitic carbon matrix reinforced with carbon fibers. They take advantage of the unique properties of the matrix, while C-fiber reinforcement provides good mechanical properties (strength and toughness). They are used in disk brakes of airplanes and trains as well as in structural elements for very high temperature applications (rocket nozzles, thermal shields).

The main limitations of both metal- and ceramic-matrix composites can be found in the difficulties associated with the infiltration of the matrix into the reinforcement. This leads to sophisticated processing routes which increase dramatically the cost and reduce their use to a limited number of high added value applications. On the contrary, polymer-matrix composites can be easily manufactured by the infiltration of a low viscosity resin into a fiber preform. The low density of the polymeric matrix together with its excellent environmental resistance has led to the widespread use of composites for lightweight structural components many industrial sectors.

1.1 Polymer matrix composites

Two types of polymers are mainly used as matrices in composites, namely thermosets and thermoplastics. Thermoset are polymers with branched chains, they are formed in situ by a chemical reaction (curing) between two polymers (resin and hardener) or a resin and catalyst, leading to a three-dimensional network in which covalent bonds link different polymeric chains. Before curing, the resin is a low viscosity liquid at ambient temperature that can be infiltrated into the fiber preform. Once cured, thermosets do not become liquid again if heated, although their mechanical properties will decrease significantly above the glass

transition temperature, T_g, because the molecular structure changes from that of a rigid network to a flexible one. This change is reversible.

Thermosets are not expensive, present high stiffness and strength, good resistance to chemical attacks and are the standard matrices for polymer-matrix composites. They are, however, brittle and their mechanical properties decrease rapidly with temperature (particularly under hot/wet conditions). Typical thermosets used as matrices are epoxy, phenolic, polyester resins. Other thermosets (such as bismaleimides or polyamides) are used when good mechanical properties at high temperature are required.

Thermoplastics are high-molecular weight polymers whose chains are linked through weak Van der Waals bonds (polyolefins), hydrogen bonds (nylon) or even stacking of aromatic rings (polystyrene). They turn to a liquid when heated and freeze to a glassy state when cooled sufficiently and this process is reversible. Thermoplastics can have amorphous or semi-crystalline structure, alternating crystalline regions with amorphous regions in which the chains approximate random coils. They normally present higher ductility and toughness than thermosets below T_g, and both properties increase very rapidly above T_g while the strength decreases because the amorphous chains change from a glassy to a rubbery phase. Above T_m, the viscosity gradually decreases without any distinct phase change and thermoplastics become viscous liquids that can be infiltrated into fiber preforms.

Typical thermoplastics for composite manufacturing are polyolefins (polyethylene and poly propyleene), polyamides (nylon) and polysterene. Other thermoplastics (such as polyphenylene sulfide and polyether-ether-ketone) are also used for high temperature applications. Although thermoplastics present many advantages with respect to thermosets (rapid and reversible processing, reusable scrap, reparability and joining by welding, etc.), they are often more expensive and infiltration requires very high temperatures to reduce the viscosity and ensure the complete impregnation of the fiber preform.

High strength polymer-matrix composites are usually reinforced with either carbon or glass fibers. Fibers are distributed in tows or yarns (that contain several thousands of fibers)

interlaced or woven together to form a fabric that can be easily handled for manufacturing. The fabrics can be classified depending on the 2D or 3D tow architecture. 2D fabrics are the most common fabrics for structural applications and can be woven, braided or stitched depending on the requirements, (Figure 1.1). 3D fabrics are usually designed to overcome the reduced mechanical properties of standard laminates in the through-the-thickness direction.

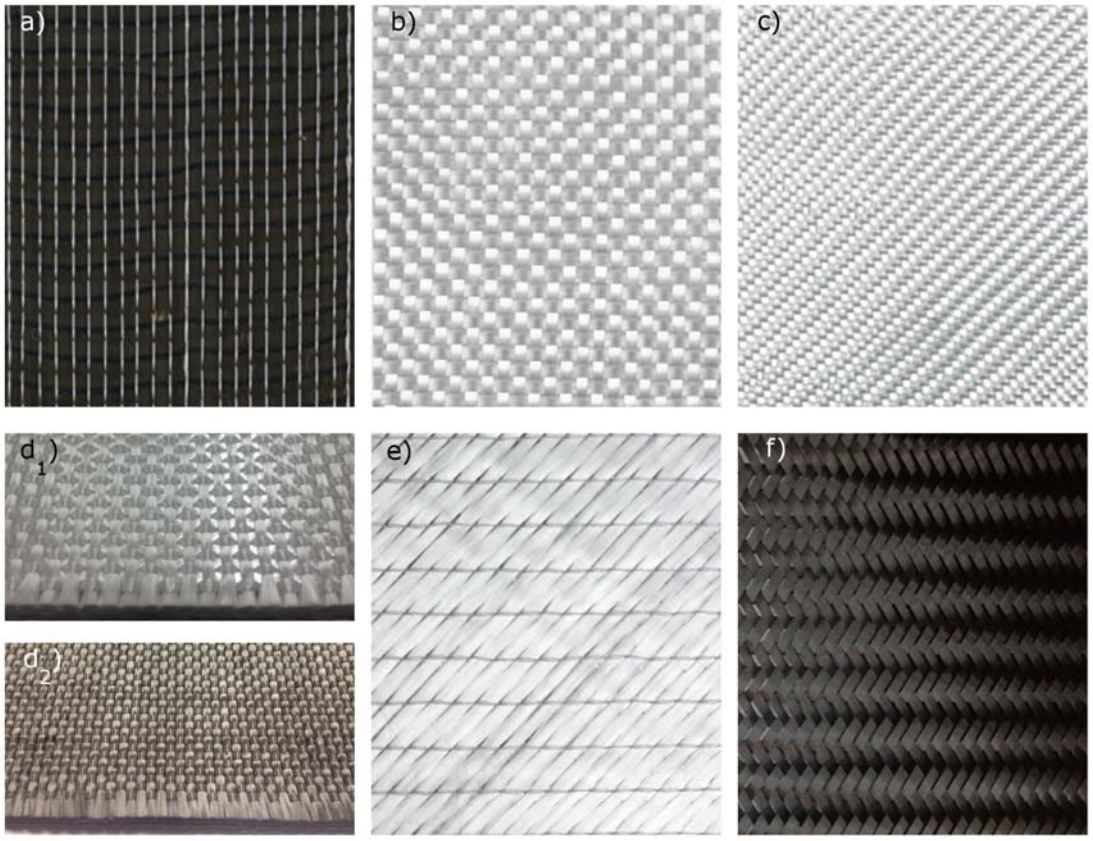

FIGURE 1.1: Different fabric architectures for the reinforcement of composites. a) unidirectional fiber tows. b) Plain woven fabric. c) Twill woven fabric. 3D woven d1) glass fiber d2) carbon fiber. e) Non-crimp fabric. f) 2D carbon triaxial braided.

Unidirectional fabrics are formed by parallel fiber tows that are slightly stitched together in the transverse direction to maintain them in position (Figure 1.1 a). The mechanical properties in the tow direction (in terms of stiffness and strength) are the highest because of the large fiber volume fraction that can be achieved but unidirectional composites are highly anisotropic because the transverse properties are mainly controlled by the matrix.

Multidirectional laminates, made up by stacking unidirectional plies with fiber different orientation, which provide a more isotropic response that can be easily tailored to meet the particular loading conditions of the structural element. Woven fabrics are made by tow weaving which is a traditional textile processing technique based on the interlacing of two sets of yarns, named warp and weft. There are many different woven fabrics. For instance, one warp tow alternately interlaces with one weft tow in a plain weave (Figure 1.1 b), whereas the weft tow passes over one and under two or more warp tows in a twill weave (Figure 1.1 c). The weave pattern influences many fabric properties, including the mechanical performance, drapability (ability of the dry fabric to adapt to complex mold shapes), and fiber volume fraction. Textile processes can also be used to manufacture 3D woven preforms (Figure 1.1 d), in which the presence of fibers in the through-the-thickness direction improves the delamination resistance of the laminate. Non-crimp fabrics are multidirectional laminates which are held in position by a secondary stitched thread called Z-yarn (Fig 1.1 e). They stand as an alternative to traditional multidirectional laminates because the fibers lay in the laminate plane following a predefined stacking sequence with slight or negligible out-of-plane undulations (non-crimped material). Finally, braiding is another textile manufacturing technique that can produce tubular or flat fabrics (Figure 1.1 f) by interlacing fibers in a spiral way. The style and size of braided fabrics depends on different variables, such as number of the yarns, their size and the braid angle that ranges from 25° to 75°[5].

The wide range of fiber preforms that can be manufactured leads to a very wide design space and the selection of the architecture of the fiber preform has to be analyzed very carefully for each application as it controls to a large extent mechanical properties of the final composite, the manufacturing route and the cost.

1.2 Overview composite processing techniques

High performance polymer-matrix composites were initially used in very high added value applications for aerospace and sports. The cost of the material (particularly the carbon fibers), together with that of the weaving and matrix infiltration can be reach as much as the 50% of the total composite part [6]. In general, manufacturing of composite materials is labor intensive and requires skilled personnel to achieve optimum results. More recently, composites started to be used in other applications in automotive, energy generation (wind turbines), petrochemical, etc. owing to the improvement of processing techniques and the use of cheaper glass fibers.

Manufacturing techniques for thermoset-based composites can be classified in two main groups, depending on the way the resin is introduced in the composite material during manufacturing: consolidation of pre-impregnated sheets (prepregs) or liquid molding. Their main features are detailed below.

1.2.1 Consolidation of prepregs

Prepregs are semi-finished products in which the dry fabric (unidirectional or woven) has been previously impregnated with the resin and maintained in a semicured stage under refrigerated conditions prior to the final stacking, assembly and consolidation of the laminate using heat and pressure, Figure 1.2. The best composite properties, provided by the highest fiber volume fraction and the minimum porosity, can be achieved by autoclave consolidation of the multidirectional or woven laminates made up by stacking prepreg sheets. Autoclaves are expensive pressure vessels with heating/cooling capabilities which allow to cure/consolidate the prepreg material under controlled pressure-temperature conditions in N_2 atmosphere to ensure the full consolidation and the evacuation of volatiles (Figure 1.3 a)). Autoclave consolidation of prepregs is currently the state-of-the-art to manufacture high performance

composites but the high capital investment capital in combination with the recurring operational costs (e.g. energy consumption, N_2, tooling, etc.) is one of the main limitations to extend the application of high-performance composite materials into other industrial sectors.

(A) (B)

FIGURE 1.2: Reinforced fabrics typically pre-impregnated with an epoxy resin a) Prepreg 3k 2x2 twill weave carbon. b) Prepreg woven carbon.

There is a large variety of products made by autoclave consolidation of prepregs ranging from tennis rackets to Formula 1 race car chassis. Small composite parts are produced by manual lay-up of the prepreg sheet, which is labor intensive and not appropriate for large components. Automated lay-up operations are preferred in this case and fuselage barrels, wing bearing surfaces, stabilizers, etc. for aerospace make use of automated lamination by means of Automatic Fiber Placement (AFP), Figure 1.3 b), and Automatic Tape Laying (ATL), Figure 1.3 c), machines. High productivity and reduced material waste are associated to ATL and AFP processes but they are still restricted to simple geometry parts with single or double curvature.

Due to the high manufacturing costs associated with the use of autoclave, there is a lot of interest in the development of prepregs that can be consolidated out of autoclave under atmospheric pressure in a vacuum bag. Nevertheless, these techniques are not fully mature, particularly for high performance applications.

(A) (B) (C)

FIGURE 1.3: a) Autoclave. b) Automatic Tape Layer (ATL) machine. c) Automatic Fiber Placement (AFP) machine.

Other techniques emerged in parallel and are intended to mitigate them. These techniques are usually covered under the umbrella of out-of-autoclave techniques (OoA) and range from special prepregs designed to cure and consolidate under vacuum bag only conditions (VBO) or liquid molding technologies in which resin is being infiltrated through the fabric preform using pressure gradients as driving forces, as in resin transfer molding (RTM) or vacuum resin infusion (VARI).

1.2.2 Liquid molding of composite materials

Manufacturing of composites by liquid molding is carried out by the infiltration of the liquid resin through the fabric preform using pressure gradients as driving forces. The most common liquid molding manufacturing processes used by the industry and their typical applications are briefly summarized below.

Injection molding is widely used for high volume production of components made up of thermoplastic polymers (with or without reinforcements) and can also be used with thermosets. In this case, resin, catalyst and chopped fibers are mixed and injected into a mold. The mixture is normally left to cure under standard atmospheric conditions. This technique is only used for low-added value applications.

During *wet or hand lay-up*, the fiber preform is lay-up into a mold and impregnated manually with the liquid resin by means of rollers or brushes. Laminates are left to cure under standard

atmospheric conditions. Wind-turbine blades, boat hulls and architectural moldings are produced by this route.

Pultrusion is a continuous process aimed at producing a continuous profile of constant cross-section. Fibers are pulled from a creel through a resin bath and then on through a heated die. The die completes the impregnation of the fiber, controls the resin content and cures the material into its final shape as it passes through the die. This cured profile is then automatically cut to length. Beams and girders used in roof structures, bridges, ladders, etc. are efficiently manufactured by pultrusion.

Filament winding is a process primarily used for hollow, generally circular or oval section components, such as pipes and tanks. Fiber tows are passed through a resin bath before being wound onto a mandrel in a variety of orientations, controlled by the fiber feeding mechanism, and rate of rotation of the mandrel. Chemical storage tanks and pipelines, gas cylinders, etc. are manufactured by filament winding.

Finally, *infiltration techniques* encompass a number of similar processes aimed at manufacturing high quality composite parts which contain a large fiber volume fraction (50-60%) and low porosity levels ($< 2\%$). These techniques use a pressure differential for the infiltration of the resin into a previously compacted dry fabric preform. They are classified depending on the way the pressure differential is applied. *Resin transfer molding* (RTM) uses a closed mold in which the fiber preform is placed and compacted. This is followed by the resin injection using a pressure gradient between the inlet and outlet gates, (P_+ in Figure 1.4), in the range 2-8 bars although high pressure systems of up to 100 bars are now available in the automotive industry.

Usually, the outlet gates are connected to a vacuum pump to assist in the extraction of resin volatiles and to reduce the entrapped voids, leading to the Vacuum-assisted RTM (VaRTM) process, Figure 1.4, in which the pressure gradient is $(P_+ - P_-)$. The use of a closed and matched mold allows an accurate control of the thickness and, as a result, of the fiber volume fraction, but it is restricted to small and medium size parts. Resin is cured in RTM using

cylindrical or flat heat resistances inserted in the mold or by the direct introduction of the mold in an oven.

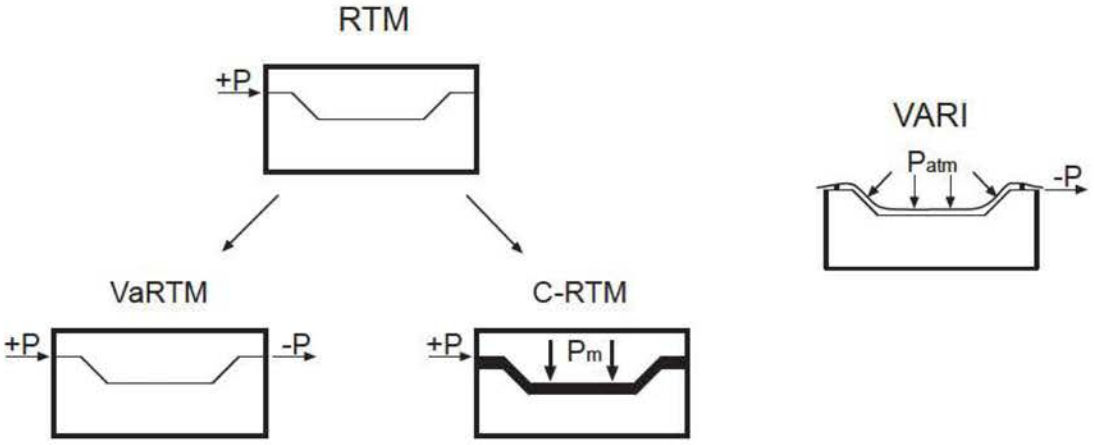

FIGURE 1.4: Infiltration techniques for composite manufacturing. Close (left side) and open mold process (right side).

vacuum infusion is another infiltration technique that uses an open mold. It is also known as Vacuum-Assisted Resin infusion (VARI), Figure 1.4. VARI uses just only rigid part mold. The other mold is replaced by a flexible bag and the resin is infiltrated into the fabric preform under the action of the atmospheric pressure. As a result, accurate thickness and void control are rather difficult to achieve but this technique - as opposed to RTM - can be easily expanded to large composite parts, such as wind turbine blades or yacht hulls.

Other interesting variants of RTM are Compression Resin Transfer Molding (C-RTM), Same-Qualified Resin Transfer Molding (SQ-RTM) or Light Resin Transfer Molding (Light-RTM). Light-RTM is a variant in between RTM and VARI in which the upper side of the mold is replaced by a semi-rigid silicone mold which allows an extra control of the thickness variation together with increased productivity and shorted cure cycles as compared with RTM. C-RTM makes use of an initial over-gap in the mold cavity to allow for an easy fabric impregnation (the permeability of the stress-free fabric is considerably larger than that in standard RTM), Figure 1.4. After full impregnation, the mold cavity is mechanically closed to achieve the

final fiber volume fraction. This process is indicated for high production rates, as in the automotive industry, although the process optimization is quite complex as the fabric move during the impregnation phase. SQ-RTM makes use of standard and previously qualified autoclave prepreg products in a RTM process. In this case, the resin is used to create a very thin resin layer surrounding the composite part to promote a hydrostatic pressure state mimicking the autoclave environment.

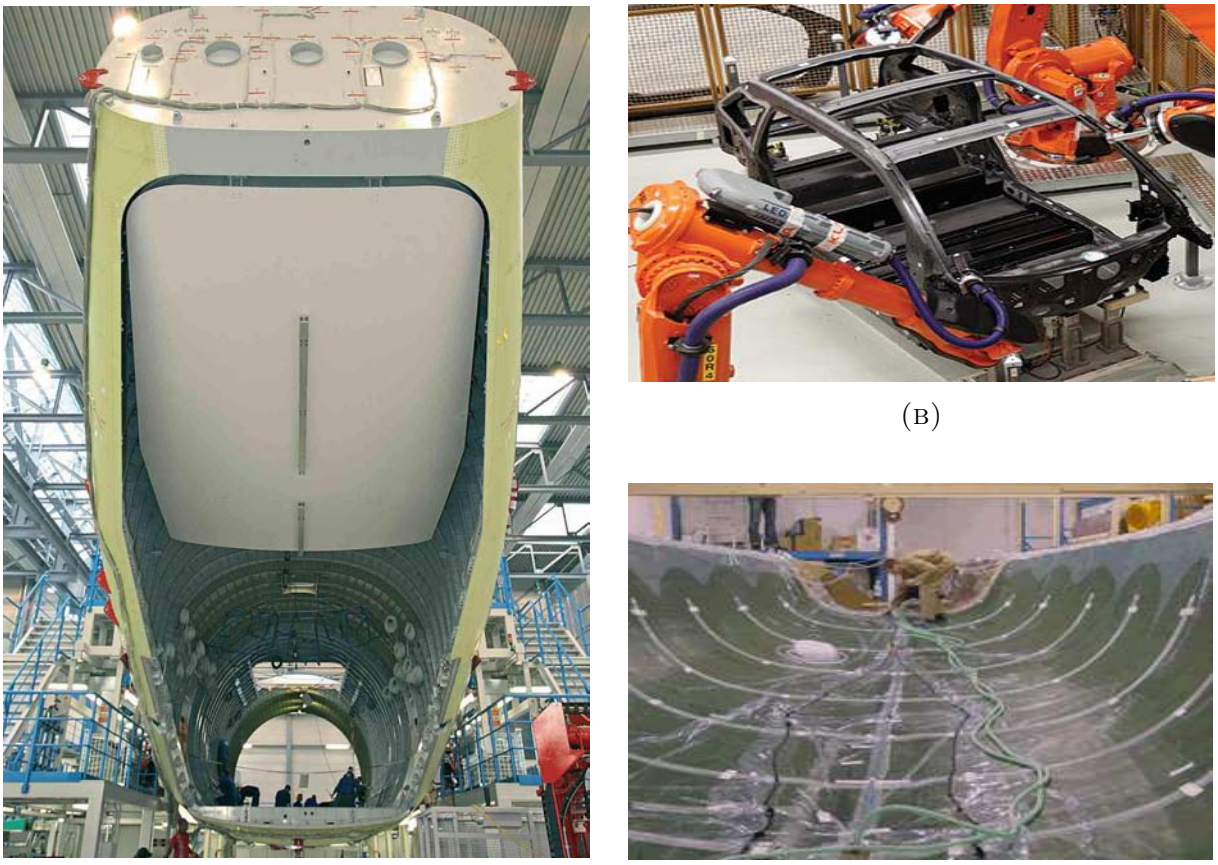

(A) (B) (C)

FIGURE 1.5: Different products made by LCM. A) Cargo door of the A400M military aircraft made by RFI. B) Chassis of the commercial electric car BMW i3 made by RTM. C) Yatch hull structure manufactured using VARI.

While RTM is well suited for manufacturing small components, as in the automotive industry, (Figure 1.5 b), the costs associated with a matched metal tooling makes it less attractive for fabrication of larger components such as wind turbine blades, vessels or fuselage/wing structures. A special attention has been paid in the last years to the VARI process, which

is an open mold process using only vacuum as the driving force to infiltrate resin through a fabric preform, this process reduces considerably the cost associated with tooling because only a single part of the rigid mold is required (Figure 1.5 c). Applications of VARI to manufacture composite parts for the aerospace industry are still limited. An example is the upper cargo door of the A400M military aircraft (Figure 1.5 a) which is, up to date, the largest structural aircraft component produced with this technique. It was manufactured using a variant of VARI known as Resin Film Infusion (RFI) in which the atmospheric gradient is used to infiltrate resin films previously intercalated between adjacent dry fabric layers.

A variant of VARI named Seemann Composites Resin Infusion Molding Process (SCRIMP) uses a cloth called distribution media with a high permeability compared to the infused fiber preform (Figure 1.6. This allows the rapid flow of the resin through the distribution media and is followed by the infiltration in the through-the-thickness direction. This technique is ideally suited for large composite parts as the thickness is much smaller than the planar dimensions allowing the fabrication in a single infusion step.

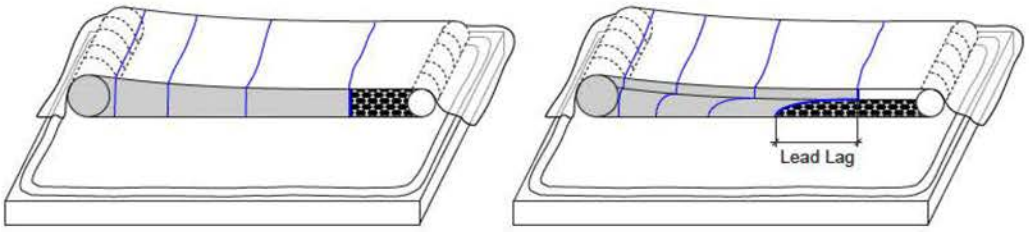

FIGURE 1.6: Schematic representation of the vacuum assisted resin infusion. a) Standard set-up with in-plane flow, b) Combined in-plane and through-the-thickness flow produced with high permeability medium (SCRIMP).

1.3 Fluid flow in liquid molding

The liquid resin is forced to infiltrate the dry preform using a pressure gradient during liquid molding. The main objective is to reach the full impregnation of the fabric by the resin that

propagates between the fiber tows and within the fiber tows reducing as much as possible the volume fraction of voids entrapped during the process. The impregnation driving force results from the pressure difference between the inlet and the outlet gates and the resistance to the fluid flow is characterized by the permeability of the porous fiber network and the rheological properties of the fluid.

According to [7], a porous medium is a material which has an interconnected three dimensional network of capillary channels of nonuniform sizes and shapes commonly referred as pores. This complex structure gives unique properties and distinguishes porous media from other materials, they can be used by their mechanical properties and thermal insulation in the textile industry or in water filtering and fluid transport in hydrology or petroleum and gas extraction.

The fluid flow through a porous media is a complex problem present in many engineering applications, including water flow in granular soils, dam seepage, petroleum extraction and resin impregnation of a textile fabric preform. The first attempt to capture the essentials of fluid flow through a porous media was developed by Henry Darcy [8] in "Les fontaines publiques de la ville de Dijon". Darcy observed that the average fluid velocity through a sand bed porous medium was proportional to the pressure gradient between the inlet and outlet (Figure 1.7).

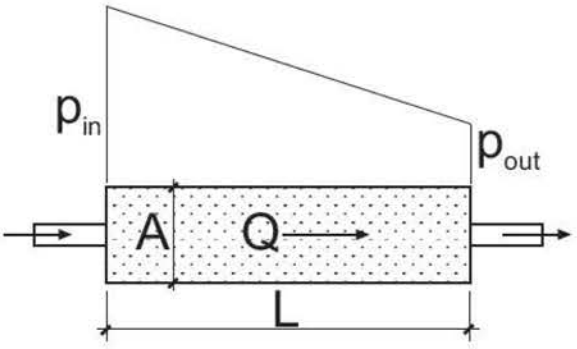

FIGURE 1.7: Uniaxial fluid flow through a porous medium according to Darcy's law.

The phenomenological relation between the volumetric flow rate Q through the porous medium and the pressure gradient $p_{in} - p_{out}$ was expressed as

$$Q = -\frac{KA}{\mu}\frac{p_{in} - p_{out}}{L} \tag{1.1}$$

where A is the cross-section of the porous channel, L the length, μ the fluid viscosity, and K the intrinsic permeability of the porous media. The negative sign in equation (5.1) is required because fluids flow from high to low pressure regions. The phenomenological Darcy's law is the standard constitutive equation used in many models for fluid transport through a porous medium, although it should be mentioned that is only strictly valid for laminar flow regime (low Reynolds number). The differential form of Darcy's equation for three dimensional flow in the absence of gravity forces can be easily generalized and reads as follows

$$\vec{v} = -\frac{\mathbf{K}}{\mu}\vec{\nabla}p. \tag{1.2}$$

This expression relates the average local fluid velocity $\vec{v} = \bar{v}_1\vec{e_1} + \bar{v}_2\vec{e_2} + \bar{v}_3\vec{e_3}$ with the spatial pressure gradient $\vec{\nabla}p$, where $\mathbf{K}$ is the second-order permeability tensor of the porous medium. The permeability tensor can be diagonalized when using principal directions of an orthotropic porous medium as in the case of a fiber preform (e.g. weft and warp directions in woven fabrics). In this case, the average local fluid velocity along the material principal directions (1 and 2 correspond to the in-plane warp and weft directions and 3 to the out-of-plane orientation) is given by

$$\begin{pmatrix} v_1 \\ v_2 \\ v_3 \end{pmatrix} = \begin{pmatrix} K_1 & 0 & 0 \\ 0 & K_2 & 0 \\ 0 & 0 & K_3 \end{pmatrix} \begin{pmatrix} \partial p/\partial x_1 \\ \partial p/\partial x_2 \\ \partial p/\partial x_3 \end{pmatrix} \tag{1.3}$$

where K_1, K_2 and K_3 stand for the in-plane (weft and warp) and out-of-plane permeabilities of the fabric.

The measurement of these permeability factors requires the use of injection gradients (linear or radial) through the fabric that can be either pressure or flow controlled. Fluids as silicone, mineral oils or corn syrup blends are used in these tests because their viscosity at ambient temperature is similar to that standard resins used in liquid molding. The measurement of the out-of-plane permeability factors of the fabric often requires the use of more complex experimental set-ups, as compared with the in-plane tests. The permeability factors depend on the physical characteristics of the fiber and fiber sizing as well as on the preform architecture (unidirectional, woven, random mat, etc.) and on the compaction pressure during the test. The fluid mobility though the fabric decreases when compaction pressure is applied to the fabric because of the constriction of potential fluid channels and plays an important role in composite processing. The higher the fiber volume fraction in the composite, the lower the permeability factor and the easiness to infiltrate the resin into the fabric decreases.

Several theories were developed to describe the pressure dependence, or the fiber volume fraction dependence, of the permeability factors. One of the most popular is the Carman-Kozeny equation [9], which is based in capillary models used in soil mechanics. It reads

$$K = A\frac{(1 - V_f)^3}{V_f^2} \tag{1.4}$$

where V_f is the fiber volume fraction and A a constant which depends on the preform architecture. This model does not account for the differences of the permeability factor in anisotropic media as, for instance, in unidirectional reinforcements. Gebart [10] developed expressions along the fiber direction ($\parallel$) and the direction perpendicular to the fibers ($\perp$) using similar principles,

$$\frac{K_{\parallel}}{D_f^2} = \frac{2}{57}\frac{(1-V_f)^3}{V_f^2} \tag{1.5a}$$

$$\frac{K_{\perp}}{D_f^2} = \frac{4}{9\pi\sqrt{2}}\left(\sqrt{\frac{V_f^{max}}{V_f}} - 1\right)^{2.5} \tag{1.5b}$$

where D_f is the fiber diameter. V_f^{max} represents the maximum fiber volume fraction that can be attained for the unidirectional fiber network and establishes the value at which the transverse channels are totally closed preventing the flow progress.

Fluid flow in most liquid molding applications can be approximated in 2D as the flow along the through-the-thickness direction is negligible when compared with the in-plane flow because the thickness is much smaller than the in-plane dimensions. Obviously, the simulation of infusion/injection problems using a two-dimensional approximation results in computational savings and is the standard approach in mold filling simulations. This simplification cannot be applied when dealing with the SCRIMP process where the flow is a combination of fast in-plane propagation through the distribution media and the subsequent through-the-thickness flow into the fiber preform.

Darcy's law, together with the continuity equation (conservation of mass for incompressible fluids), form the basis for the numerical simulation of the impregnation process. Assuming isothermal fluid flow under incompressible conditions, the governing equation for the pressure field in a fluid saturated domain is given by [11, 12]

$$\nabla(-\frac{\mathbf{K}}{\mu}\nabla p) = 0 \tag{1.6}$$

This second order partial differential equation can be solved under appropriate boundary conditions. The two most common boundary conditions for the fluid ingress into the mold cavity are either the pressure (according to $p_{inlet} = p(t)$) or the flow rate ($q_{inlet} = q(t)$), which is obtained from the pressure derivative at the inlet position. The pressure boundary

condition at the front flow (a moving boundary) is imposed as $p_{front} = 0$ by assuming the simultaneous action of a vacuum pump (Figure 1.8).

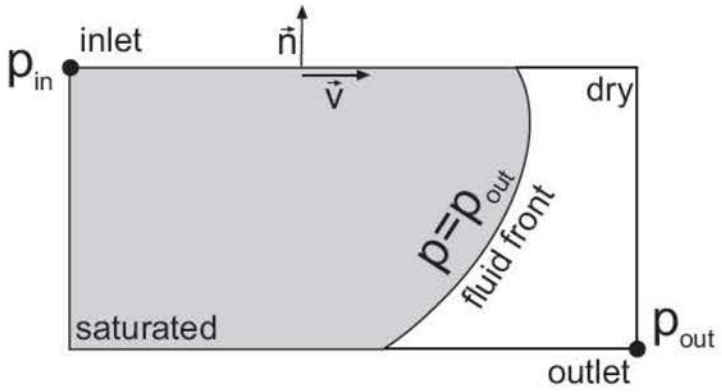

FIGURE 1.8: Boundary conditions in models of fluid flow propagation.

Finally, the fluid velocity normal to the mold wall should be zero and this condition (also known as the standard slip-free boundary condition) is expressed as,

$$\vec{v} \cdot \vec{n} = 0 \tag{1.7}$$

where $\vec{n}$ is the unit vector normal to the mold wall.

The numerical solution of the boundary value problem of equation 1.6 under specific boundary conditions can be carried out using standard numerical procedures, such as finite differences [13], the boundary element method [14] or the finite element method [15, 16]. Among them, the finite element method in combination with the control volume technique (FE/CV) for tracking the fluid flow propagation is the most popular one and is implemented in commercial software packages such as PAM/RTM [17] or LIMS [18]. The success of the FE/CV technique to track the fluid front propagation is based on the use of a fixed discretization without the need of remeshing as opposed to moving-mesh propagation algorithms. The first stage in the FE/CV model is to set-up an appropriate finite element discretization of the whole filling domain. The control volumes are formed using the same finite element mesh and the control volume is associated to each individual node of the mesh (Figure 1.9

a). The flow front propagation is determined from the fluid fluxes, q_{ij}, passing though the boundaries, s_{ij}, between adjacent control volumes $i - j$ according to

$$q_{ij} = -h \int_{s_{ij}} (\frac{\mathbf{K}}{\mu} \nabla p \cdot \vec{n})\, ds \tag{1.8}$$

where $\vec{n}$ is the unit vector normal to the boundary between adjacent nodes s_{ij} and h is the thickness perpendicular to the fabric. Nodal fill factors at time t, ϕ_i, are used to track the fluid flow propagation through the filling domain and are defined as the proportion of the control volume associated with the node i occupied by the fluid. They range from 0 and 1 as the control volume is empty or filled, respectively (Figure 1.9 b). The nodal fill factors ϕ_i are updated using a explicit integration scheme from the flow rates associated to all the nodes connected to node i according to

$$\phi_i^{t+1} = \phi_i^t + \frac{q_i \Delta t}{V_i} \tag{1.9}$$

where Δt is the discretization time, V_i the volume associated to the control volume and q_i the sum of all the flow rates of all the nodes connected to i. It should be mentioned that the FE/CV algorithm guarantees the mass conservation of the problem at any time.

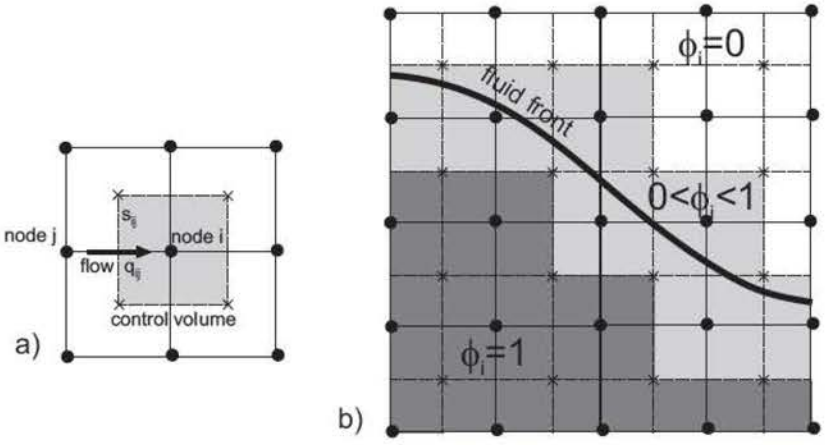

FIGURE 1.9: a) Definition of the control volume in FE/CV simulation schemes, b) Numerical representation of the fluid front using filling factors.

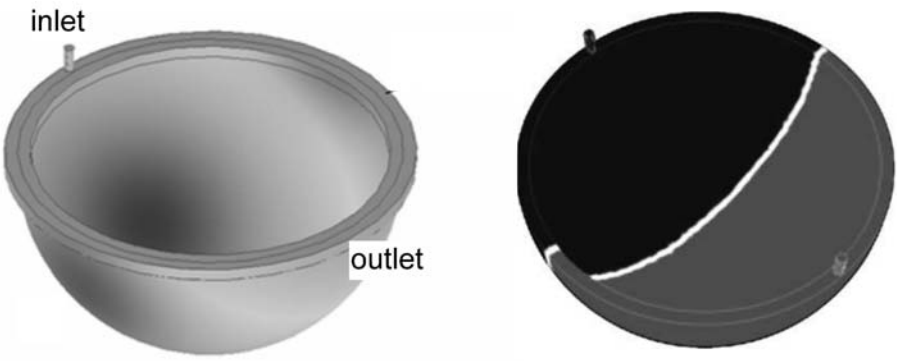

FIGURE 1.10: Filling simulation of a spherical shell using the FE/CV method.

The filling algorithm of FE/CV method used during the infiltration of a complex shape, such as spherical shell, is shown in Figure 1.10.

1.3.1 Influence of fabric deformation

VARI and RTM manufacturing processes use a pressure gradient between the inlet and outlet gates ($\Delta p = p_{in} - p_{out}$) as driving force to fully impregnate the fiber preform. The outlet gate is connected in both cases to a vacuum pump $p_{out} = 0$ while the inlet pressure in RTM is imposed directly by the injection system (e.g. pressure or flow controlled injection) or is equal to the atmospheric pressure (p_{in}=1 atm) in VARI. The pressure field within the fabric preform differs, however, in both cases. The mold gap is constant in RTM (Figure 1.11 a) and, as a result, the volume fraction of fiber reinforcement and the permeability factors remain constant during the injection. However, the thickness varies in position and time in VARI process (Figure 1.11 b). This effect is related with the progressive stress transfer between the fluid and the fiber bed during the infusion process. At the beginning of the infusion, the atmospheric pressure is transferred directly to the fiber bed skeleton through the vacuum bag. However, as soon as the resin progresses, the stress is transferred from the fiber bed to the fluid leading to an spring-back or relaxation of the fiber preform. Thus, the permeability of the fabric changes during infiltration and this phenomenon influences the fluid velocity and the pressure gradients. As a result, the continuity equation (1.6) is no

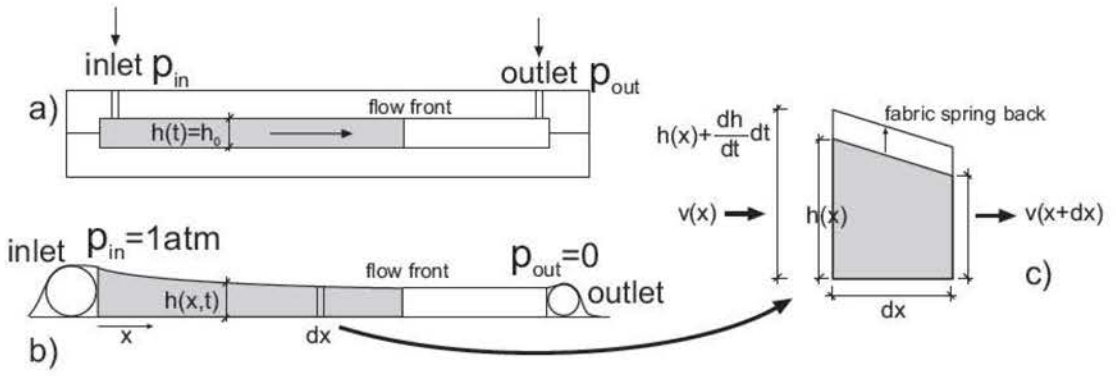

FIGURE 1.11: Scheme for a) Incompressible fabrics with constant thickness h_0, b) Compressible fabrics with the differential mass conservation.

longer valid to simulate resin infusion through fiber preforms and specific modifications in the mass conservation law should be included. Correia [19] reviewed the different approaches [20–24] to quantify the effect of fiber deformability on the pressure profiles for unidirectional resin flow and the strategy is briefly summarized below. A differential control volume for the mass conservation is plotted in Figure 1.11 c). The mass temporal variation within the conservation volume, $\partial M/\partial t$, can be computed as

$$\frac{\partial M}{\partial t} = \frac{\partial}{\partial t}(\rho h(x)dx) = \rho \frac{\partial h(x)}{\partial t}dx \tag{1.10}$$

and should be balanced by the mass passing through the boundaries of the control volume for the same time increment dt (neglecting second order terms) as

$$\rho v(x)h(x) - \rho v(x+dx)h(x+dx) = -\rho \frac{\partial (h(x)v(x))}{\partial x}. \tag{1.11}$$

Then, the mass conservation law for infused preforms under one dimensional flow reads as follows

$$-\frac{\partial h(x)v(x)}{\partial x} = \frac{\partial h}{\partial t}. \tag{1.12}$$

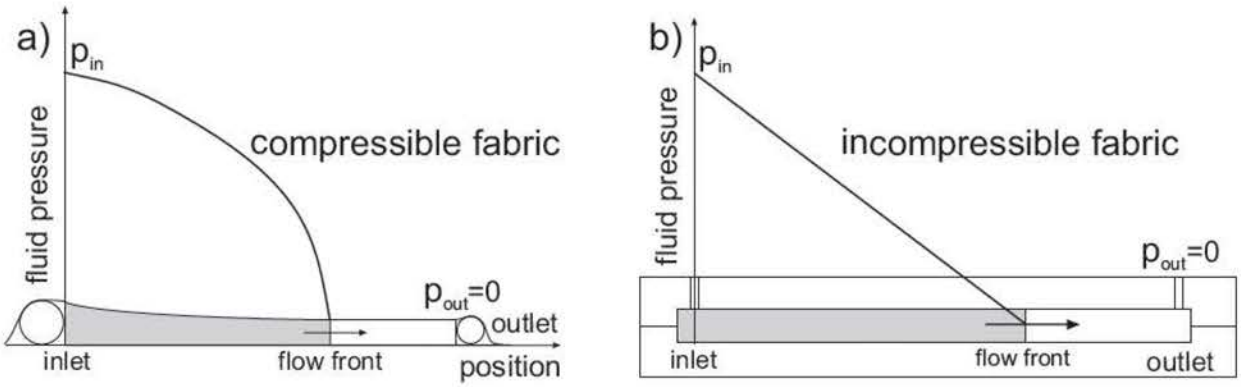

FIGURE 1.12: Fluid pressure fields for a) Compressible fabrics in VARI, b) Incompressible fabrics in RTM.

Using the Darcy's law (equation 1.2) for the average local fluid velocity and rearranging terms, the instantaneous variation of the thickness with time, $\partial h/\partial t$, can be expressed as

$$\frac{\partial h}{\partial t} = \frac{1}{\mu}\left[(K\frac{\partial h}{\partial p} + h\frac{\partial K}{\partial p})(\frac{\partial p}{\partial x})^2 + hK\frac{\partial^2 p}{\partial x^2}\right]. \tag{1.13}$$

The pressure field $p(x,t)$ depends on the permeability variation due to the compaction of the fabric, Figure 1.12 a). It should be noted that if thickness and permeability remain constant (as in the RTM process), the previous differential equation is simplified to $\partial^2 p/\partial x^2 = 0$ which leads to a linear pressure profile between the inlet and outlet gate, Figure 1.12 b).

The unidimensional equation can be easily expanded to bidimensional in-plane flow (see Advani and coworkers [25]) by using the same concept of the control volume. In this case, equation (1.6) is corrected with the compressibility term according to

$$\nabla(-\frac{\mathbf{K}(V_f)}{\mu}\nabla p) = \frac{\dot{V}_f}{V_f} \tag{1.14}$$

In order to solve equations (1.6) and (1.14), it is necessary to know the influence of the fluid pressure on the fiber volume fraction of the fabric. This task can be accomplished using Terzaghi's effective stress concept developed within the framework of soil mechanics

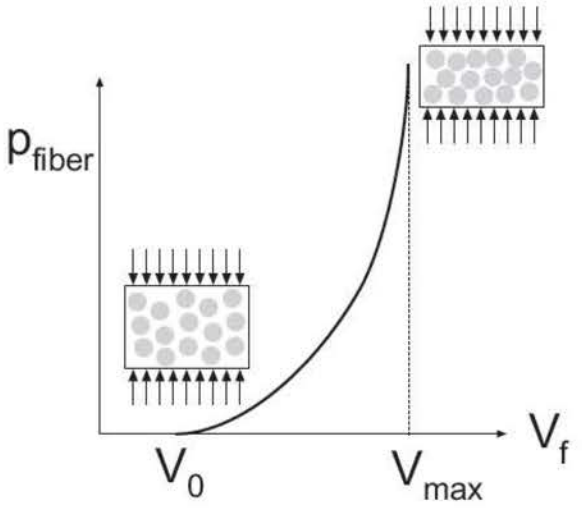

FIGURE 1.13: Fiber bed compaction curve.

and poro-elasticity [26, 27] and applied by Gutowsky [28, 29] and Davé [30] to study the compaction phenomena of fiber beds during composite manufacturing. The atmospheric pressure p_{atm} acting on the bag surface in VARI is transferred to the fiber bed p_{fibre} and the fluid p assuming the equilibrium condition

$$p_{atm} = \sigma_{fibre} + p \tag{1.15}$$

The relationship $\sigma_{fiber} = \sigma_{fiber}(V_f)$ can be measured by the application of a compressive pressure on the fabric and the determination of the corresponding thickness and volume fraction of reinforcement [31] (Figure 1.13). The presence of a fluid during the compaction experiments may alter the response of the fabric producing additional deformation due to the lubrication effects at the fiber and yarns scale. The curves generated during the experiments $\sigma_{fiber}(V_f)$ are typically fitted to power law expressions [19, 25] although more refined micromechanical constitutive models can also be used [28–30]. In these later cases, the stress carried by the fiber bed can be computed as

$$\sigma_{fibre} = \frac{A_0 V_0}{V_f} \frac{1 - \sqrt{\frac{V_f}{V_0}}}{\frac{16\beta^2}{\pi^3 E}\sqrt{\frac{V_{max}}{V_0}}(\sqrt{\frac{V_{max}}{V_f}} - 1)^3} \tag{1.16}$$

where E_f and A_0 stand for the elastic modulus and the cross section of the fiber, β is the average waviness ratio (length of the wavy portion of the fiber with respect to its length), V_0 the initial volume fraction prior to the compaction, V_f the current volume fraction of reinforcement and V_{max} the maximum achievable volume fraction. This expression reflects the stiffening effects of the fiber bed during compressive deformation due to the increasing number of fiber-to-fiber contacts.

1.3.2 Influence of fabric architecture: the dual-scale flow

A major drawback in liquid molding technologies is related with the generation of voids and air entrapments during processing that leads to well-known detrimental effects on their mechanical performance [32, 33]. Macrodefects results from dry or poorly impregnated regions that appear when the resin flow reaches the outlet gate prior to complete the filling stage and are considered the result of an incorrect spatial distribution of the injection/infusion/venting ports [34, 35]. Even if the part has been completely filled with resin, voids can be generated in the material due to the inhomogeneous fluid flow propagation caused by the dual scale of the porosity in the textile preform. Standard reinforcements used in composite manufacturing are produced by weaving tows containing thousands of fibers forming specific fabric architectures (woven, non-crimp, stitched fabrics, etc.), which results in a clear two-scale porosity level. Therefore, the global flow can be divided into meso-flow and micro-flow (Figure 1.14):

- Meso-flow is the fluid flow occurring between adjacent fiber tows which is mainly affected by the external pressure gradients due to the gap between the tows.

- Micro-flow is the flow occurring within fiber tows. In this case, the flow is mainly driven by capillary forces.

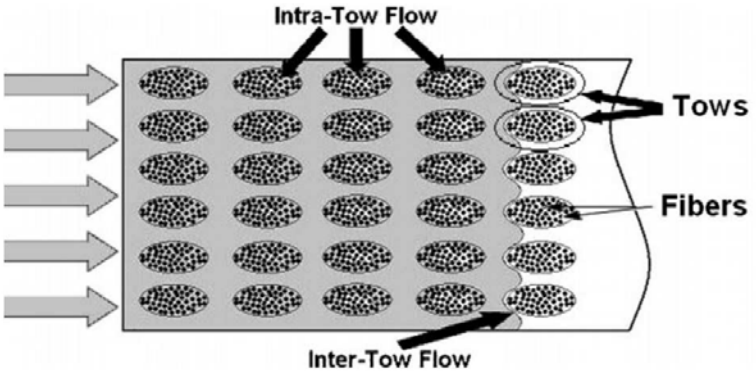

FIGURE 1.14: Sketch of the dual-scale flow during textile impregnation.

The initial free spaces in between individual fibers and between adjacent tows are considered, respectively, micro and mesoscale porosity. Viscous flow dominated by the resin pressure gradient takes place rapidly through the high permeability channels between adjacent fiber tows while tow impregnation perpendicular to the fibers is mainly driven by capillary forces. This dual-scale flow (micro-meso) is responsible of the generation of voids in composite materials by the direct competition between viscous and capillary forces [36–39]. Experimental results demonstrated that void formation in engineering composites depends on the ratio between viscous and capillary forces through the non-dimensional modified capillary number, Ca^*, [40–43]

$$Ca^* = \frac{\mu \bar{v}}{\gamma \cos\theta} \tag{1.17}$$

where μ and $\bar{v}$ stand for the resin viscosity and the average resin velocity, respectively, while γ and θ are the fluid surface tension and the contact angle, respectively. Capillary numbers for an optimum void content in specific material systems have been reported [43]. Viscous forces are predominant over capillary ones for high capillary numbers ($Ca^* > 10^{-2}$), and voids are generated by the rapid flow propagation along the yarn-to-yarn free gaps while void

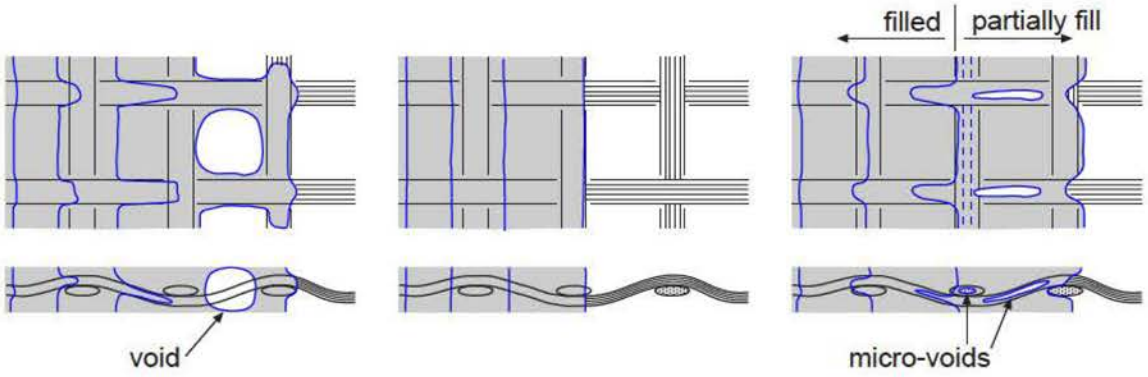

FIGURE 1.15: Different infiltration scenarios depending on the capillary number (Ca^*). a) $Ca^* < 10^{-3}$, b) $10^{-2} < Ca^* < 10^{-3}$, c) $Ca^* > 10^{-2}$.

entrapments are generated at the intra-tow level (Figure 1.15). On the contrary, the fluid velocity is small for low capillary numbers ($Ca^* < 10^{-3}$) and the wicking effects caused by the intratow capillary forces become predominant. In this later case, entrapments are generated at the tow interfaces rather than at the intratow spaces. Finally, the intermediate regime is characterized by the coexistence of intra-tow and inter-tow voids. The appropriate range of filling rate (given by the capillary number) with uniform progress of both flows would lead to a minimization of the void formation in the material. Macro-voids can be easily reduced by selecting the appropriate venting strategy controlling the pressure gradients within the fabric preform. However, microvoids are more difficult to evacuate due to the surface tension forces acting at the fiber bundle scale. As a result, microvoids will tend to be confined in areas with low pressure gradients. Understanding these mechanisms of resin flow during liquid molding is crucial to manufacture high quality composite parts with low fraction of voids and defects. Moreover, the selection of the appropriate experimental technique to address void generation and transport becomes crucial.

1.4 Objectives of the thesis

Autoclave consolidation of prepregs is a well-established processing technique to manufacture composite materials with high fiber volume fraction and low porosity and, thus, excellent

mechanical properties. Nevertheless, the costs associated with this technique hinder their application in other industrial sectors besides aerospace and sport goods and their is a strong interest to optimize composite processing by liquid molding. Most of the attention in this area has been focused in RTM because VARI -although it has larger potential for cost savings- is rather difficult to control. Atmospheric pressure gradients depends on the geographical location of the factory resulting in a variable driving force. Thickness accuracy is rather difficult to achieve, specially during impregnation of large components where the load transfer between fibers and resin plays a critical role. Voids are generated from the different resin velocities due to the dual meso-structure of the fabric depending on the rheological properties of the resin, viscosity, contact angle, surface tension. Finally, the definition of the infusion strategy, including the location of infusion and venting ports, is of key importance to avoid the apparition of dry or poorly impregnated regions, and to reduce the filling times. This thesis has been aimed at improving our understanding of the mechanisms of resin infiltration during VARI so these objectives can be achieved.

Within this framework, the objectives of this thesis are the following:

- Understand the physical mechanisms of resin infusion at the mesoscopic level. To this end, detailed infusion experiments were carried out and all the experimental variables involved in the process (permeability, compaction, stress transfer between the fiber preform and and the infused fluid) were measured independently.

- Analyze the nature of the dual-scale flow during vacuum infusion. While mesosocopic flow between tows and the development of macroscopic porosity can be easily tracked by visual inspection, there is no experimental evidence of the process of void generation and migration at the microscopic scale (intratow voids). *In situ* infusion experiments in a synchrotron were carried out for the first time to determine intratow flow and void transport by means of X-ray computed microtomography.

- Develop a numerical model to predict the thickness variation and fluid pressure evolution during vacuum infusion. The model included the effect of the progressive stress

transfer from the fiber bed to the resin and was validated against the infiltration experiments.

1.5 Organization of the thesis

After the introduction, the thesis is organized in five chapters. The description of all the experimental techniques (vacuum infusion experiments, digital image correlation, X-ray computed tomography, etc.) is presented in Chapter 2. Chapter 3 includes all the experimental results corresponding to the infusion experiments and to the measurement of the parameters required for the modelization. Tow infusion experiments carried out under X-ray synchrotron radiation to evaluate the evolution of the flow front at the microlevel as well as the corresponding void transport mechanisms are presented in Chapter 4. A new model for vacuum infusion based on the level set method is presented in Chapter 5. The model is able to track the flow front evolution as well as the pressure field and compaction phenomena during infusion and it is validated against the experimental results in Chapter 3. Finally, Chapter 6 summarizes the main conclusions and the original contributions of the thesis and presents several topics for further investigation.

Chapter 2

Experimental techniques

This chapter is devoted to present all the experimental techniques used in the infusion experiments carried out in this thesis. The information in this chapter contains key original contributions of this thesis that were developed to achieve one the goals of the investigation: obtain new insights of the underlying physical mechanisms that control the infusion of a textile preform at the mesoscale and microscale. VARI uses the vacuum pressure as the driving force to infiltrate a fluid into the fabric preform and the stress transfer between the textile fabric and the fluid leads to a continuous change in the thickness during infusion. A new experimental set-up based on digital image correlation was developed to monitor the thickness evolution. This information, in combination with the pressure evolution, was necessary to characterize the infusion at the mesoscopic level and and provided the quantitative information for model validation. In addition, another novel strategy based on X-ray computed microtomography was developed to monitor the microscopic flow and determine the physical mechanisms responsible for void transport within the fiber tows.

2.1 Experimental set-up for vacuum assisted resin infusion

Vacuum infusion tests were performed following a standard experimental set-up. In addition, the fluid pressure was monitored with pressure sensors and the thickness variation by means of Digital Image Correlation (DIC) (Figure 2.1).

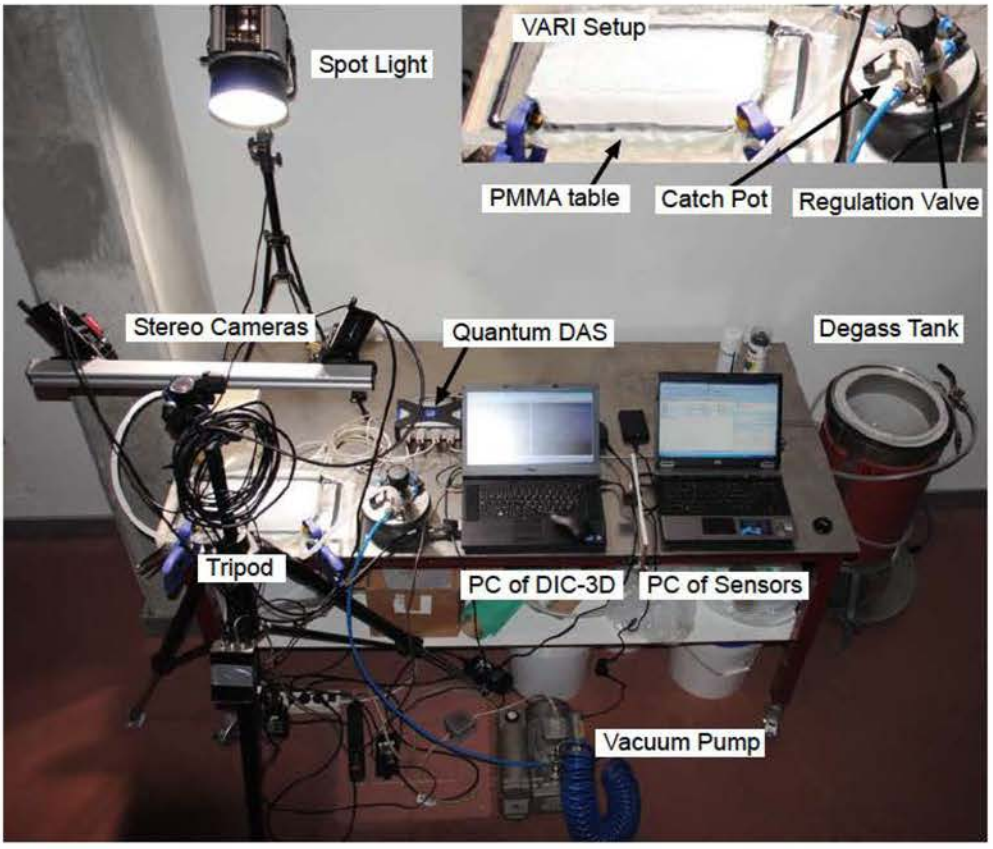

FIGURE 2.1: Experimental set-up for the vacuum infusion tests.

The standard VARI process is very simple although it requires hand lay-up, and several steps are subtle and very time consuming. They are summarized in Figure 2.2. Firstly, the infusion area is delimited with a sealing tape (LTT-90B) on a rigid mold surface of PMMA. A release agent, such as Frekote, is applied on the mold area to avoid resin sticking. Fabric layers are cut to the dimensions of the infused panel and weighted to determine the exact resin volume

for the infusion. When the release agent is dry, the fabrics are laid up (Figure 2.2a), followed by a peel ply fabric and, if necessary, the distribution medium. The peel ply is a textile fabric to separate easily the infused panel from the others layers after curing and create a rough surface ready for adhesive bonding. The distribution medium is a highly porous material which allows to carry out the infiltration of the fabric in the through-the-thickness direction rather than by fluid infiltration along the fabric plane. Thus, through-the-thickness or in-plane flow will be achieved depending on whether or not the distribution medium is included.

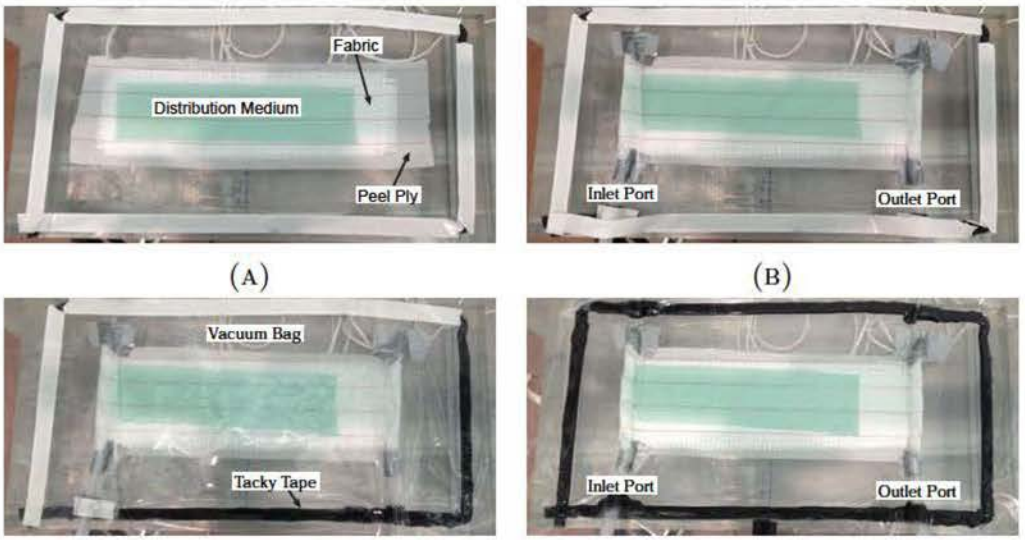

FIGURE 2.2: Vacuum infusion steps. (A) Fabrics are laid up. (B) Inlet (left side) and outlet (right side) gates are set and connected. (C) All the edges of the bag are sealed with sealing tape.(D) Close the inlet and apply vacuum through the outlet.

The next step is to place the inlet and outlet gates (Figure 2.2b) formed by open spiral tubes connected to another rigid tube by sticky tape. The inlet is connected directly to the resin pot while the outlet is connected to the catch pot to avoid resin flow into the vacuum pump. An important detail of VARI process is to place the resin pot at a lower level than the infused fabric. Otherwise, the resin pressure is no longer the vacuum and it will inflate the cavity. Sealing the cavity is a difficult task which requires several trial an error operations until the panel has a perfect seal, and the vacuum pressure is maintained (leaks below 0.01 mbar/min). The plastic cover of the sealing tape is gently removed when installing the

vacuum bag (NBF-540-LFT) (Figure 2.2c) and the tubes are additionally sealed with a ring of sealing tape. The tape on the aligned zones on the opposite side of inlet and outlet is arranged in a loop to avoid the development of stresses in the bagging film when vacuum is applied. Finally, the inlet port is closed with the help of a clamp when the vacuum bag is ready and the vacuum pump switched on (Figure 2.2d). By using a regulation valve, the vacuum is increased progressively until the vacuum bag adapts without any creases over the panel surface. After checking that the cavity has no vacuum leaks, the panel is infused by simply opening the clamp at the inlet port.

Before each test, it is necessary to degas the infusion fluid and this is a critical step in the VARI process because the fluid contains some dissolved air (e.g. resulting from mixing of different resin components). The fluid is first degassed in an independent container (left side of Figure 2.1) by applying vacuum for approximately 20 minutes until the resin stops boiling and bubbles are no longer created.

The whole experimental set-up is mounted in a PMMA table of 500 mm in length and 250 mm in width, where all the fabrics are lay down symmetrically in an area of 250 x 100 mm^2 (Figure 2.3). The position of the pressure transducers is also shown in this figure.

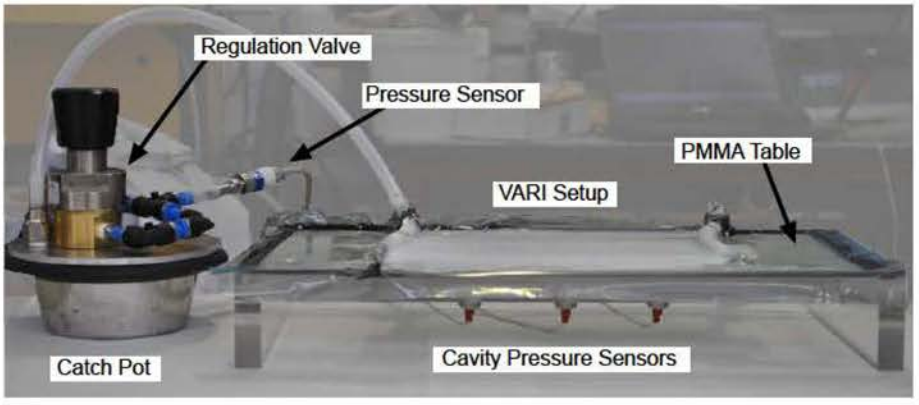

FIGURE 2.3: Instrumented PMMA table with the monitoring pressure system.

Three pressure sensors (Omega® PX61V0-100AV) were used to measure the fluid pressure inside the vacuum bag. They were equally spaced along the panel length and were inserted using threaded holes machined on the PMMA table. The vacuum pressure of the outlet

was controlled by a screw-driven valve regulator (Tescom® DV) and a pressure transducer (HBM® P8AP). They were connected between the catch pot and the vacuum pump. All the sensors were connected to a computer-controlled universal data acquisition system (QuantumX MX840A) after signal amplification and conditioning. The acquisition was carried in real time at 1 Hz of sampling frequency. Each transducer had an independent set of calibration parameters which are used by the acquisition software. Before the test, all the sensors were connected at the maximum vacuum pressure of the pump using a manifold. This common pressure was used as the reference.

2.2 Digital image correlation

Digital Image Correlation (DIC) is an optical, non-contacting measurement technique to measure the full-field in-plane or out-of-plane displacements of the vacuum bag. DIC is a mature tool commonly used for the measurement of the displacement fields during mechanical testing, but there are only a few applications to infusion processing [44]. The main advantages with respect to traditional sensors -as a Linear Variable Displacement Transducers (LVDT)- are the higher spatial resolution and the capture of the displacement field in the whole surface. Moreover, any interference between the sensor and the surface of the specimen is avoided. Thus, DIC is particularly suitable for the *in situ* measurement of the vacuum bag displacement during vacuum infusion.

DIC is based in the spatial correlation of the deformation of a speckle pattern sprayed deposited on the surface of the vacuum bag by tracking the distribution of the gray intensities in images of such pattern obtained during the test. The correlation algorithm begins with the definition of a square area of $n \times n$ pixels called subset (Figure 2.4), where the deformation is assumed to be constant. Inside of the subset, the coordinates of the center point $\mathbf{P}$ and of an arbitrary pixel $\mathbf{Q}$ are defined with respect to the reference configuration. These pixels will be displaced to new positions within of the deformed subset, given by the coordinates

$\mathbf{P}'$, $\mathbf{Q}'$ in the deformed configuration. $\mathbf{P}'$ and $\mathbf{Q}'$ are related to $\mathbf{P}$ and $\mathbf{Q}$ through the vectors $\mathbf{u}$ and $\mathbf{v}$, respectively.

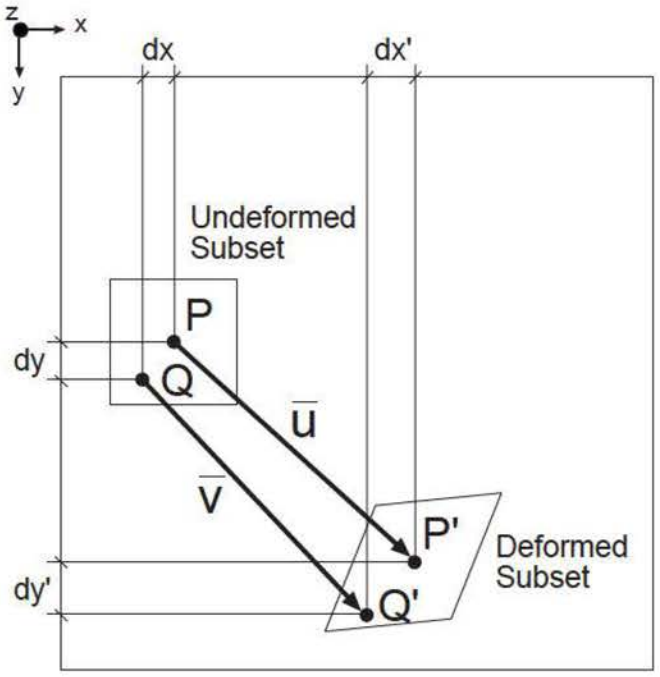

FIGURE 2.4: Deformation of a subset in two dimensions.

The intensity function I gives the gray intensity in any point of the subset $I(\mathbf{Q})$ and $I(\mathbf{Q}')$ in the undeformed and deformed configurations, respectively. It is assumed that the intensity of corresponding points $\mathbf{Q}$ and $\mathbf{Q}'$ in the speckle pattern does not change during deformation, and hence

$$I(\mathbf{Q}') = I(\mathbf{Q} + \mathbf{v}) \tag{2.1}$$

The coordinates of any point $\mathbf{Q}'$ of the subset in the deformed configuration can be related to the central point of the subset $\mathbf{P}$ in the undeformed configuration by

$$\mathbf{Q} = \mathbf{P} + \mathbf{v} + \nabla(\mathbf{v})(\mathbf{Q} - \mathbf{P}) \tag{2.2}$$

where $\mathbf{v}$ is the displacement of point $\mathbf{P}$ and $\nabla(\mathbf{v})$ the displacement gradient. According to this equation, the deformation of the speckle pattern in the subset can be obtained by finding the optimum value of $\mathbf{v}$ that minimizes the gray differences within the subset in the undeformed and deformed configuration. To this end, a correlation function of the gray level is defined as [45],

$$C(\mathbf{Q}, \mathbf{v}) = \sum_{i,j=-n/2}^{n/2} \left[I(\mathbf{Q}) - I(\mathbf{Q}' + \mathbf{v}) \right]^2 \tag{2.3}$$

and various algorithms are available in the literature to find the optimum $\mathbf{v}$ and $\nabla(\mathbf{v})$ that minimize C within the subset [46, 47]. Once the displacement of the central point $\mathbf{P}$ is obtained, the subset is shifted along the x and y directions (step parameter) to calculate the deformation of the next point. Once the displacement field is obtained in the whole surface, strains are computed from the displacement gradient following the continuum mechanics definitions.

The out-of-plane displacement can also be obtained by stereographic DIC. Two cameras are needed in this case and a previous calibration of the cameras is required. The calibration algorithm is based on the stereo-photogrammetry principles [48] of triangulation to obtain the 3D spatial position of the two cameras by taking pictures of a calibration target (Figure 2.6). The calibration target is a pattern of 12 $\times$ 9 points equally spaced 9 mm. After the software has the correct spatial position of the cameras, two more steps are necessary, called the stereo correlation and triangulation. The stereo correlation uses the procedure detailed above for 2D but for a pair of images within the area of interest. Firstly, the pair of images are correlated to each other and then to the original reference image. Afterwards, the coordinates of the correlated points with respect to the reference frame are obtained by triangulation.

The VARI experiments in this thesis were carried out using the DIC-3D system from Correlate Solutions®[49]. The experimental set-up is shown in Figure 2.5 and includes one tripod which regulates the spatial position of the two high resolution cameras (29 Mpixels) for the stereographic vision. A spot light source in the middle maintains an homogeneous brightness in the region of interest for DIC.

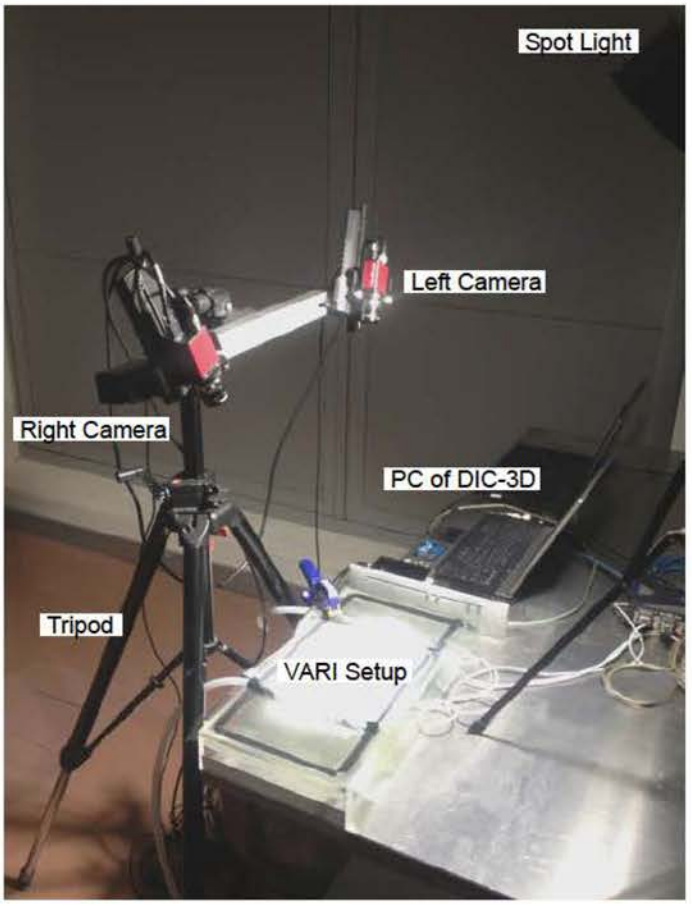

FIGURE 2.5: Digital image correlation set-up.

The preparation of the infusion test surfaces for the DIC system requires different steps to obtain a correct and uniform random speckle pattern. Firstly, the specimen is painted with white mate color to avoid light reflections during the acquisition of the images. Afterwards, a random speckle pattern is applied by spraying black spots on the white surface. The acquisition rate was selected depending on the process duration and it was set to 10 or 60 images per minute for in-plane or out-of-plane infiltration, respectively.

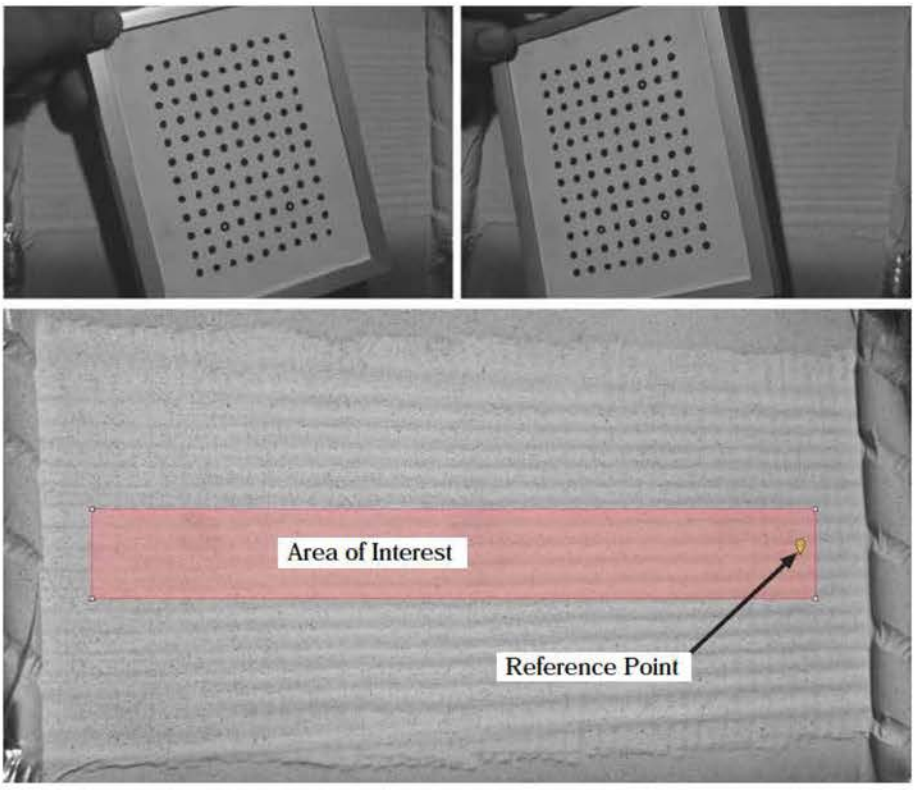

FIGURE 2.6: Stereo images with the calibration target of 12 × 9 points. (a) left image. (b) Right image. (c) The AOI is delimited symmetrically on the reference image and it is set the reference point.

By using the post-processing software of the system, an Area Of Interest (AOI) is delimited within a rectangle of 210 × 10 mm^2 in the initial image (Figure 2.6), and the DIC algorithm calculates the displacement fields with respect to this reference image. The subset and step size were 29 and 7 pixels, respectively.

2.3 X-ray computed microtomography

X-ray computed microtomography (XCT) [50, 51] is a non-destructive imaging technique that provides information on the three-dimensional (3D) structure of a material. The sample is positioned in between a X-ray source and a detector. The X rays traveling through the sample are attenuated depending on the absorption coefficient of the material and the energy

of the incident X-ray beam reaching the detector which records a radiography. During a tomographic scan a set of radiographies is recorded at different angle positions and the full 3D object is reconstructed from the images at different angles.

The microstructural features that induce a modification of the attenuation or of the optical phase along the path of the X-ray beam, depending on the tomographic set up, can be detected with this technique. They include different chemical elements or phases, inclusions, cracks, pores, etc. XCT has been traditionally used in medicine, but it has become a standard tool for Material Science characterization with the development of the third generation synchrotron sources which provide beams of high energy and high brilliance, and with the improvement of the spatial and temporal resolution even in laboratory devices.

X-ray radiography physics[52] is based on the Beer-Lambert law (Equation. 2.4), which relates the intensity of the incident and transmitted X-ray beam of a certain energy with the corresponding attenuation coefficient μ along the beam path according to

$$\frac{N_1}{N_0} = \exp\left[-\int_{S\in ray} \mu(s)ds\right] \tag{2.4}$$

where the N_1 and N_0 are the number of transmitted and incident photons, respectively. The attenuation coefficient μ might vary along the beam path due to the changes in the local composition of the sample, such as density and atomic number, as well as to the photon energy. The total attenuation of the beam will depend on the path in heterogeneous materials, thus providing the contrast observed in the radiography.

Besides attenuation, X-rays might experience a phase shift during propagation through the material when two parallel rays pass on each side of an interface of two different constituents. This phase contrast is due to interference between parts of the wavefront that have suffered slightly different angular deviations. A condition to observe contrast due to a phase shift is that the X-ray beam is monochromatic and partially coherent. The overlap between parts

of the wavefront is only possible after propagation over a certain distance. In general, phase contrast imaging is much more sensitive than absorption imaging.

The X-ray radiation used for tomography experiments is normally produced by standard X-ray tubes or by a synchrotron sources. In an X-ray tube, X-rays are generated by the acceleration of electrons from a filament towards a target material, normally made of a heavy element, such as tungsten or molybdenum. Synchrotron radiation is generated when relativistic electrons moving in the so called storage ring are accelerated by a magnetic field which modifies their trajectory. The magnetic field can be applied by diverse devices, e.g. bending magnets, wigglers, undulators, etc. The X-ray beam produced is tangent to the curved trajectory of the electrons, hence the beam lines are also tangent and located all around the storage ring.

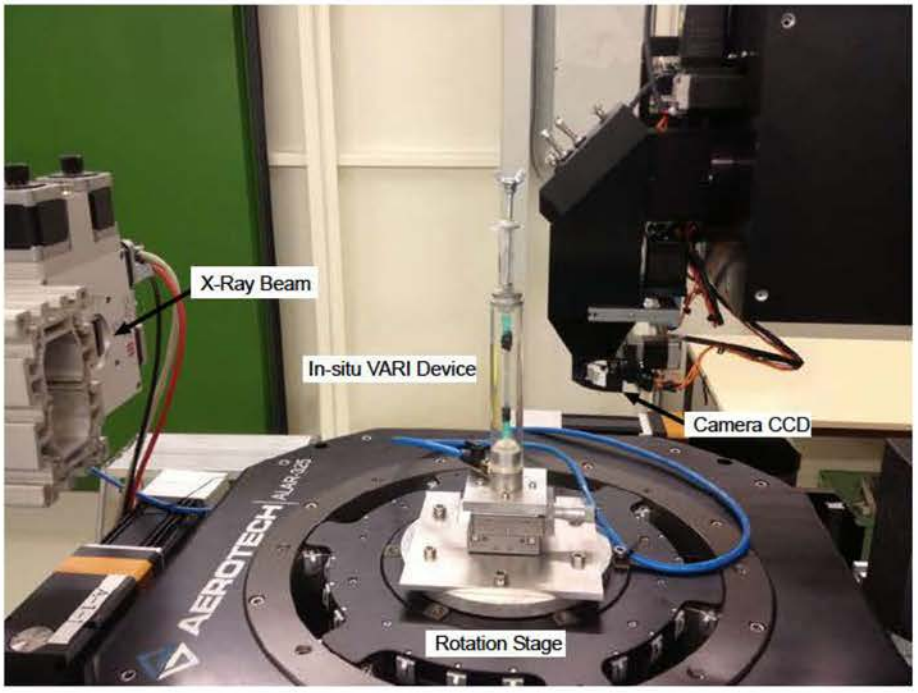

FIGURE 2.7: Hutch of the beamline P05 in Petra III.

The beamline is where the experiment using the X-ray beam emerging from synchrotron is performed. A tomographic measurement can be carried out with white beam, pink beam or monochromatic beam. The tomographic beamline where the experiments were carried

out (P05 at Petra III) receives the beam from an undulator, from which the proper energy is selected by a monochromator. Placing the device on the rotation stage (Figure 2.7) the X-ray beam penetrates through the sample and the attenuated beam is recorded at different angular positions over 180°, which is sufficient for the parallel beam configuration due to the symmetry. Normally, a number of projections in a range $(\pi/4; \pi/2)$ are taken for 360° (one half of that for 180°) in order to obtain a good quality reconstruction. The detection system converts X-ray into visible light thanks to a scintillator. The resulting visible image is then magnified by light optics and projected onto a CCD chip from which a digital image is read out into a computer. The results are post-processed in a set of projections that are used for reconstructing a complete 3D image representing the local X-ray absorption coefficient distribution in the sample. Finally the volume is segmented into different regions by the gray scale of pixels (Chapter 4).

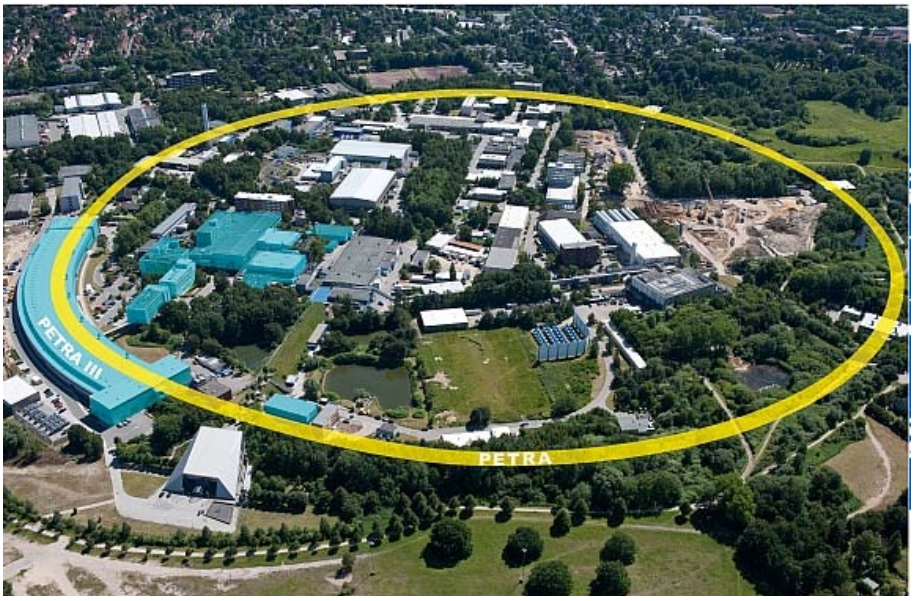

FIGURE 2.8: Bird's eye view of Desy installations in Hamburg. Petra has a circumference of 2.3 km and it is the most brilliant light source in the world. The lower left building is the PETRA III experimental hall with 14 beamlines.

Synchrotron installations have experienced a tremendous improvement over the last decades which has lead to the construction of third generation synchotrons, such as Petra III at DESY (Deutsches Elektronnen-Synchrotron), one of the world's leading accelerator center, in

Hamburg (Figure 2.8). A particular characteristic of third generation synchrotron radiation is that produces X-rays with high brilliance (even if it is monochromatized), practically parallel and partially coherent, while an X-ray tube produces a fan, polychromatic and non-coherent beam with a brilliance orders of magnitude lower than those of synchrotrons. One of the techniques available at some synchrotron is X-ray microtomography, which achieve submicrometric resolution without X-rays optics and normally allows to obtain absorption and phase contrast tomography, or to get some amount of phase and absorption contrast.

2.4 In-situ infiltration set-up

A miniaturized device for vacuum infusion was designed and built to study the infiltration mechanisms operating at the micro-scale by means of XCT. In particular, the object was to monitor the flow through a single yarn of fibers at the micro-scale to assess the effect of viscous and capillary forces on the fluid propagation.

The apparatus was designed in such a way that the fluid is infiltrated from the top of a vertical single fiber yarn while the outlet is placed at the bottom (Figure 2.9). Thus, the device can be installed on the rotation stage of a XCT system. The miniaturized device allows to study small specimens consisting of one to three fiber tows within the detector field of view (FOV) of the X-ray system. An important feature of the device is the miniaturization of all the parts of the infusion process, including the inlet and outlet ports. The inlet was manufactured using a syringe needle which provides a reservoir of 20 ml and a piston system that allows to accurately control the infused fluid. The outlet was made using an open syringe previously cut and adjusted to the support, which is connected to the vacuum system. The sample is a single yarn, placed between the inlet and the outlet, connecting the two ends with the respective syringe needles, and sealed with standard tacky tape (LTT-90B). The whole system was mounted on an aluminum support providing the connection to the vacuum system. The yarn is placed into a PMMA tube with low X-ray absorption to provide the necessary stiffness to the device, and avoiding dangerous leaks during the acquisition time.

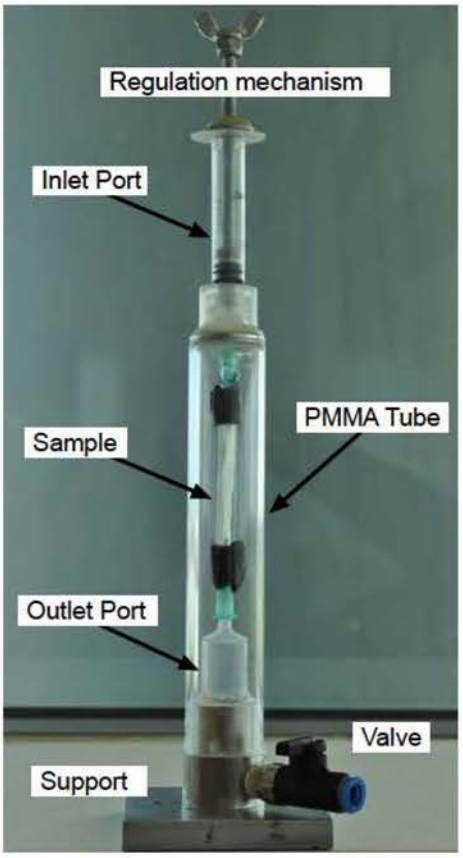

FIGURE 2.9: Experimental device for in-situ infiltration.

The procedure to prepare and mount a sample of, for instance, a single tow is the following. Firstly, the fiber tow is covered with a vacuum bag (NBF-540-LFT) and the edges are thermally sealed along the sample length. The specimen is then cut to the correct dimensions in order to fit in the FOV of the detector (around 40 mm in length by 3.8 mm wide) inserting the needles at both ends and sealing them with standard tape. Finally, the sample is placed between the syringes by connecting to the needles and to the PMMA tube, that holds the whole system (Figure 2.10).

The fluid infusion is controlled by a simple regulation system made up of a screw and a nut with a washer. Initially, the nut and the washer block the syringe piston preventing fluid propagation driven by the vacuum. The infusion can progress by rotating the nut of the screw while the vacuum acts in the yarn. This procedure allows to accurately control

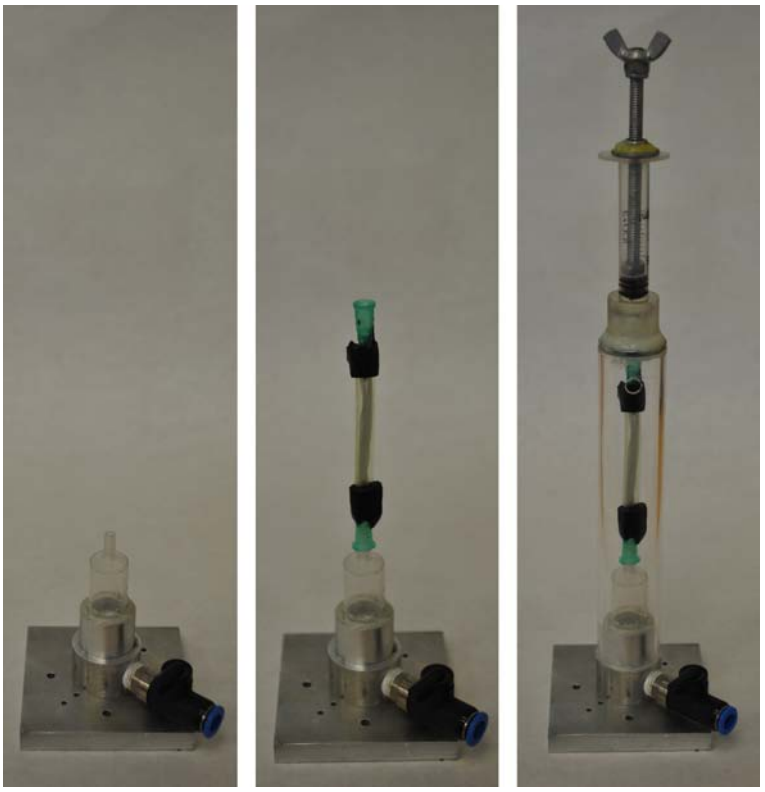

FIGURE 2.10: Preparation steps of the insitu infiltration tests. (a) The syringe is sealed with the base plate. (b) The sample is connected to the bottom syringe. (c) The PMMA tube with the reservoir is connected to the sample.

the flow front by adjusting the nut rotations. This is critical because any parasitic fluid propagation through the sample during the acquisition time of the tomograms will produce image artifacts and blurring in the reconstructed volumes making impossible to create a detailed reconstruction of the flow front. The acquisition time for each tomogram was about 2 hours (see Section 4.2)

Chapter 3

Experimental analysis of resin infusion at the mesoscale

This chapter is devoted to the experimental characterization of the flow mechanisms at the mesoscale during the impregnation of a fiber preform by vacuum infusion (VARI). Three laminates ($[0°]_2$, $[0°]_4$, $[0°]_8$) were infiltrated in order to ascertain the effect of thickness on the macroscopic flow. In-plane (standard VARI) and out-of-plane (SCRIMP vacuum infusion) flow were studied, the latter by placing a distribution medium film on top of the laminate. The laminate thickness variations during the infusion process were measured by means of digital image correlation while the effect of fiber compaction on the pressure distribution was captured by means of pressure sensors distributed along the infusion length. In addition, the fluid rheology (viscosity and contact angle), the in-plane fabric permeability and the compactability were determined by means of independent tests.

As mentioned in Chapter 1, fluid flow during vacuum infusion is mainly controlled by the competition between fabric compaction and fluid permeability. Before impregnation, the atmospheric pressure over the vacuum bag is directly transferred to the dry fiber network leading to compaction of the laminate. As the fluid infiltrates the fiber preform, the atmospheric pressure is shared between the fiber network and the fluid resulting in the well-known

elastic spring back effect. The stress transfer mechanisms between the fluid and the fiber network strongly influence the mesoscopic flow because the preform compaction and the permeability are no longer homogeneous in the infused part, leading to important changes in the pressure distribution, fluid velocity and filling times. This behavior is significantly different from that found during resin transfer molding (RTM) in which the thickness of the cavity is constant during infiltration.

The mechanisms of fiber compaction during the infiltration of the porous preform can be explained by using a simple model derived from the soil consolidation theory developed by Terzaghi, Figure 3.1. Initially, the atmospheric pressure is transmitted directly to fiber bed skeleton $\sigma_{fiber} = p_{atm}$ which acts as an elastic spring, Figure 3.1 b). As soon as the fluid progress throughout the preform driven by vacuum, the pressure is not longer held by the fabric but shared with the infused fluid according to $\sigma_{fiber} + p_{fluid} = p_{atm}$. This stress transfer mechanism results in a elastic recovery called as "spring back" effect, Figure 3.1 c).

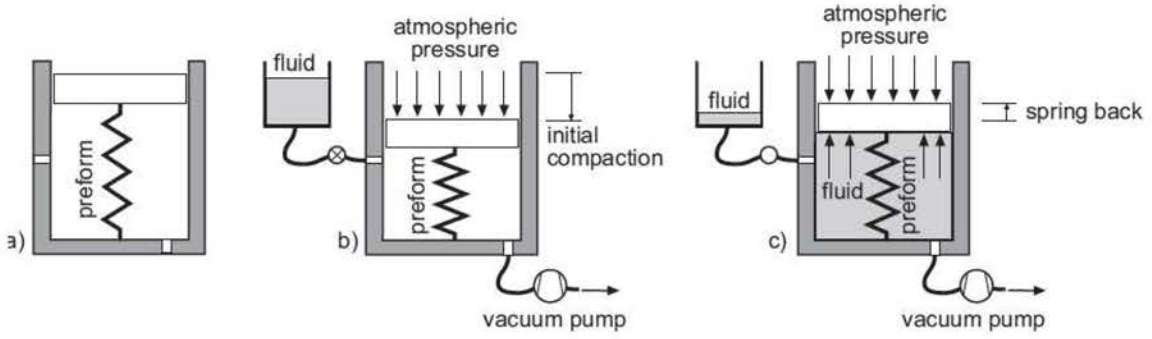

FIGURE 3.1: Sketch of the stress transfer mechanisms between the fabric preform and the infusion fluid. a) Initial stress-free state. b) Dry fabric preform compaction during vacuum bagging. c) Stress transfer between the infused fluid and the fabric preform leading to the spring-back effect

3.1 Vacuum infusion experiments

Vacuum-assisted resin infusion (VARI) experiments were carried out in an standard E-glass plain woven fabric infused with a blend of corn syrup (70%) and water (30%) The experimental set-up for the infusion tests was presented in Figure 3.2, leading to an approximate unidimensional flow between the inlet and outlet gates, as shown in Section 2.1. Rectangular strips of 250 x 80 mm^2 of the fabric were cut and carefully laid on the top of a PMMA flat mold tool. A set of three pressure transducers (P1, P2 and P3 in Figure 3.2) were uniformly distributed over the infusion length. The inlet gate was connected to the corn syrup blend pot while the outlet gate was connected to the resin trap and the vacuum pump. A mechanical valve was used to precisely control the applied vacuum pressure during the test which was measured by an additional pressure transducer (P4 in Figure 3.2).

Laminates with three different thicknesses ($[0°]_2$, $[0°]_4$, $[0°]_8$ stacking sequences) were infiltrated. In-plane and out-of-plane flow were studied, the latter by placing a distribution medium film on top of the laminate. The fluid flows rapidly through the distribution medium because of its high permeability and infiltration of the fiber preform is carried out simultaneously from the side and from top, leading to a combination of in-plane and out-of-plane flow which reduces significantly the total filling time. The displacement field (or the variation of the fabric thickness $\Delta h(x,t)$ during the infusion experiments) was measured by means of digital image correlation. To this end, a speckle pattern was painted on the vacuum bag surface using a white painting with a fine dispersion of black dots. The speckle pattern was deposited after several vacuum/release cycles in order to mitigate as much as possible nesting effects between fabric layers during the infusion experiments.

The area of interest, AOI, (region were digital image correlation is performed) was restricted to a central strip of 210 x 10 mm^2 aligned with the flow direction. Unidimensional fluid flow was reported in in most of the tests: uniform along the width of the strip without significant fluid race-tracking along the fabric edges. The compaction displacements were obtained by averaging throughout the width of the AOI ($\approx$ 10 mm) the data provided by digital image

correlation. The acquisition time of the digital cameras was set to 10 and 60 images per minute for VARI (in-plane flow) and SCRIMP (in-plane and out-of-plane flow), respectively, to take into account that the fluid flow along the vacuum bag surface was faster in the latter.

In all the cases, the infusion tests were carried out in two stages. The first one is the filling phase, in which the infusion fluid propagates through the dry fiber preform. Once the flow front reached the outlet gate, the inlet gate is closed by mechanical clamps and the post-filling phase begins, leading to a progressive homogenization of the thickness within the infused area, accompanied by a reduction in the fluid pressure as the load is transferred back to the fiber bed.

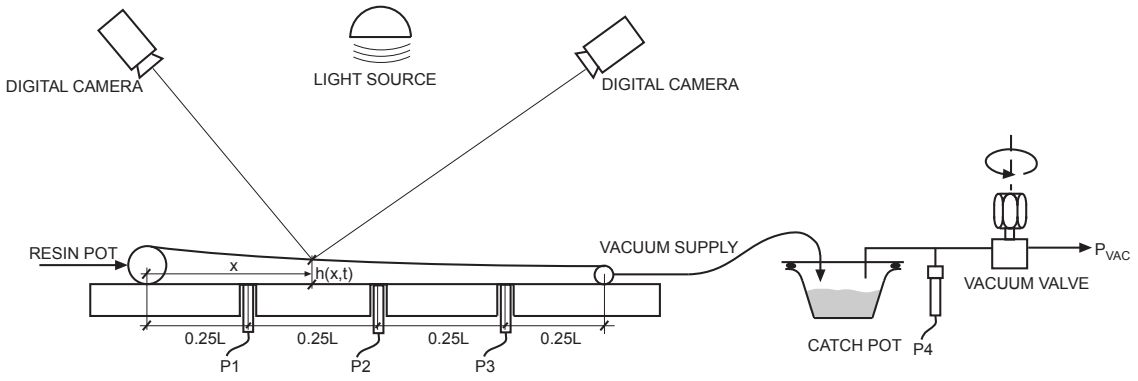

FIGURE 3.2: Sketch of the experimental infusion set-up and of the digital image correlation system.

3.1.1 Infusion experiments without distribution medium

Standard VARI experiments were carried out without distribution medium using the three lay-up configurations aforementioned ($[0°]_2$, $[0°]_4$, $[0°]_8$). The fluid viscosity, initial thickness and reference vacuum pressure measured prior to each infusion test are presented in Table 3.1. The total duration of the filling and post-filling stages is also included in the table for the sake of completion. The filling times t_f for the three thicknesses were similar indicating a

homogeneous progression of the flow front which took approximately $\approx$ 130 minutes in all cases. Minor variations in the $[0°]_2$ fabric can be probably endorsed to small fluid leaks along the longitudinal edges.

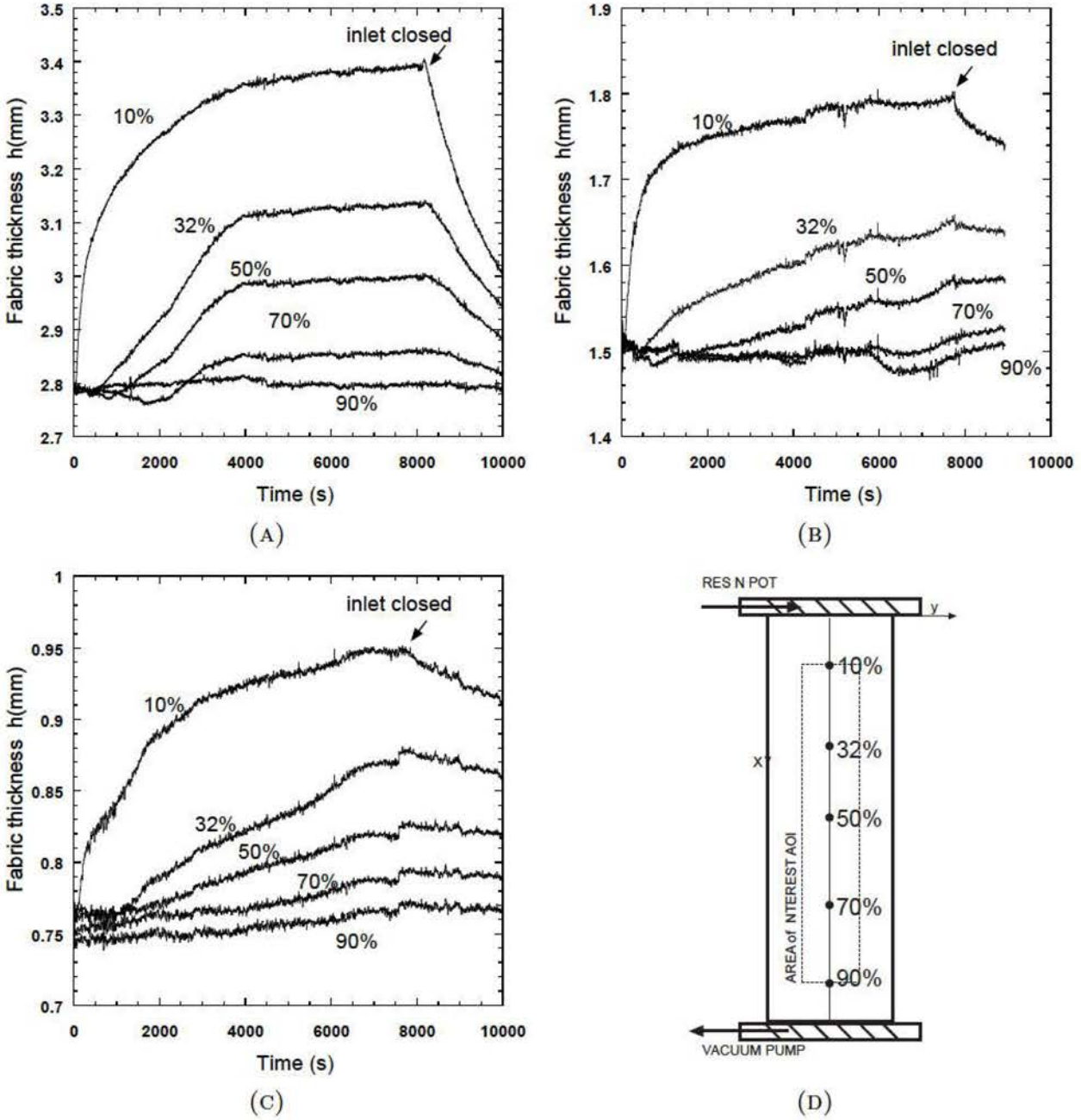

FIGURE 3.3: Evolution of the vacuum bag thickness with time during infusion at different positions of the strip located within the AOI. Experiments carried out without distribution medium: A) $[0°]_8$ B) $[0°]_4$ C) $[0°]_2$ D) Sketch of the panel with the different positions.

TABLE 3.1: Parameters of the infusion experiments without distribution medium

Parameter	$[0°]_8$	$[0°]_4$	$[0°]_2$
Viscosity μ [Pa s]	2.35	2.5	2.25
Filling time T_f [s]	8160	7760	7590
Post-Filling time T_p [s]	10000	8940	10000
Initial thickness h_0 [mm]	2.8	1.5	0.75
Reference vacuum pressure p_0/p_{atm} [1]	0.93	0.92	0.92

The evolution of the vacuum bag thickness with time at different bag positions (located at 10, 32, 50, 70 and 90% along the infusion line within the AOI) is shown in Figure 3.3 for the three different thickness of the fabric preform. In all the positions, the final thickness increased during the infusion time until the fluid reached the outlet gate and the post filling phase started. A slight reduction of the local thickness was detected as soon as the fluid entered into the bag, which is usually attributed to fluid lubrication of the fiber bed at the flow front. Wet yarns were more prone to undergo relative sliding within the fabric producing additional compaction without an increase of the external applied pressure. Afterwards, the bag thickness increased continuously due to the stress transfer between the fiber bed and the infusion fluid. The external load induced by the atmospheric pressure, initially supported by the fiber bed skeleton, was progressively transferred to the fluid leading to a spring-back effect with the corresponding increase of the fabric thickness. These effects (compaction followed by spring back) during infiltration were also reported by other authors, [53, 54]. The preform thickness variation during infusion was 0.6, 0.3 and 0.2 mm for the $[0°]_8$, $[0°]_4$, $[0°]_2$ fabrics, respectively (Figure 3.3). In all the cases, the maximum thickness variation was detected in the first gage point at 10% of the infused length.

The pressure build-up in the fluid, p_{fluid} was recorded by the transducers installed on the mold surface and is plotted in Figure 3.4 for the three fabric thicknesses. The pressure build up was very fast as soon as the fluid reach the corresponding transducer position and rapidly attains an asymptotic value once the steady state regime is established and the whole fabric is filled by the fluid.

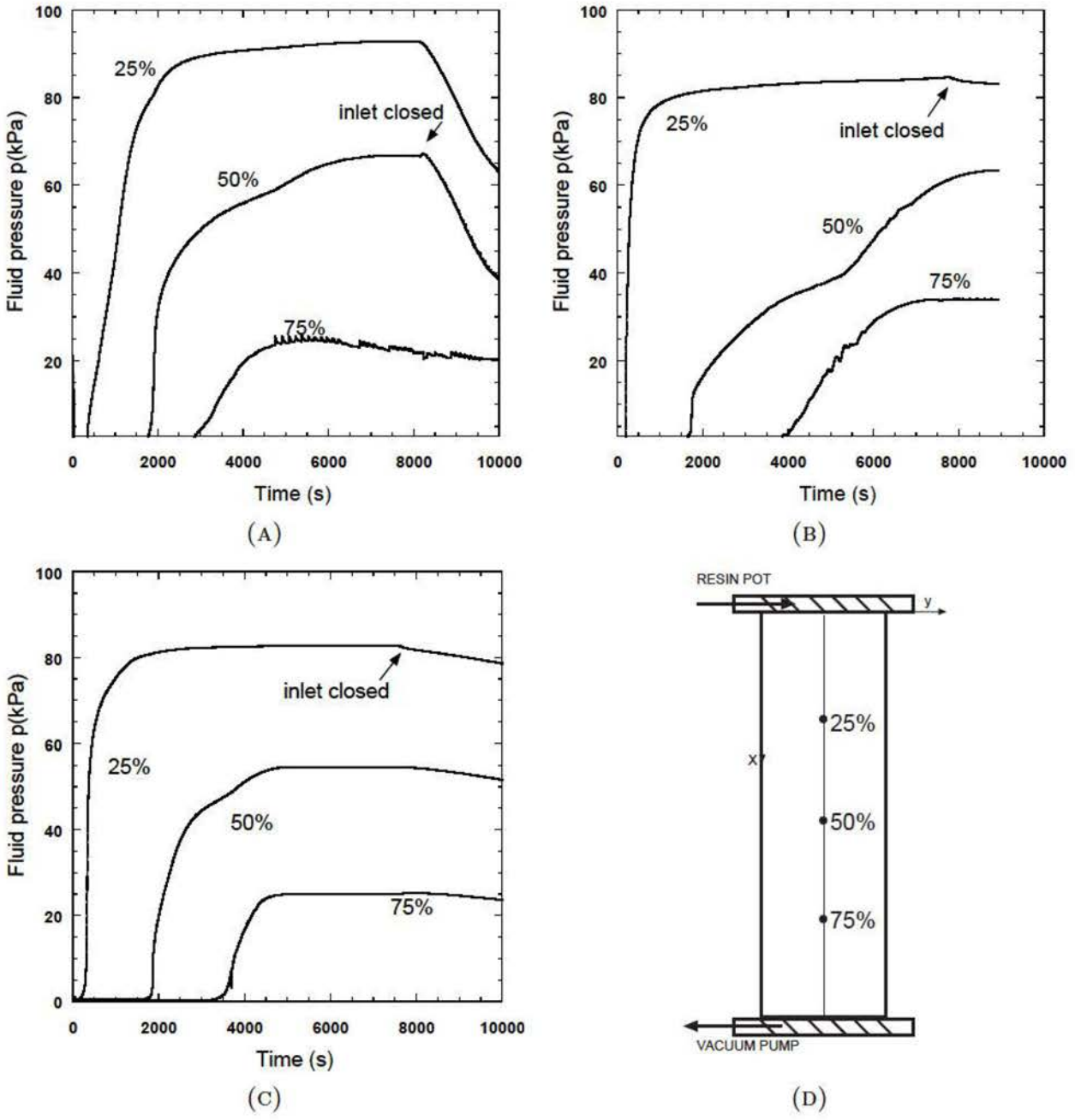

FIGURE 3.4: Evolution of fluid pressure at different positions of the strip located within the AOI. Experiments carried out without distribution medium: A) $[0°]_8$ B) $[0°]_4$ C) $[0°]_2$ D) Sketch of the panel with the position of the pressure transducers.

Permeability and compaction play a key role on the shape of the vacuum bag during the infusion. When the resin enters through the inlet gate, part of the vacuum pressure is transferred directly to the resin, releasing the fiber fabric, which in turn leads to a significant

increase of the fabric permeability. This results in a non-linear evolution of the vacuum bag profile during the infusion which is clearly observed in Figures 3.5 a), b) for the three fabric thicknesses, which show the shape of the vacuum bag measured with digital image correlation at different instants during the filling stage. This figures clearly demonstrate that digital image correlation is able to capture accurately the progression of the fluid along the infusion length until the fluid front reached the outlet gate and the fabric was completely saturated. Very interestingly, digital image correlation was also able to capture the roughness of the E-glass plain woven fabric (the approximate tow width was ≈5 mm).

The information provided by digital image correlation allowed also the determination of the flow front position during the experiments even if the direct optical observation of the fabric was not possible due to the speckle pattern. This kind of information is crucial to ensure the fabric lay-up is fully saturated and no dry spots are formed during the infusion. According to the results showed in Figure 3.5, the thickness of the fabric initially decreased due to the lubrication of the fiber-to-fiber contacts and then increased as a result of the load transfer between the fluid and the fiber bed. The transition point between both phenomena (attained when the bag thickness reached zero after the initially thickness reduction due to lubrication) was used to track the actual position of flow front during infiltration. Following this assumption, the location of flow front with time is plotted in Figure 3.6 for the different fabric thicknesses. As it was mentioned previously, filling times were similar for the three fabric thicknesses and also the time to saturate the panel (≈ 3000s) indicating similar flow progression mechanisms irrespective to the number of layers.

3.1.2 Infusion experiments with distribution medium

A second set of experiments was designed to understand the stress transfer between the infused fluid and the fabric in the presence of a distribution medium film on top of the laminate. The parameters used in the experiments are summarized in Table 3.2 for the different fabric thicknesses. The distribution medium is a highly permeability porous material

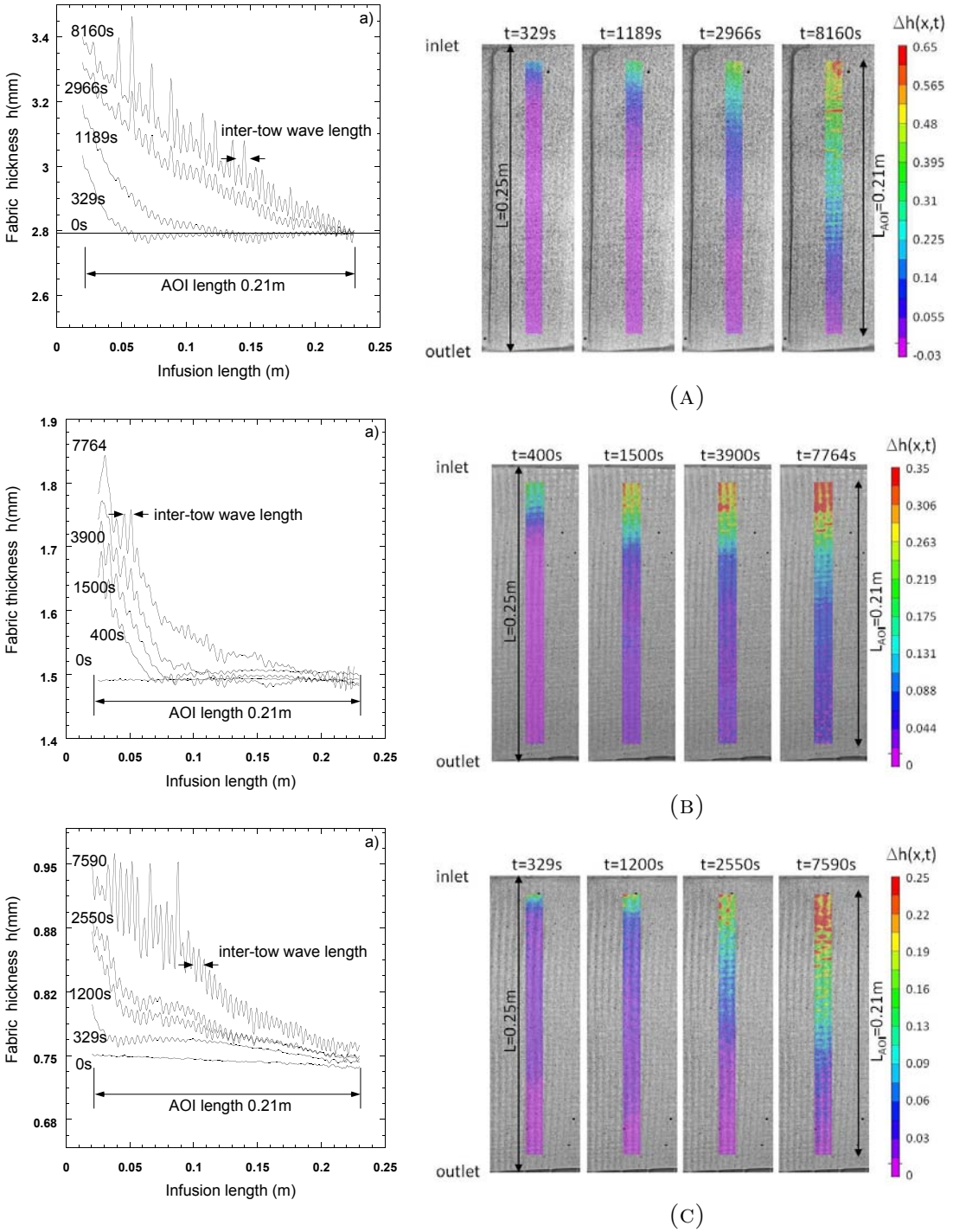

FIGURE 3.5: (a) Evolution of the bag thickness profile along the infusion length within the AOI for different infusion times.(b) Contour plot of the increment in the fabric thickness, $\Delta h(x,t)$, within the AOI for different infusion times. A) $[0°]_8$ B) $[0°]_4$ C) $[0°]_2$.

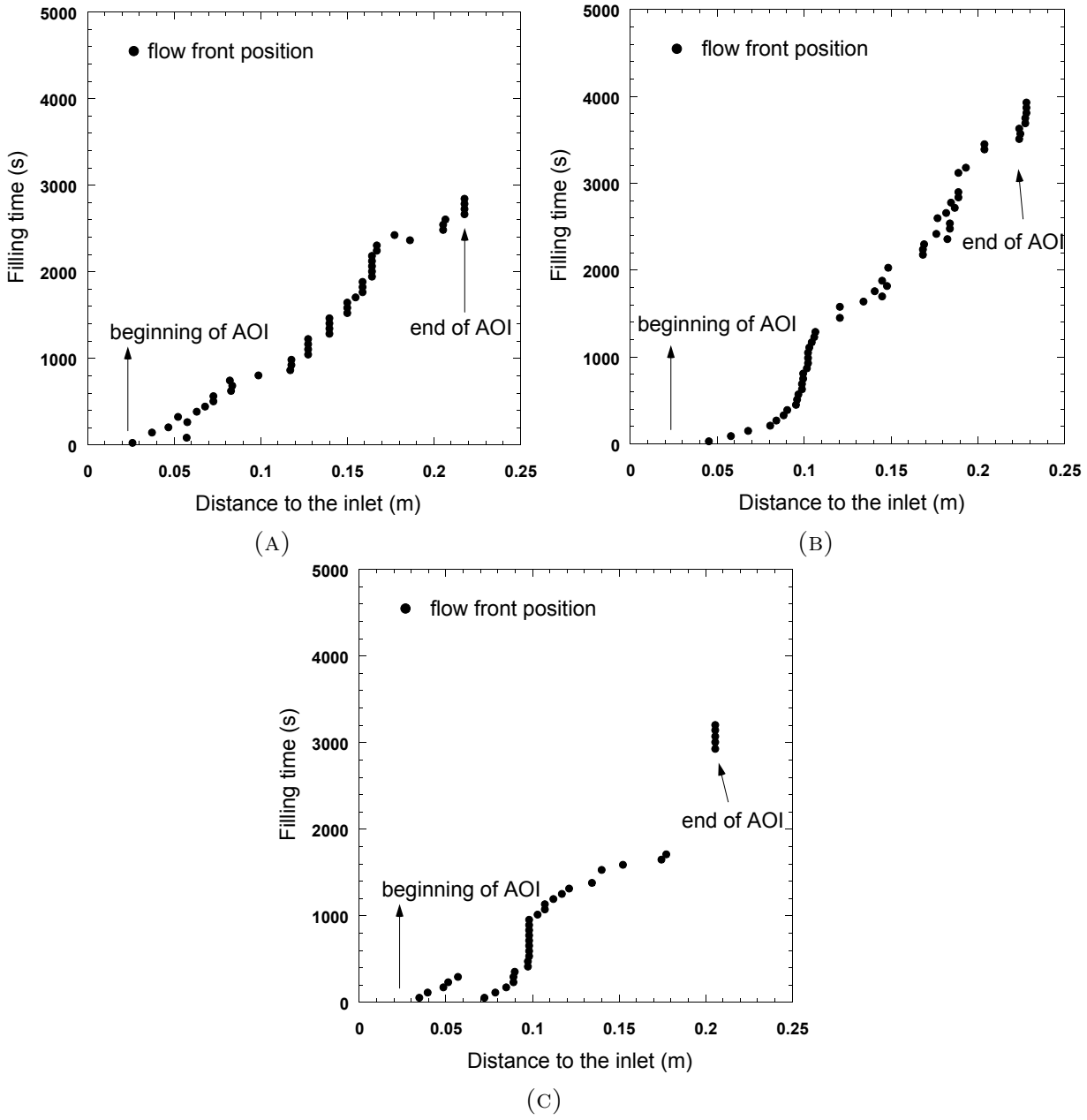

FIGURE 3.6: Evolution of the flow front with filling time. A) $[0°]_8$ B) $[0°]_4$ C) $[0°]_2$.

that leads to a fast fluid propagation along the upper surface of the laminate. As a result, fluid infusion takes place both in-plane and through-the-thickness, Figure 3.7, leading to a reduced filling time as compared with in-plane flow in the absence of the distribution medium. The velocity of flow front depends on the pressure gradient ($\approx \Delta p/L$ where L is the infused length) and decreases with the infused length L under in-plane flow, leading

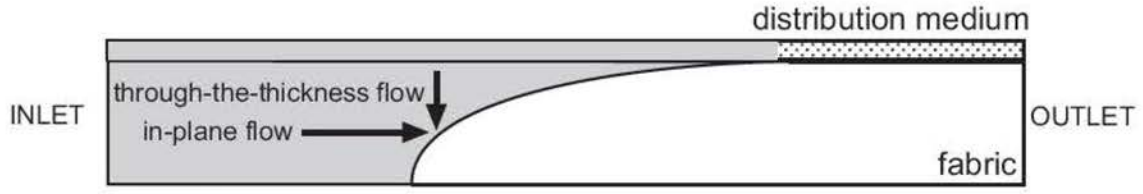

FIGURE 3.7: Sketch of the two-dimensional flow propagation in experiments carried out with distribution medium.

to very long filling times for large parts. Assuming incompressible (non-deformable) fabric behavior, the filling time can be obtained by direct integration resulting in

$$t_{filling} = \frac{\mu \phi L^2}{2 p_0 K_x} \tag{3.1}$$

where K_x stands for the in-plane permeability of the fabric, μ the fluid viscosity, ϕ the fabric porosity and p_0 the reference pressure. The former expression (equation 3.1) shows that the filling time scales with the square of the infused length L^2 resulting into a prohibitive manufacturing strategy for large composite parts. In such cases, the optimization and localization of the infusion/venting ports becomes crucial in order to reduce the filling times while the appropriate processing window is maintained well below the resin gelification. The use of a distribution medium reduces considerably the filling times by substituting in-plane flow with a faster through-the-thickness infiltration mechanism. This manufacturing method also known as SCRIMP (Seemann Composites Resin Infusion Molding Process) provides substantial benefits with respect to the in-plane flow propagation.

TABLE 3.2: Parameters of the infusion experiments with distribution medium.

Parameter	$[0°]_8$	$[0°]_4$	$[0°]_2$
Viscosity μ [Pa s]	1.3	2.0	1.5
Filling time T_f [s]	547	400	152
Post-filling time T_p [s]	700	500	250
Initial thickness h_0 [mm]	2.8	1.5	0.75
Reference vacuum pressure p_0/p_{atm}	0.93	0.93	0.93

The infusion filling times using the distribution medium were ≈6 times lower when compared with the standard vacuum infusion without distribution medium for an infusion length of 25 cm, showing the effectiveness of the distribution medium. The filling times divided by fluid viscosity also depended on the laminate thickness (from 101.33 $1/Pa$ for the thinnest $[0°]_2$ laminate to 420.77 $1/Pa$ in the $[0°]_8$ laminate) suggesting that the thickness of the laminate plays an important role. Again, by assuming incompressible (non-deformable) fabric, the estimated $fillingtime/viscosity$ when flow propagates from the top to the bottom of the laminate can be estimated as

$$\frac{t_{filling}}{\mu} = \frac{\phi h^2}{2p_0 K_z} \tag{3.2}$$

where h and K_z are the fabric thickness and the out-of-plane permeability, respectively. The experimental results obtained, Table 3.2, showed an almost linear ($\propto h^{1.132}$) dependence of the filling time with the fabric thickness in the thickness range analyzed, Figure 3.8. This effect could be attributed to various reasons. Firstly, the fabric will not behave as a perfectly incompressible porous solid because the effect of the compaction pressure on the out-of-plane permeability is not known *a priori* and, therefore, the quadratic dependence could be partially relaxed. Secondly, the out-of-plane permeability is strongly dependent on geometrical features such as ply shifting and it can increase with the number of layers under some circumstances, [55, 56] for equal fiber volume fraction. The effect of ply shifting becomes predominant for the thinnest laminates, being the flow channels hindered when the maximum nesting occurs (plies perfectly out-of-phase) or enabling direct and highly permeable channels for the case of minimum nesting. However, thicker laminates are more prone to produce random nesting configurations.

The evolution of the vacuum bag displacement with the filling time was also measured by digital image correlation and the results are plotted in Figure 3.9. The overall shape of the vacuum bag displacement is different when compared with the experiments carried out without distribution medium. The effect was specially evident in the thicker laminates $[0°]_8$

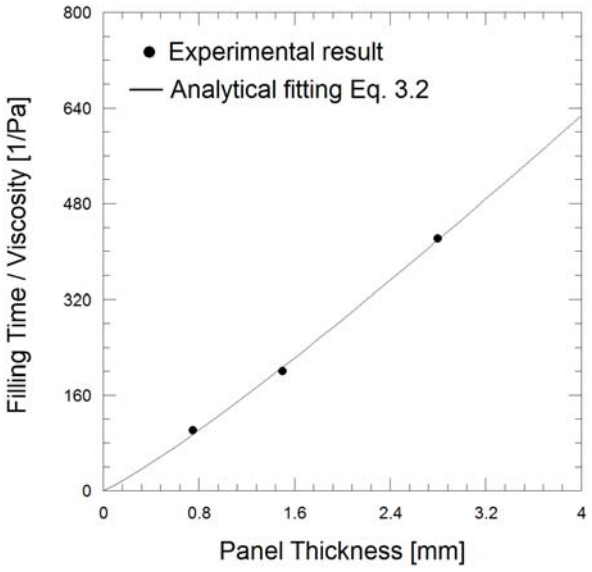

FIGURE 3.8: Thickness dependence of the filling times (divided by fluid viscosity) for infusion experiments carried out with distribution medium.

, Figure 3.9 A) where the bag displacement evolution showed an interesting change of trend. The displacement measured at a given position was initially dependent only on the position along the laminate length. However, the bag displacement increased afterwards until a second stabilization plateau occurred when the flow reached the entire laminate length and the fabric was completely impregnated. The double stabilization curve is observed for any of the positions (10, 32, 50, 70 and 90%) along the laminate length although with an obvious decreasing amplitude.

The mechanisms behind this effect can be the combination of the flow mechanisms (in-plane and out-of-plane) in operation when using the distribution medium, Figure 3.7. In these tests, the flow progresses first within the distribution medium and leads to the initial fabric thickness increase due to the stress transfer. This initial bag displacement is a consequence of a non-homogeneous deformation distribution in the thickness of the fabric, that affects only the impregnated upper layers of the laminate. In these layers, the fluid share the compaction pressure relaxing the fiber bed and producing this initial increment of the fabric thickness. This stage ends when the lagging in-plane flow exceeds the corresponding measurement

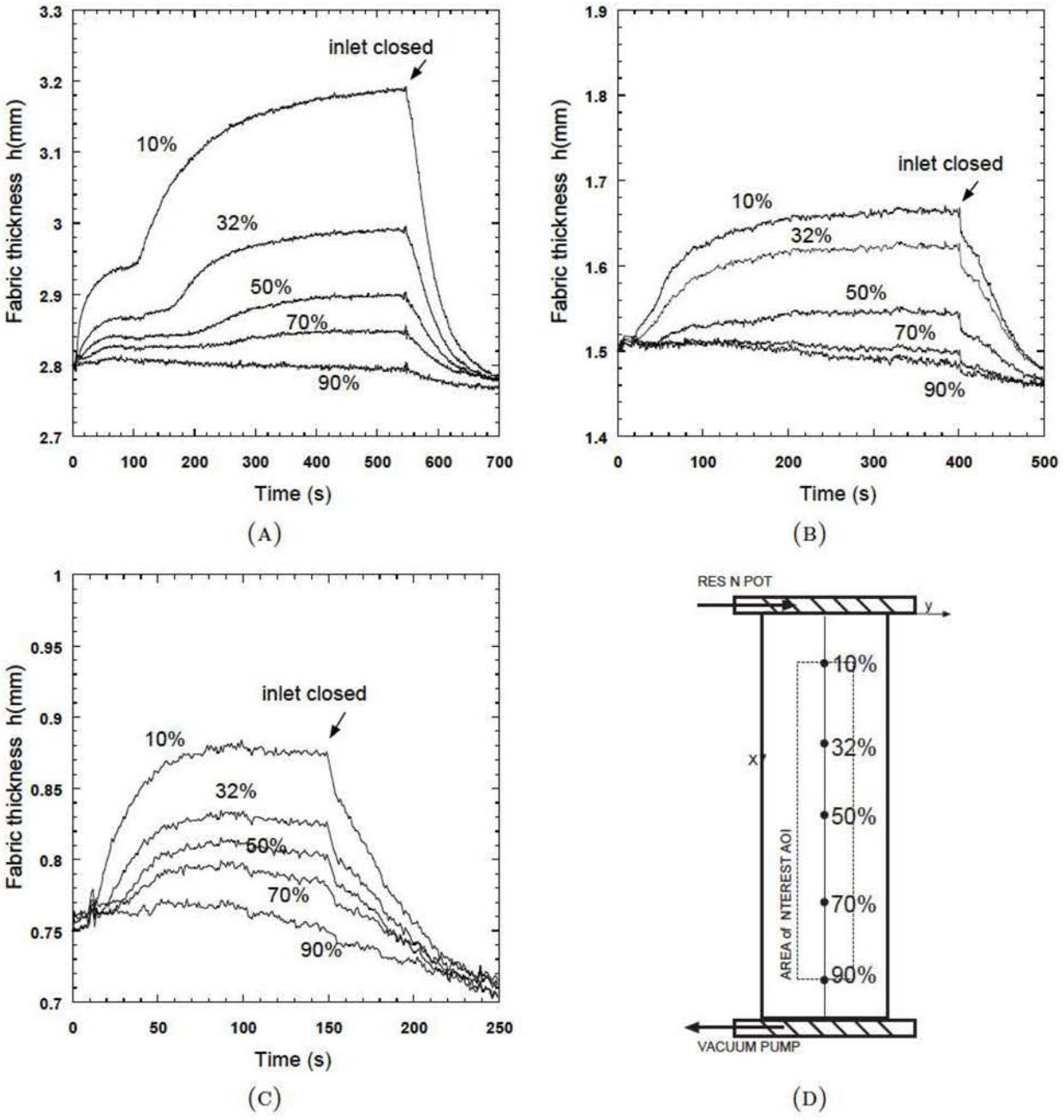

FIGURE 3.9: Evolution of the vacuum bag thickness with time during infusion at different positions of the strip located within the AOI. A) $[0°]_8$ B) $[0°]_4$ C) $[0°]_2$ D) Sketch of the panel with the different positions.

position and the entire fabric thickness is saturated by the fluid. This latter assumption was also corroborated by the fluid pressure transducers that recorded a sudden increase of the readings when the in-plane flow passes through its position.

The fabric deformation was not stabilized after the inlet gate was closed. Moreover, the experimental results suggested the fabric thickness converges to a stable value below the initial one, (Figure 3.9) and this effect was not observed in the case of in-plane infusion, Figure 3.3. It should be emphasized that resin is not in equilibrium and flow continues after the filling stage is finished requiring some time for the pressure to become uniform along the part length. Moreover, the basic difference of post-filling stages in both set of experiments, with and without distribution medium, is the ability of the distribution medium to act as a fluid reservoir exchanging flow with the fabric, [25]. In this presence of the distribution medium, the fluid can be squeezed out from the fabric producing and additional compaction as compared with standard infusion experiments without distribution medium.

The preform thickness variation during infiltration in the presence of the distribution medium (0.4, 0.2 and 0.12 mm for the $[0°]_8$, $[0°]_4$, $[0°]_2$ fabrics, respectively, Figure 3.9) was slightly lower than that without distribution medium. The overall shape of the vacuum bag corresponding to different times during the filling stage is shown in Figure 3.10 a) in combination with the contour plot of the increment in the fabric thickness, $\Delta h(x,t)$, Figure 3.10 b) for the same infusion times. The overall shape was similar to that found without distribution medium. Very interestingly, the roughness of the E-glass plain woven fabric was not clearly detected in these tests as the vacuum bag was not in direct contact with the infused fabric and the undulations were mainly attributed to the roughness of the distribution medium. The flexible vacuum bag bridged in this case the empty spaces between the yarns of the distribution medium allowing to exchange fluid with the fabric during the post-filling stage acting as a bleeding layer.

3.2 Infusion parameters

This section compiles all the experimental techniques developed in this thesis to determine the main processing parameters governing the fluid infusion process through the E-glass fabric preform. As it was mentioned above, the compaction phenomena occurring during

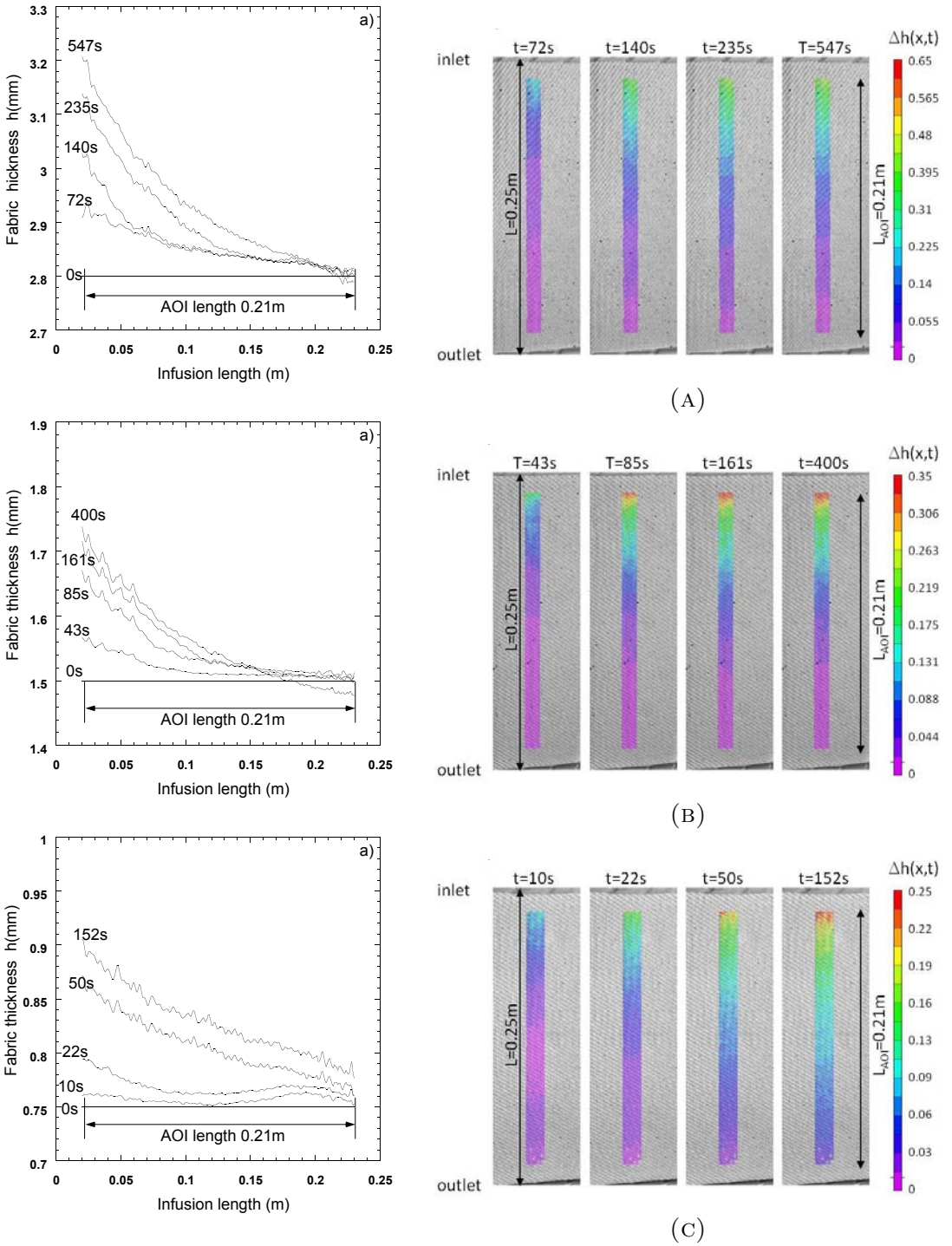

FIGURE 3.10: (a) Evolution of the bag thickness profile along the infusion length within the AOI for different infusion times. (b) Contour plot of the increment in the fabric thickness, $\Delta h(x,t)$, within the AOI for different infusion times. A) $[0°]_8$ B) $[0°]_4$ C) $[0°]_2$.

infusion is a consequence of the stress transfer between the fiber bed and the infused fluid. Fluid propagates through the porous medium according to the Darcy's equation which essentially states that the resistance to the flow depends on the fabric permeability factor, the fluid rheology and the pressure gradient. Therefore, a set of detailed experiments was carried out to measure the fabric permeability and the resin rheology. In addition, fiber bed compaction behaviour is also measured since fiber volume fraction plays a critical role in the permeability.

3.2.1 Fluid characteristics

Thermoset resins, such as polyesters, vinylesters and epoxies. are frequently used for vacuum infusion of composite parts. These resins are assumed to behave as incompressible newtonian fluids whose behaviour is independent of the shear strain prior to the gelation point [57]. Afterwards, the viscosity increment due to cross-linking makes the analysis of the infusion process difficult to analyze. For this reason, it is preferred to use other infusion fluids such as non-activated thermoset resins, silicone oils or corn syrup water blends. Among them, corn syrup blends were selected due to the cleanliness and ease of use. Besides, the viscosity of the fluid is stable to small fluctuations of the laboratory room temperature ($\approx 25°C$) and can be easily tunned by adjusting the water to syrup ratio. In this thesis, blends with $(70\% - 80\%)$ of corn syrup were used in all the infusion experiments. They were assumed to behave as incompressible newtonian fluids. The fluids were degassed in a vacuum chamber prior to the infusion tests and the viscosity was measured at room temperature (Table 3.1 and 3.2).

The ability of a liquid to maintain the contact with a solid surface is commonly known wetting and is the result of the molecular interactions between the three phases involved in the process (liquid, gas and solid). The degree of wetting between E-glass fiber and corn-syrup was measured by the sessile drop test method. The method is based on the force balance analysis of a liquid drop on a solid surface. These forces lead to a contact angle which is the result of the thermodynamic equilibrium between the three phases involved.

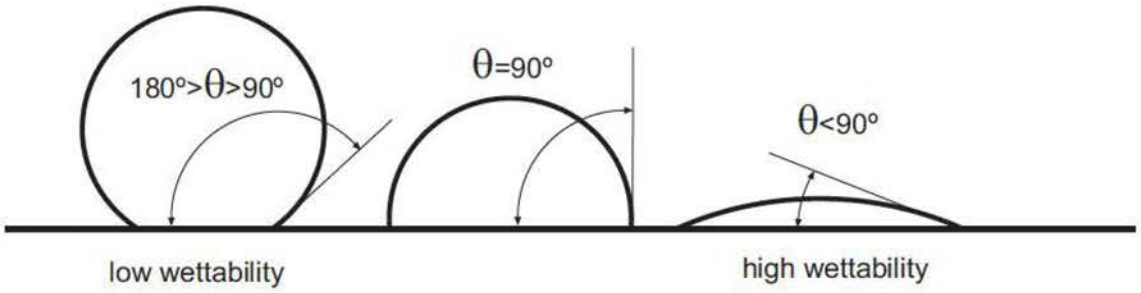

FIGURE 3.11: Sketch of the wetting angle between solid and liquid

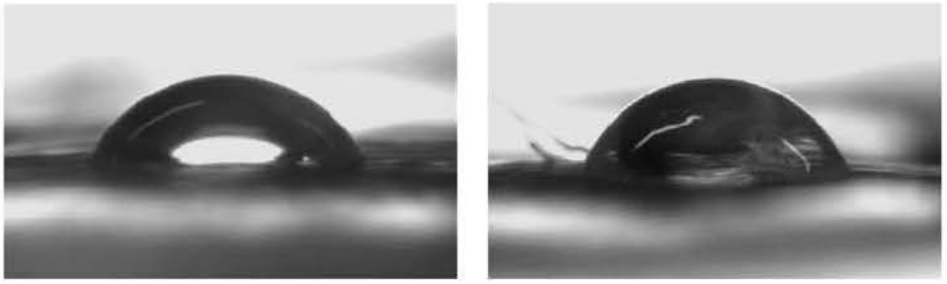

FIGURE 3.12: Contact angle between E-glass fabric and a drop of corn syrup fluid (80%).

Depending on the contact angle, the degree of wetting can be classified as (Figure 3.11): high wettability when the contact angle is $\theta < 90°$ and low wettability when $90° < \theta < 180°$. The contact angle between corn syrup drops placed on E-glass fabric was measured using a video-based optical system Neurtek OCA 15EC (Figure 3.12) yielding a contact angle of $78.5° \pm 6.5°$. This is indicates that the fluid partially wet the E-glass fiber surface.

The surface tension of corn syrup blends is assumed to be constant and equal to 0.0808 N/m because is not strongly affected by the water content [58]. Hence, the yarn impregnation process is assumed not to be influenced by the water content in the corn syrup blend $(70\% - 80\%)$. According to the Young-Laplace equation, positive capillary pressure is expected to control the impregnation process although significant discrepancies were found when impregnating single E-glass yarns by vacuum infusion, as it will be shown in Chapter 4.

3.2.2 Fabric permeability

Permeability is probably the most important property to assess liquid molding of composite materials. It measures the resistance to the viscous flow through a porous medium under a given pressure gradient according to the Darcy's equation. The measurement of the permeability properties of dry fabrics present enormous experimental difficulties which are related with the fabric architecture (in-plane and through-the-thickness), the compaction and the actual fiber volume content, fluid characteristics, saturated/non saturated flow [59], etc. which introduce an important experimental scatter. As a result, there is no standard procedure although important efforts has been made to address this problem [60]. Not surprisingly, differences of more than 100% are found in the literature for the same dry fabric and impregnating fluid among different laboratories that even use the same experimental methodology.

The common approach for in-plane characterization of the fabric permeability is a RTM mold based on Darcy's law [59, 61], in which the fabric preform is located inside the cavity (Figure 3.13). This set-up allows to measure the permeability for different cavity thicknesses in one single experiment by means of a piston. The aluminium mold is machined into the dimensions of the panel 250 x 100 mm and closed by a PMMA cover which is transparent and allows to check if the flow is uniform and there is not race-traking [62, 63]. The mold is sealed by a silicon ring carefully placed between the PMMA wall and the mold allowing free slip in the vertical direction. The mold has two inlets and one vent connected to a milled channel at each side of the mold, as shown in the sketch of Figure 3.13. These channels create an uniform flow front during the filling from the two inlets.

The permeability fixture is connected to a universal electromechanical testing frame Instron 3384 equipped with a 10 kN load cell (Figure 3.14). A stainless steel beam supported by two screws is used to connect the testing frame to the PMMA plate allowing a good pressure distribution over the fabric surface. The cavity thickness is controlled using a 10 mm linear variable displacement transducer LVDT. Finally, the inlet is connected to the

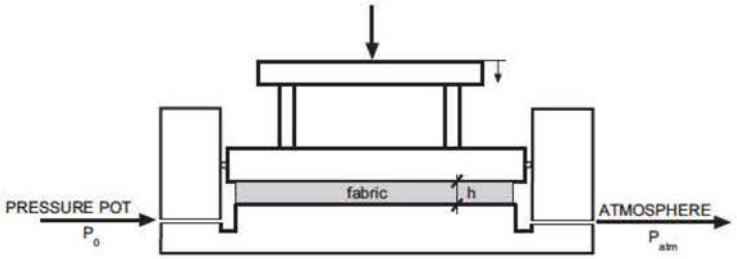

FIGURE 3.13: Sketch of the experimental set-up for the in-plane permeability tests.

injection pressure pot controlling the injection pressure while the outlet drains the fluid directly to a bucket placed over the plate of the balance. The flow rate is calculated using the mass time variation recorded with the balance.

FIGURE 3.14: Experimental permeability set-up.

In-plane permeability factors were measured in the E-glass fabric lay-ups ($[0°]_8$ B) $[0°]_4$ C) $[0°]_2$) oriented in the warp (0°), weft (90°) and 45° directions. The inlet pressure, p_0, is increased in several steps (0.25, 0.5, 0.75 and 1.0 atm) while the outlet is maintained at atmospheric pressure, p_{atm}. The fluid flow rate (obtained from the fluid mass and density) of the corn syrup blend was measured for each imposed pressure gradient. All the experiments

were carried out under fluid saturated conditions using different thicknesses corresponding to fiber volume fractions in the range 40 to 60%.

The permeability factor was computed from the experimental variables as

$$K_i = \frac{\phi}{h}\frac{\mu L}{\rho W}\frac{Q_m}{\Delta p} \tag{3.3}$$

where Q_m is fluid mass flow, ϕ the porosity of fabric ($V_f = 1 - \phi$), ρ and μ are the density and viscosity of the infused fluid, respectively, and Δp is the pressure differential between the inlet and outlet. L, W and h are, respectively, the length, width and thickness of the mold cavity. It should be mentioned that fiber volume content was adjusted by selecting the mold cavity thickness h with the displacement of the actuator of the electromechanical testing frame.

The results for three different lay-up configurations with 8, 4, and 2 layers are plotted in Figure 3.15. In all the cases, the permeability factors decreased with the fiber volume fraction because the higher the volume fraction of fiber reinforcement, the smaller the channels for the fluid flow, hindering the progression of the viscous flow. The experimental results followed the Carman-Kozeny equation [28],

$$K_i = k_{i0}\frac{(1 - V_f)^3}{{V_f}^2} \tag{3.4}$$

where k_{i0} is an empirical constant which depends on the specific fiber bed architecture, (Table 3.3). In all the cases, the permeability factors measured along the warp and weft directions were very similar, while slight variations were found in the 45° orientation, indicating that the plain woven fabric was well balanced. The results also showed that the permeability factor decreased with the number of layers and this effect can probably endorsed to the nesting effects near the mold surface where the yarns are not contacting properly. This poor yarn contact could create areas of high local porosity that facilitate the fluid flow parallel to

TABLE 3.3: Permeability factor experimental fitting parameters and regression factors.

	8 Layers			4 Layers			2 Layers		
Parameter	$[0°]_8$	$[45°]_8$	$[90°]_8$	$[0°]_4$	$[45°]_4$	$[90°]_4$	$[0°]_2$	$[45°]_2$	$[90°]_2$
k_{i0} ($\times 10^{-10}$m^2)	2.41	1.78	2.36	4.57	4.03	4.57	11.75	7.77	9.72
R	0.95	0.99	0.98	0.97	0.99	0.99	0.99	0.98	0.99

the mold surface in a kind of race-tracking disturbance. Thus it was assumed that the most accurate permeability factors correspond to the experiments with 8 layers and they are used for all the simulations of the Chapter 5.

The permeability factor of the distribution medium was also determined with the same methodology. In this case, a single layer of the distribution medium network was used. Different fiber volume fractions were analysed in the range of 11-15% by adjusting the mold cavity thickness with the actuator of the electromechanical testing frame. The results are depicted in Figure 3.15 and clearly show that the permeability of the distribution medium was independent of the fiber volume fraction, at least in the vacuum infusion range, and it is assumed equal to 1.4×10^{-8}m^2.

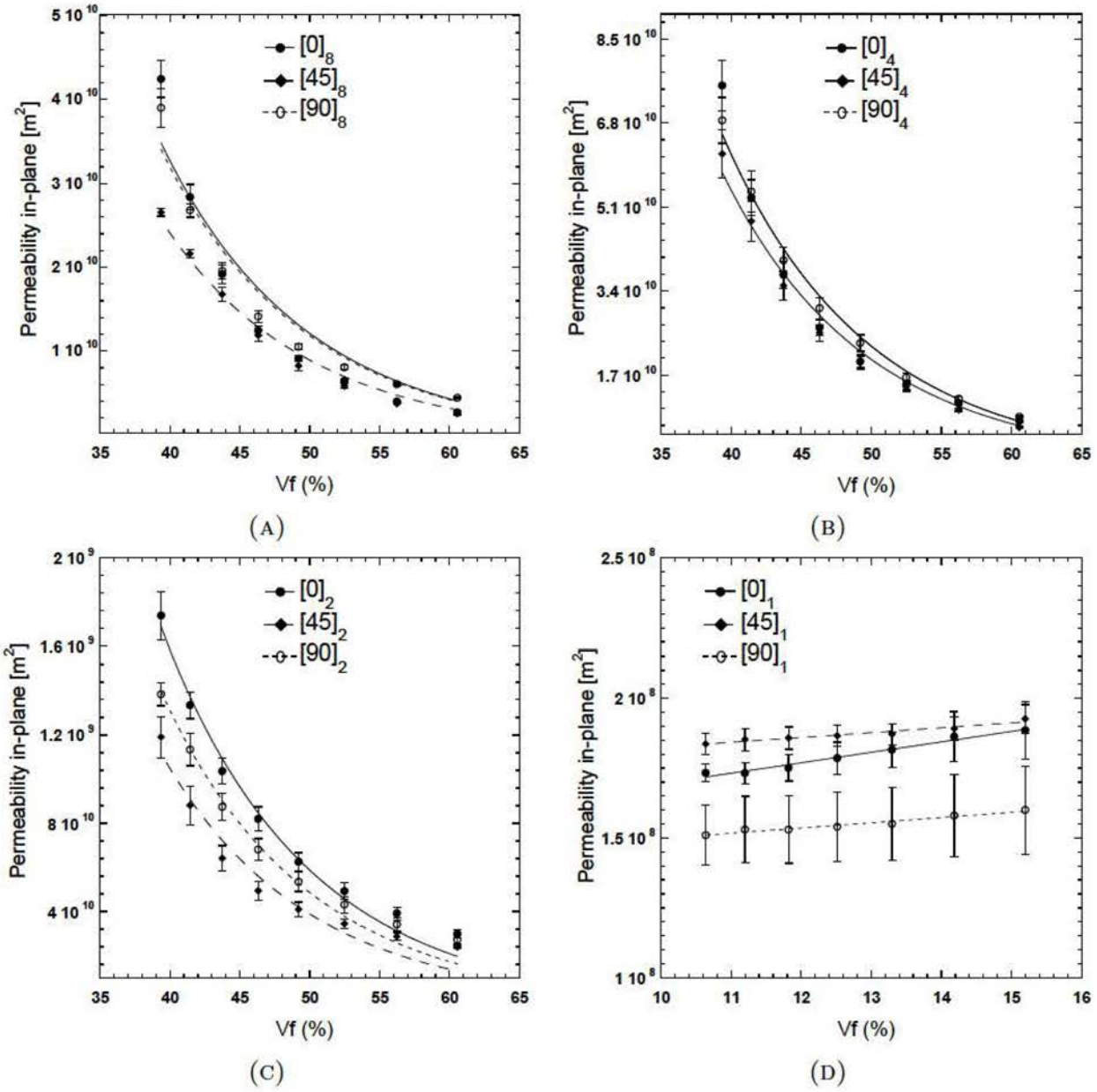

FIGURE 3.15: Variation of the in-plane permeability factor with the fiber volume fraction V_f for different stacks configurations: A) 8 Layers, B) 4 Layers, C) 2 Layers of E-glass fiber and D) Layer of distribution medium. The lines in A) B) C) corresponding to the fitting of the experimental data with the Carman-Kozeny equation 3.4.

3.2.3 Fiber bed compaction

The compressibility of the preform is another of the key factors affecting the final quality of composite materials manufactured by vacuum infusion. Fiber bed compaction tests, in dry and wet conditions, were carried out in this thesis to understand the compressive response of the E-glass woven fabric and to obtain the basic constitutive equations for modeling purposes. Different approaches concerning the compaction characterization of fabrics are reported in the literature. Among them, the direct compression test using universal testing frames is the most common [64], although other people use the standard vacuum infusion test using displacement gauges to measure the preform deformation [65]. In this thesis, an improved approach based on these last set of experiments was used to determine the fiber bed compaction curve my means of digital image correlation.

The experimental set-up was similar to the one used in a standard vacuum infusion experiments. A laminate of 250 x 80 mm^2 was consolidated using a single vacuum port without fluid ingress. After stabilization of the vacuum pressure inside the bag, the laminate is subjected to a homogeneous pressure which is controlled by the external vacuum valve. A sequence of compaction cycles was imposed to determine the compressibility of the preform. The compaction displacements were measured using digital image correlation by averaging the results over the area of the laminate.

During the compaction process, different phenomena occur simultaneously. Basically, the compaction curve of a dry fabric exhibits three different regions [66]. Firstly, the linear region at very low strains due to the elastic deformation of the fiber network. This initial stage is followed by a highly non-linear region were irreversible fiber compaction, yarn nesting and accommodation takes place. In this region, the distance between the fibers decrease and the number of contacts between fibers growth until the final asymptotic behaviour is attained, which is similar to the elastic deformation of a porous-like structure. This last stage establishes the maximum compaction that the fabric is able to sustain during manufacturing.

The compaction behaviour of the fiber bed is different for dry and wet conditions [67]. During dry experiments, hysteresis loops are formed due to the irreversible change of individual positions of fibers and yarns during the compaction [68]. Yarn nesting decreases the fiber bed compaction due to ply-to-ply non matching fabric undulations. When the fluid wets the fibers, there is a lubrication phenomenon leading to an additional rearrangement of the fibers. Such lubrication effects also decrease the inter-ply nesting and hence the panel can be compacted more than in the dry experiments. In addition, the hysteresis loops are not observed anymore.

During the tests, images of the panel were acquired at the different pressure levels. The pressure levels are controlled using the vacuum valve and measuring the fluid pressure by means of cavity sensors as in standard vacuum infusion tests (Figure 3.2). The characterization of the compaction curve for wet fabrics required fewer pressure steps than under dry conditions conditions due to the absence of hysteresis loops. In this later case, the fiber bed pressure ($\sigma_{fiber} = p_0$) was applied in steps of 5, 10, 20, 40, 60, 80 and 90 kPa from the initial unloaded state to achieve several complete load-unload cycles. The wet fabric experiments started by opening the inlet gate and allowing the fluid to ingress until the fabric was fully saturated. After several minutes, the load-unload process was repeated. In this case, the fabric pressure was determined by means of the Terzagui's equation from the pressure differential between the vacuum port and the cavity sensor inside the bag ($\sigma_{fiber} = p_0 - p_{fluid}$). The pressure steps applied in this case were 5, 30, 50, 60 and 80 kPa.

The fabric compaction, or thickness decrease, was determined in all the cases from the images acquired during the loading-unloading steps by means of digital image correlation. To this end, the bag displacement were averaged over the area of interest AOI of the panel. The fiber volume content was computed from the total areal weight of the corresponding lay-up and the thickness variation according to

$$V_f = \frac{\rho_A N}{\rho_f (h_0 + \Delta h)} \tag{3.5}$$

where N stands for the number of layers of the laminate, $h_0 + \Delta h$ is the final thickness after compaction, and ρ_A and ρ_f are the areal weight of the fabric and the density of the E-glass fibers used in the experiments, respectively (Table 3.4).

TABLE 3.4: Properties of woven E-glass fabric preform

Parameter	
Areal density of fabric ρ_A $[Kg/m^2]$	0.49-0.51
Fiber E-glass density ρ_f $[Kg/m^3]$	2540
Fabric porosity ϕ	0.48

The compaction curves, fiber volume content *vs.* applied pressure, of the different E-glass lay-ups ($[0°]_8$, $[0°]_4$, $[0°]_2$) are plotted in Figure 3.16 for the dry and wet preforms. The curves correspond to the loading-unloading cycles of the dry fabric experiments and the loading portion of the wet experiments. The maximum dry fabric compaction measured was in the range of 50-55% although a slight increase in the $[0°]_4$ and $[0°]_8$ lay-ups was observed. This effect can be attributed to nesting during fabric compaction. The hard contact between the yarns and the mold surface prevents their accommodation which is favoured in the presence of multiple plies. Hysteresis loops are also evident, especially during the first cycles. Wet preforms could be compacted to higher volume fractions than dry experiments illustrating the effect of lubrication. The experimental data of compaction experiments obtained in the dry and wet condition were fitted to a power law expression as suggested in the literature [19].:

$$V_f = a\sigma_{fiber}^{b} \tag{3.6}$$

where b is the stiffening index, and a the fiber volume fraction corresponding to 1 KPa of net pressure acting on the fiber bed. The corresponding fitting parameters are presented in Table 3.5. The results obtained for the compaction of wet fabrics will be used as inputs to model vacuum infusion.

TABLE 3.5: Compaction parameters in wet/dry conditions of E-glass fabric and distribution medium.

Parameter in wet/dry	$[0°]_8$	$[0°]_4$	$[0°]_2$	$[0°]_1$ DM
a (%/KPa)	44.58/48.98	46.02/49.12	46.41/46.256	10.97/10.866
b	0.0642/0.0285	0.0454/0.0238	0.0345/0.0288	0.0539/0.0369
R	0.996/0.987	0.956/0.985	0.885/0.993	0.994/0.909

The experiments were repeated including a single layer of the distribution medium. In this case, the compaction of the distribution medium is negligible with respect to the fabric compaction (Figure 3.16) and, therefore it can be assumed as incompressible for the range of applied pressures.

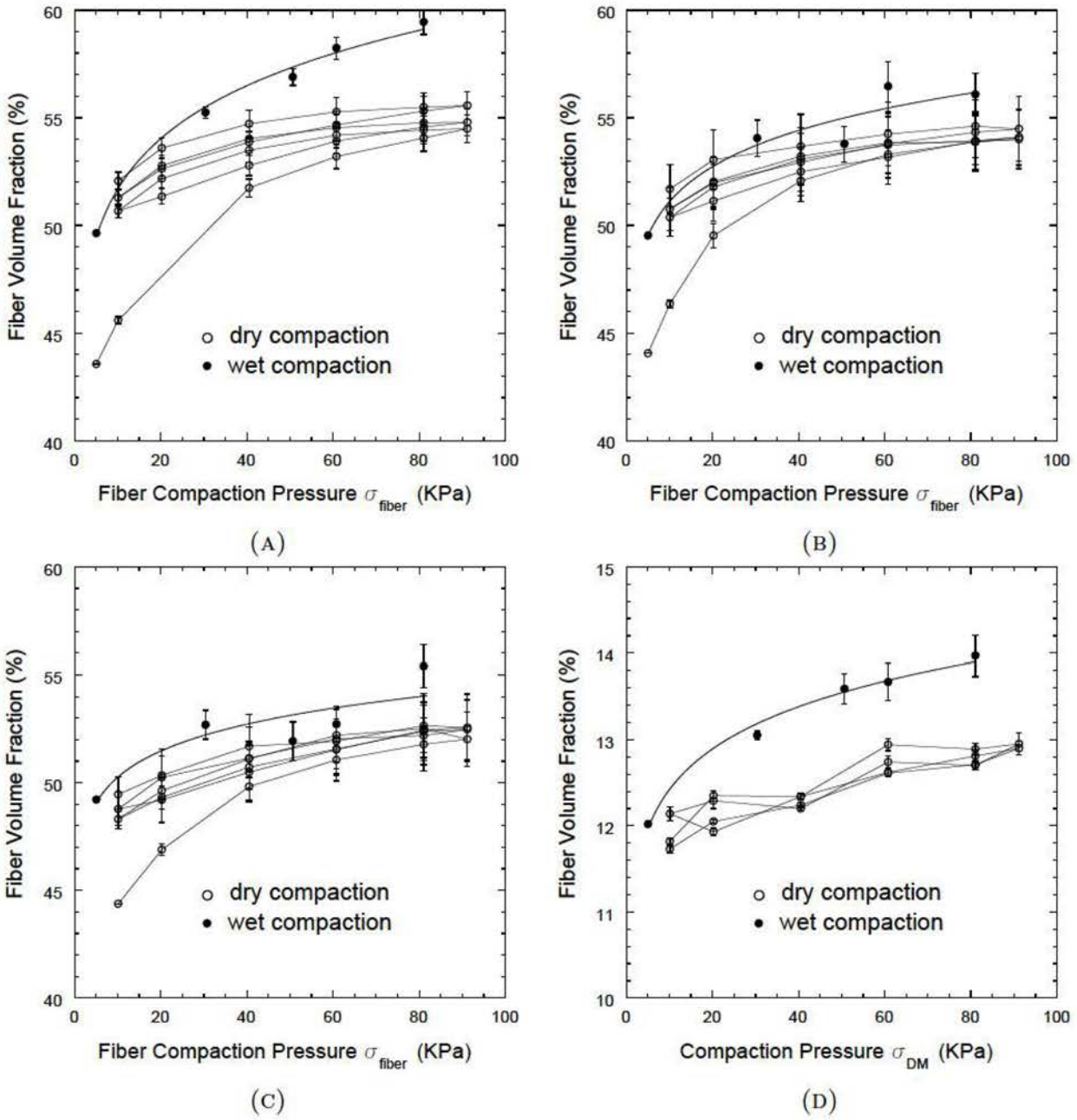

FIGURE 3.16: Compaction curves of dry and wet conditions of E-glass fabric preforms. A) $[0°]_8$ B) $[0°]_4$ C) $[0°]_2$ and D) $[0°]_1$ one layer of distribution medium. The lines stand for the fitting of the experimental results to equation 3.6.

"In moments of crisis, only imagination is more important than knowledge"

Theoretical physicist Albert Einstein

Chapter 4

In situ characterization of microflow

A novel approach, based on *in situ* vacuum-assisted infiltration experiments in a synchrotron beamline, is presented in this chapter to investigate the mechanisms of microflow and void transport at tow scale [69]. Synchrotron X-ray computed tomography (SXCT) was used to study the mechanisms of microfluid flow within a E glass fiber tow using an apparatus designed and built for this purpose. The high resolution of the SXCT images allows the detailed reconstruction of individual fibers within the tow while the contrast between the different phases (air, fluid and fibers) was enough to track the fluid front position and shape as well as the void transport during infiltration. The ability of this technique to provide detailed information of microfluid flow and void transport in composite materials is clearly established. The fluid propagation at the microscopic level as well as the mechanisms of void transport within the tow were related to the wetting between the fluid and the fibers, the rheological properties of the fluid and the local microstructural details (fiber volume fraction, fiber orientation) of the fiber tow.

4.1 Background

The major drawback of liquid molding techniques for composite processing, with respect to the autoclave consolidation of prepreg laminates, is the generation of voids and air entrapments during infiltration, which reduce significantly the mechanical properties of the composite. Macrodefects result from dry or poorly impregnated zones that appear when the resin flow reaches the outlet gate before completely the filling the component. They are due to an inadequate distribution of the injection/infusion/venting ports in the component. In addition, microdefects (voids) can also develop, even if the part has been completely filled with resin during infusion. Standard reinforcements used in composite manufacturing are produced by tows containing thousands of fibers in specific fabric architectures (unidirectional, woven, non-crimp, stitched, etc.), leading to microporosity (the free space in between individual fibers within the tow) and mesoporosity (the free space between tows). Viscous flow dominated by the resin pressure gradient takes place through the high permeable channels between adjacent fiber tows while tow impregnation perpendicular to the fiber is mainly driven by capillary forces if the fibers are wetted by the liquid. This dual-scale flow (micro-meso) is partially responsible for the generation of voids during liquid molding of composite parts because of the competition between viscous and capillary forces [36–39].

Previous experimental observations have demonstrated that void formation in engineering composites depends on the ratio between viscous and capillary forces through the non-dimensional modified capillary number, Ca* [40–43]

$$Ca^* = \frac{\mu \bar{v}}{\gamma cos\theta} \tag{4.1}$$

where μ and $\bar{v}$ stand, respectively, for the resin viscosity and the average resin velocity, while γ and θ are the fluid surface tension and the contact angle, respectively. An optimum capillary number to minimize the void content has been found in specific material systems [43]. Viscous forces are dominant with respect to capillary ones for large capillary numbers

($Ca* > 10^{-2}$) and the rapid flow of the resin through the tow-to-tow free gaps leads to the formation of voids within the tows, as air entrapments cannot scape. On the contrary, the fluid velocity between tows is smaller for low capillary numbers ($Ca* < 10^{-3}$), and the wicking effects caused by the intra-tow capillary forces become dominant. Under these conditions, fiber tows are rapidly filled with resin and air entrapments are generated between tows.

Obviously, understanding the resin flow mechanisms is crucial to manufacture composite parts with minimum porosity by liquid molding and the selection of the appropriate experimental technique to monitor accurately void generation and transport is a critical part of this process. Macroscopic resin flow measurements can be performed by direct image monitoring in transparent acrylic molds during RTM [40, 70–74] or on the surface of the vacuum bag in VARI [36]. The author Vilà [75] tracked the position of the resin flow front in VARI by measuring the changes in the fabric thickness, associated with the resin-fabric stress transfer during infusion, by means of digital image correlation. Dielectric sensors [76] or embedded optical Bragg sensors, based on the change of the refractive index of the surrounding media when the fabric is infiltrated, can also be used to track resin flow and curing at discrete points [77, 78]. Other authors have used C-scan ultrasounds when resin progress through the fabric [79]. The infusion experiments were carried out with the vacuum bag immersed in a water tank and the resin flow was stopped at different times. Fully and partially saturated regions were tracked by C-scan by averaging the signal attenuation in the through-the-thickness direction of the laminate. This technique can also be used to monitor the flow propagation in the through-the-thickness direction in thick fabrics to determine the out-of-plane permeability [80]. All these techniques provide valuable information about the macroscopic flow propagation in a composite part during the infusion/injection process but their low spatial resolution cannot analyze the microflow process within the tow.

To overcome these limitations, Magnetic Resonance Imaging (MRI) can be used to track the front flow by mapping the fluid concentration inside porous samples of cm dimensions [81]. Neacsu et al. [82] carried out MRI measurements to study capillary-driven transverse flow

in bundles of aligned fibers using blends of water and corn syrup with protonated liquids. The evolution of the wet portion of the fiber bundle with respect to time was obtained and compared with analytical models of fluid propagation. Endruweit et al. [83, 84] determined the local fluid concentration using MRI during impregnation of several fabrics, including woven, non-crimp and triaxial braids, detecting local variations attributed to the microvoid formation at the tow level as well as dry spots.

X-ray radiography has also been used to track the progress of the fluid during infiltration due to the difference of X-ray absorption coefficients between the fibers and the fluid [85]. The two-dimensional information provided by radiography can be very useful to track the progress of the fluid front but it is not suitable to analyze the development of porosity, particularly at the microlevel. X-ray computed tomography (XCT), in which a set of radiographies obtained at different angles are used to obtain a three dimensional reconstruction of the object, is much more appropriate to track of porosity during infiltration. This technique has been successfully applied to study damage in composites [86, 87], as well as to analyze the effect of processing conditions in the porosity of composite materials [88–91]. Moreover, the resolution of this technique (in the range of μm) is adequate to detect intratow and intertow voids, including information about their size, shape and spatial distribution.

To the author's knowledge, XCT has not been used to monitor the infiltration process at the microscale in composite materials and this work is intended to establish the advantages and limitations of this technique for this particular problem. To this end, a miniaturized apparatus for vacuum infusion was designed and built to study *in situ* the infiltration mechanisms operating at the micro-scale in a XCT synchrotron beamline. These conditions are representative of the fluid flow in textile preforms under low capillary numbers in which the wicking effects due to capillary forces are dominant with respect to viscous flow. The fluid propagation at the microscopic level as well as the mechanisms of void transport within the tow were related to the wetting between the fluid and the fibers, the rheological properties of the fluid and the local microstructural features (local fiber volume fraction, fiber orientation) of the fiber tow.

4.2 Experimental details

The vacuum infusion apparatus was described in Chapter 2. The miniaturized device allows to study small specimens consisting of one to three fiber tows within the detector FOV of the X-ray system (approximately 40 mm in length by 3.8 mm wide). The sample was a single fiber tow of 2K (1000 tex) extracted from a plain woven fabric of E glass (average fiber diameter $16 \pm 2\mu m$), which was placed in between two standard vacuum bag films of about $64\mu m$ in thickness (NBF-540-LFT) thermally sealed at the edges, Figure 4.1 b). The vacuum bag and fiber tow assembly was 25mm in length with an irregular cross section of 4mm in width and 0.5mm in thickness, Figure 4.1 c). The sample was placed between the inlet and the outlet, connecting both ends with the respective syringe needles, and sealed with standard tacky tape (LTT-90B). Thus, the sample contained in the vacuum bag film was completely sealed at the edges (by thermal sealing) and borders (by tacky tape) at the infusion and vacuum points. The whole system was mounted on an aluminium support connected to the vacuum system. Vacuum pressure of $\approx$ 0.91 x 10^5 Pa was applied with a rotatory vane pump connected to the vacuum line to avoid leaks during the tomographic measurements. The vacuum pressure was continuously monitored during the *in situ* experiment. The infusion tow was encapsulated within a PMMA cylinder (at atmospheric pressure inside the cylinder) to provide mechanical stability to the infusion device and to protect the X-ray system against fluid spills without significant X-ray attenuation.

The fluid infusion is controlled by a simple regulation system made up of a screw and a nut with washer. Initially, the nut and the washer block the syringe piston preventing fluid propagation driven by the vacuum. The infusion driven by vacuum can progress by rotating the nut of the screw. In this way the flow front can be controlled accurately by adjusting the nut rotations and the total amount of fluid infused can be controlled step-by-step with the thread pitch. This is critical because any parasitic fluid propagation through the sample during the acquisition time of the tomograms (due to negligible leaks at the vacuum and infusion ports or other sources) will lead to image artifacts and blurring in the reconstructed

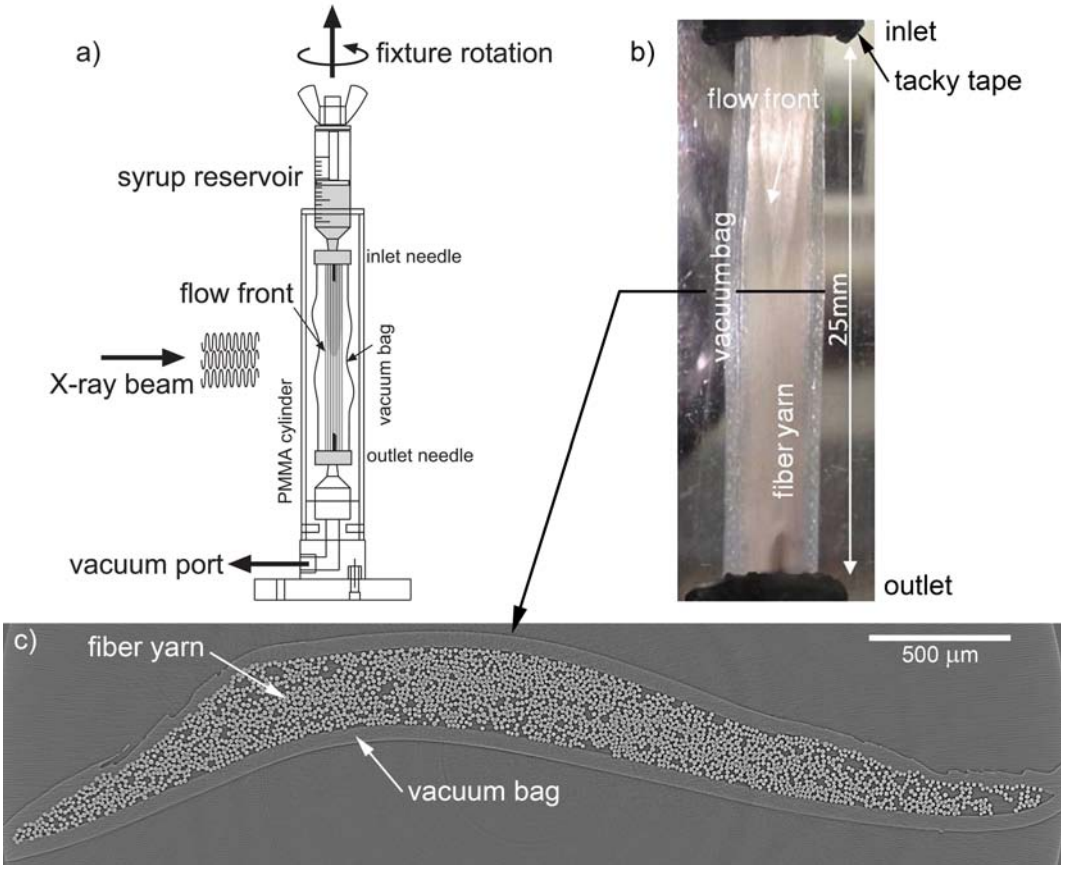

FIGURE 4.1: a) Sketch of rotating apparatus for tow infusion in the XCT synchrotron beamline. b) Detail of the infused tow and of the flow front position. c) XCT cross section of tow and of the vacuum bag before infiltration.

volumes, that can preclude the adequate spatial resolution of the different phases (fibers, fluid and air entrapments). Gravitational effects could also be discarded (negligible Bond number, *Bo* [92]) for the size of the capillaries between individual fibers. The acquisition time for each tomogram was about 2h (see below).

A blend of water (30%) and syrup (70%) was used as infusion fluid. The blend was degassed immediately before the infiltration for 20 minutes in a vacuum container. The viscosity of the fluid, μ =0.35 Pa·s, was measured with a rotational viscosimeter Fungilab with L2 type spindle at 30 rpm at ambient temperature. The static fiber-fluid contact angle, θ =78.5 $\pm$ 6.5°, was measured optically with an OCA 15EC Neurtek apparatus while the surface tension, $\gamma \approx 80$ mJ/m^2 was obtained from well-established values in the literature [58]. Under these

conditions, the modified capillary number during infusion can be estimated from equation (1.17) as

$$Ca^* \approx \frac{K_{\parallel} \Delta p / \Delta x}{\gamma \cos\theta} \tag{4.2}$$

where $\Delta p \approx 0.7$ atm is the pressure gradient, $\Delta x \approx 2.5$ cm the average infusion length and $K_{\parallel} = 2.6 \times 10^{-12}$ m^2 the tow permeability parallel to the fibers that was obtained from the Gebart model for an average fiber volume fraction of 54% [10]. The average fiber volume fraction was calculated from the tomograms of the cross-sections along the tow. The fiber area was determined from the number of pixels corresponding to the fibers, which was divided by the total tow area. The average fiber volume fraction was fairly constant along the tow. According to equation (4.2), $Ca^* \approx 6 \times 10^{-4}$, leading to a regime in which capillary forces are dominant over viscous forces.

The SXCT observation was focused in the infiltration mechanics during the infusion process. The *in situ* experiment was performed at the P05 beamline of PETRA III storage ring at the Deutsches Elektronen-Synchrotron (DESY) in Hamburg (Germany). The intense and coherent synchrotron beam was generated by an undulator which provides X-rays in energy range of 5 keV to 50 keV. A Si 111 double crystal monochromator was used to set the energy at 25 keV during the experiments. The flow was stopped by the blocked piston of the syringe and the infiltration device was rotated by 180° while recording the transmitted intensity by an X-ray CCD detector with an effective pixel size of 1.25 μm^2. The volumes were reconstructed with binning 2 leading to an effective pixel size of 2.5 μm^2. Motorized slits defined the horizontal and vertical beam sizes of 3.8 mm and 1.9 mm, respectively. Radiographies at different angles of the central region of the tow, located within the field of view of the X-ray system, were obtained three times during the experiment. The first one prior to infusion, the second one once the fluid front has advanced up to approximately the middle of the tow, and the third one after the tow was fully impregnated. Nine hundred radiographs with an exposure time of 300 ms each were collected in about 120 min. The

sample to detector distance was set to 37 mm which provided some degree of phase contrast to the reconstructions. The three dimensional microstructure was reconstructed using the standard filtered back-projection algorithm.

4.3 Results and discussion

Infusion experiments were performed using the experimental set-up described above. The mesoscopic flow front had a triangular shape mainly due to the anisotropic permeability of the fiber bundle and to the point infusion, Figure 4.1 b). According to the Gebart model [10], the longitude permeability is at least one order of magnitude larger than the radial one for a fiber volume fraction of 54%, leading to a two dimensional flow. However, preferential propagation of the fluid along the tow/bag interface was observed in several tests, as in racetracking.

4.3.1 Local fluid flow mechanisms

Figure 4.2 a) shows a cross section perpendicular to the fiber tow of the partially impregnated reconstructed volume where the different phases (fibers, fluid and voids) are clearly distinguished. It is worth noting that the high resolution of the SXCT images allows the detailed reconstruction of individual fibers within the tow while impregnated and dry regions of the tow can be distinguished. A nearly constant fiber volume fraction of ≈ 54 % was measured from different cross sections along the tow. This volume fraction is representative of the typical conditions during vacuum infusion manufacturing. The fiber volume fraction was only locally disturbed when voids were dragged along the fiber direction, as shown below.

The reconstructed volume of ≈ 1.8 mm in length included 753 slices perpendicular to the tow and allowed a detailed 3D reconstruction of the flow front at the microscale. Representative tomograms of the central region of the tow prior, during and after filling are depicted in

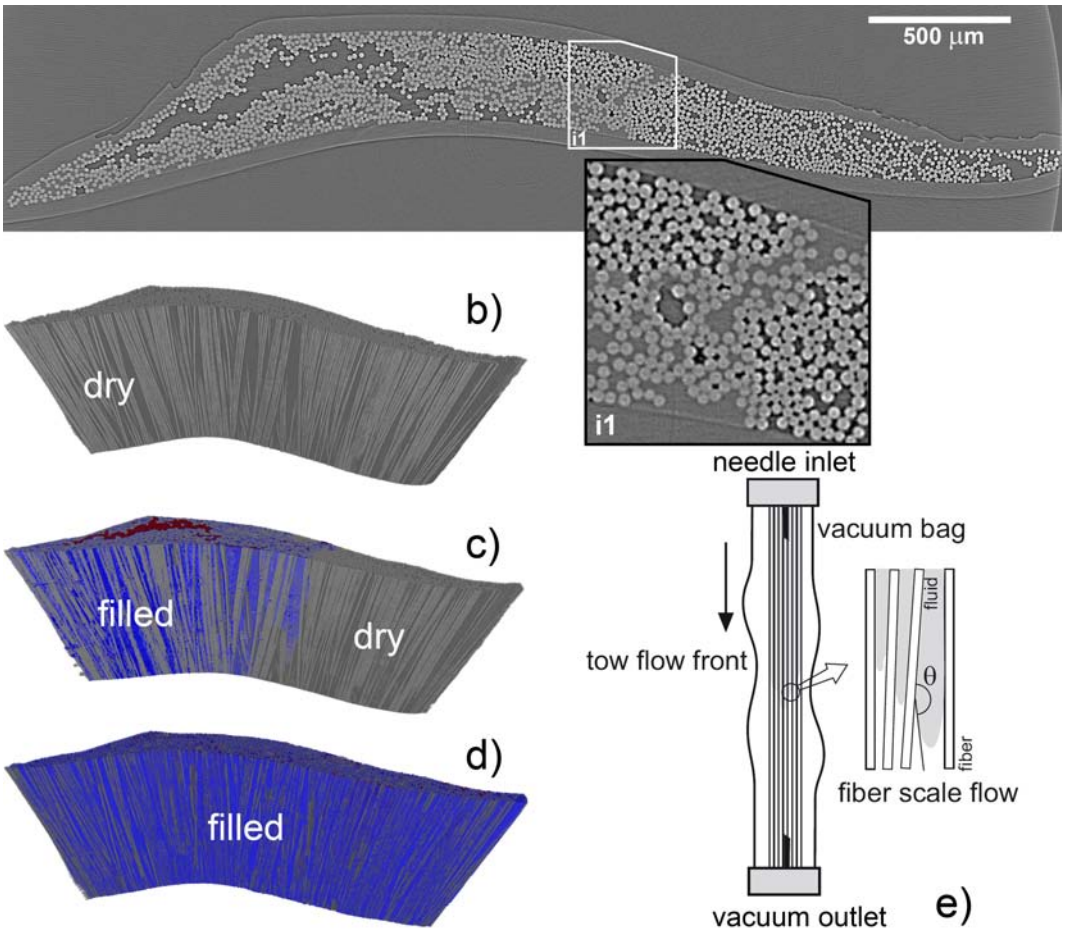

FIGURE 4.2: a) Cross section of the fiber bundle within the vacuum bag. Fibers and voids are clearly visible while the differences between dry and wet regions are visible in the inset *i*1. b) Detail of the fiber tow prior to the infusion. c) Detail of the partially impregnated fiber tow. d) Fully impregnated fiber tow. e) Sketch of the dual flow at the tow/fiber level observed during the impregnation experiments.

Figures 4.2 b)-d), respectively. The fluid is represented in navy blue while the internal void within the tow is shown in red in Figure 4.2 c). Air not corresponding to voids is shown as dark gray and fibers as light gray. The local distribution of fibers within the tow is inhomogeneous (fiber clusters and empty spaces are clearly shown) and fibers are not parallel and present convergent/divergent trajectories with significant twisting and meandering. As a result, flow progress along the bundle is inhomogeneous, leading to the formation of preferential channels in the fiber direction, Figure 4.2 c). Full impregnation of the tow is attained afterwards by the fluid flow perpendicular to the fibers from these preferential channels.

This sequence in the infiltration mechanisms is triggered by the differences in permeability and capillary forces between both orientations, although the relative trajectories of neighbor fibers play an important role because fluid flow along the channel formed by two convergent fibers is arrested by the drag capillary forces, Figure 4.2 e).

A first interesting observation provided by the *in situ* infusion experiments is related with the capillary forces and the shape of the meniscus formed at the flow front between adjacent fibers, 4.3. The local contact angle was measured at different positions across the fluid front, leading to an obtuse angle with an average value of $\approx 150°$, which indicates a non-wetting condition between the fluid and the fibers. This value is different from static contact angle of 78.5° measured optically, as indicated above. Similar discrepancies during vacuum infusion have been reported by other authors [93]. For instance, Li et al [94] studied the behavior of capillary forces during longitudinal impregnation of fiber yarns subjected to external and vacuum-driven pressure gradients with several infiltration fluids. They found out that the capillary pressure acted as a drag force for the infiltration under vacuum-assisted conditions for several fluids but this effect was not found if the stress gradient for infiltration was produced with compressed air. These authors attributed this behavior to dynamic effects because the capillary number Ca^* during infiltration was large. Verrey et al. [95] found similar dynamic effects on the contact angle, which were attributed to the fiber surface roughness increasing the real contact area or to the pinning of triple lines (gas-liquid-solid) by the sharp edges. Other authors [96] attributed this effect to the interaction of fiber sizing with the wetting fluid.

It should be remarked that SXCT measurements were carried out under quasi-static conditions and no fluid displacements were detected during data acquisition because they would have led to image blurring effects. As a result, the discrepancies in the contact angle between vacuum infiltration and air measurements cannot be attributed to dynamic effects and they are more likely associated with surface effects induced by fiber sizing in vacuum. This non-wetting fluid-fiber interaction during vacuum infusion leads to important effects in the local microflow distribution. Transversal fluid flow is easier in those areas where the

FIGURE 4.3: Longitudinal cross section of the impregnated tow showing trapped voids and the flow front meniscus. Local fiber misalignments with convergent/divergent trajectories are also visible.

dragging force against the infiltration is lower, and thus coincides with the channels with faster longitudinal flow.

A detailed quantification of the variations of the capillary pressure and the permeability was carried out from the local fiber volume fraction, V_f, obtained from SXCT. The fiber centers as well as their radius were determined and the local fiber volume fraction in the transversal section of the tow was computed assuming a fixed spot size equal to a fiber diameter. This spot size yields $V_f = \pi/4 = 78.5\%$ for a square-packed fiber arrangement. The local fiber volume fractions in three transverse cross-sections along the tow direction are shown in Figure 4.4 b). It should be noted that the minima of the local volume fraction are found in the perimeter, while the maxima are located in the center.

From these estimations of the local fiber volume fraction, the non-dimensional capillary pressure, $\bar{p}_c$, was determined according to Ahn et al. [97] and Pil-lai and Advani [98] as

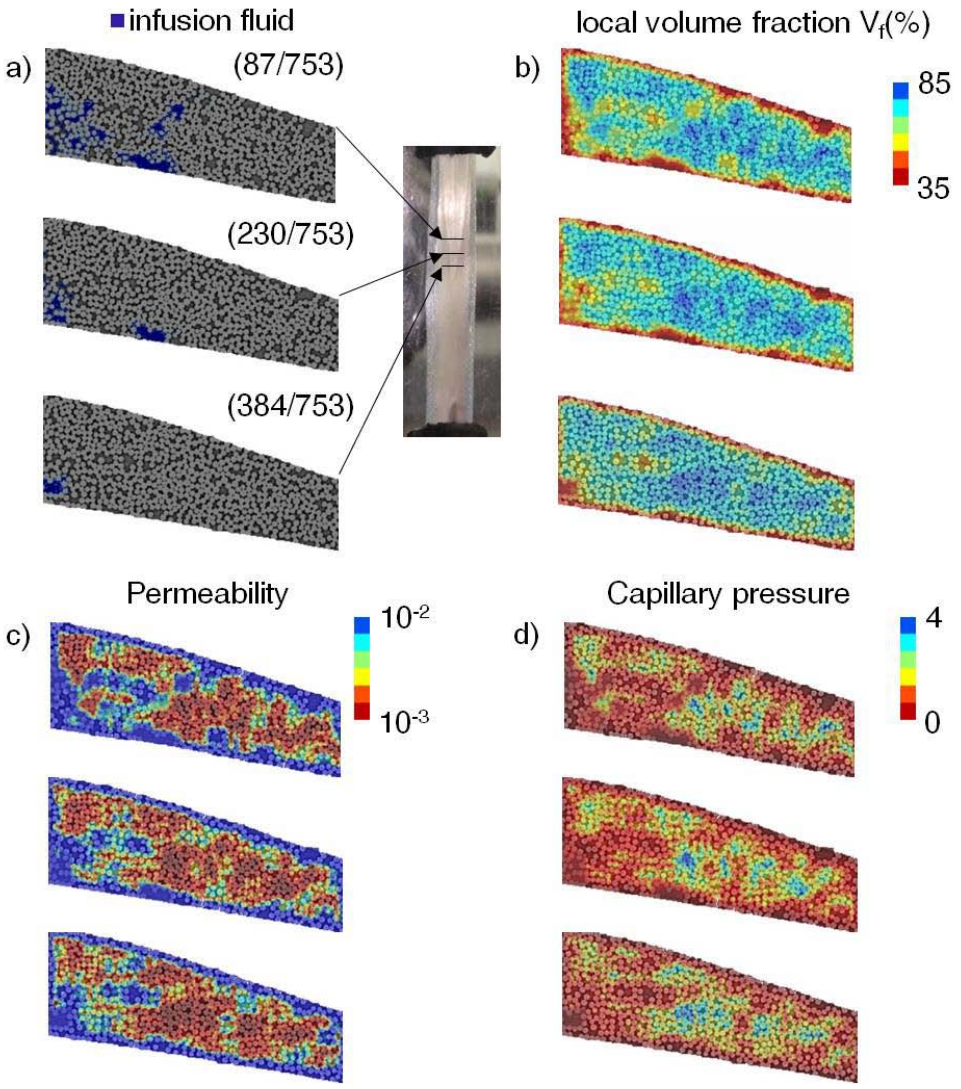

FIGURE 4.4: Transverse cross-sections of the tow obtained by XCT. a) Dry and wet regions, the latter shown in navy blue. b) Local fiber volume fraction, Vf. c) Longitudinal permeability factor, $\frac{K_{||}}{D_f^2}$, according to equation 4.4. d) Non-dimensional capillary pressure, $\bar{p}_c$, according to to equation 4.3

$$\bar{p}_c = \frac{p_c}{p} = \frac{Vf}{1 - Vf} \tag{4.3}$$

where $p = F\gamma \cos\theta / D_f$ and F and D_f stand, respectively, for the shape factor ($F = 4$ and $F = 2$ for longitudinal and transverse flow, respectively) and the fiber diameter, while γ and

θ are the surface energy and contact angle. The term $\bar{p}_c = V_f/(1 - V_f)$ in equation (4.3) represents, therefore, the effect of the microstructure on the capillary pressure distribution within the tow. In addition, the longitudinal permeability $K_{\|}$ of a set of unidirectional and parallel fibers was analytically derived by Gebart [10] as a function of the fiber volume fraction as

$$\frac{K_{||}}{D_f^2} = \frac{2}{57}\frac{(1 - Vf)^3}{Vf^2} \tag{4.4}$$

The longitudinal permeability factor, $K_{\|}/D_f^2$ and the non-dimensional capillary pressure, $\bar{p}_c$, are plotted in Figure 4.4 c) and d), respectively, for three cross-sections perpendicular to the tow at the same infusion time. The dry and wet regions in these cross sections at this instant are also shown in Figure 4.4 a). The regions in which the fiber volume fraction was low (mainly the tow perimeter) were areas of preferential longitudinal flow, leading to a kind of race tracking effect.

The differences in the capillary pressure between the regions with the highest ($\approx 80\%$) and lowest ($\approx 35\%$) fiber volume fraction were very large. Fluid flow in the transverse direction was not favored in regions with high fiber volume fraction while the longitudinal impregnation of the fiber clusters was impeded by the drag associated with the obtuse contact angle. Obviously, the mechanisms of microfluid flow in the transverse direction depended on the precise fiber distribution in both longitudinal and transverse orientations. As indicated above, fibers were not perfectly aligned in the tow direction and significant convergent/divergent trajectories were found. These irregularities facilitated the fluid propagation in the transverse direction even in areas containing a high volume fraction of packed fibers.

4.3.2 Void transport

During tow impregnation, microvoids and macrovoids were found and their movement was followed from SXCT data. Microvoids were generated by small inhomogeneities in the flow

velocity in the tow cross section resulting in zones/channels were the fluid propagates faster. These differences in the velocity of the flow at the tow level were also shown in Figure 4.3. Elongated voids are formed as a result of the differences in the longitudinal flow within the tows. The migration of the void along the tow is sometimes constrained by presence of two fibers with convergent trajectories that can trap the void and arrest the propagation, Figure 4.3. These voids can escape from this trap in the longitudinal direction if the pressure gradient is large enough to push them along the constrained capillary channel. Otherwise, they will try to move along the transverse direction and the final transportation path depends on the different constraints, longitudinal and transverse, experience by the void towards the outlet gate.

Lundstrom [99] determined analytically the pressure gradient $\Delta p = (p1 - p2)$ required to move a void of radius R_v through a constricted capillary tube of radius R_{con}, Figure 4.5, as

$$\Delta p = \frac{2\gamma cos\theta}{R_{con}}(1 - \frac{R_{con}}{R_v}) \tag{4.5}$$

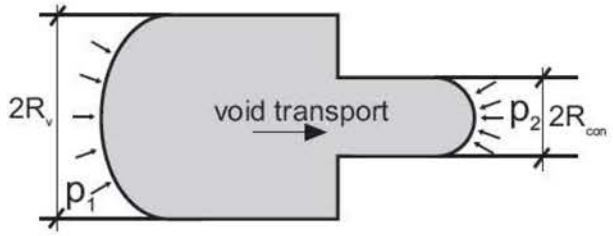

FIGURE 4.5: Constricted void transport through a capillary tube.

Assuming that the ratio R_v/R_{con} remains constant, 4.5 indicates that the smaller the capillary radius the higher the pressure gradient required to pull the void through the constriction. Thus, microvoids are much more prone to be trapped by the microstructure of the fiber bundle in the longitudinal direction and can only be evacuated by migration in the tow plane in which they will maintain some transverse mobility. As a consequence, small voids are rather difficult to evacuate in liquid molding for the usual pressure gradients applied but the influence of small voids in the mechanical behavior of composite materials is much

smaller than that of large voids, which can usually span dozens of fibers with a characteristic dimension in the range of the fiber tow thickness.

Bubbles resulting from minor air leaks at the inlet led to the formation of macrovoids, which were transported to the outlet gate during the *in situ* experiments. Initially, they were easily transported by the fluid flow, as compared with small voids, because the pressure differential to overcome the obstacles was much smaller. However, the bubble may be anchored along the trajectory because of various mechanisms (closed-packed fiber regions, fiber convergent trajectories, etc.) and the internal pressure has to rise to resume the propagation. As a result, the presence of the void led to an important perturbation of the fiber distribution as well as the vacuum bag. This is shown in Figure 4.6, which shows the cross sections of the fiber tow prior, during, and afer the transport of a large void. It is important to note that individual fibers did not return to the original position once the void passed through a given cross section and this effect can be probably attributed to the higher mobility of the fibers as a result of fluid lubrication. Very interestingly, the large void passed through the tow section, closing again the bag and leaving a trace of small voids that remained arrested after the process, delineating the original void contour, Figure 4.6 c).

4.4 Conclusions

In situ VARI experiments were carried out in the synchrotron beam to study the mechanisms of microfluid flow within a fiber tow by means of SXCT. A single tow of E glass fibers was infused with a water and syrup blend using an apparatus designed and built for this purpose. The tow was impregnated in several steps by controlling the fluid volume delivered at the inlet needle and radiographies at different angles were taken after each step to reconstruct the three dimensional microstructure of the infiltrated tow. The high resolution of the SXCT images allows the detailed reconstruction of individual fibers within the tow while the contrast between the different phases (air, fluid and fibers) was enough to track the fluid front position and shape as well as the void transport during infiltration. The ability of this

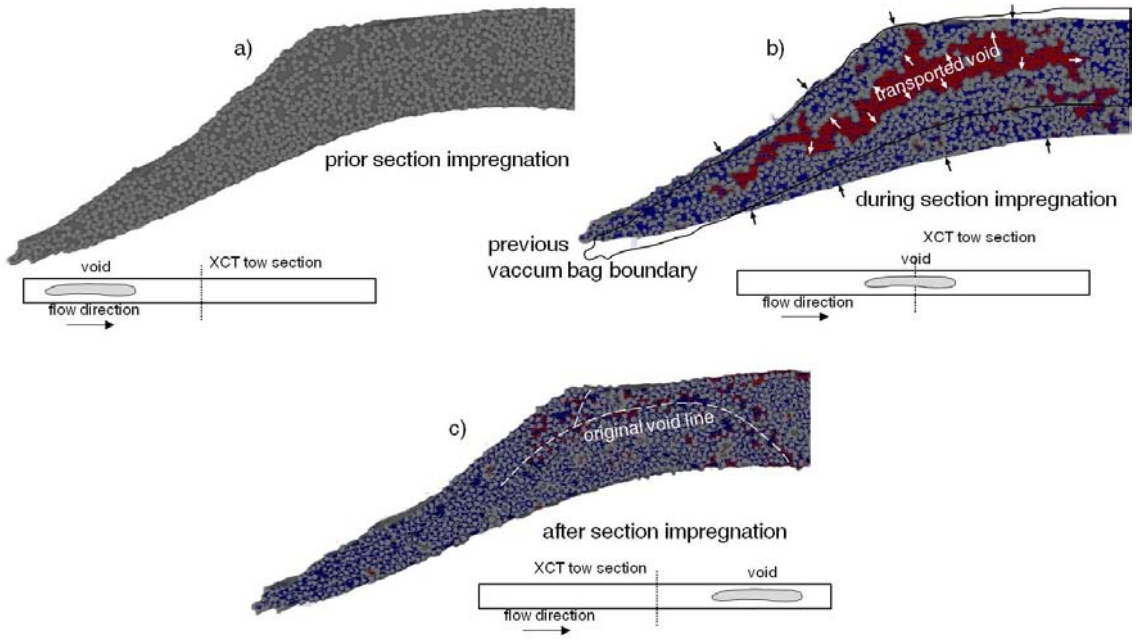

FIGURE 4.6: XCT cross section of the fiber tow showing the transportation during infiltration. a) Prior to infiltration. b) When the void is passing through the cross section. c) After impregnation. The fluid is shown in navy blue and the pore in red.

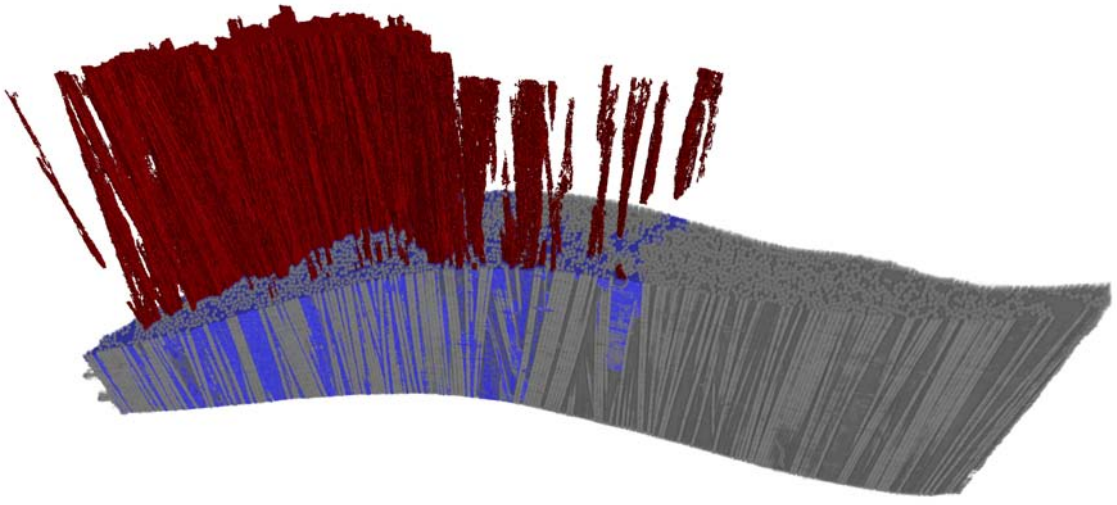

FIGURE 4.7: 3D cut of the reconstructed specimen during infiltration. The macroscopic pore, which is crossing through the tow, is shown in red while the fluid is presented in navy blue.

technique to analyze the details of microfluid flow and void transport in composite materials is clearly established.

The high resolution SXCT images showed an obtuse contact angles between the fluid and the fibers at the flow front. This behavior, which was opposed to the wetting contact angles measured in air, was also reported by other authors [94, 95] and it cannot attributed to dynamic effects because the tomograms were acquired when the flow front was stopped. More likely, it seems to be a surface effect triggered in vacuum by the interaction between the fluid and the fiber sizing. One consequence of the phenomenon is that the capillary pressure acted as a drag force on the fluid flow. As a result, fluid flow was favored through areas with low fiber volume fraction which presented higher permeability and lower capillary forces. The complexity of the microflow depended markedly on the microstructure and the presence of convergent/divergent individual fiber trajectories played a significant role. Convergent fiber trajectories tend to arrest the fluid propagation by capillary forces and the detailed reconstruction of the fiber distribution allowed the interpretation of the flow progression in terms of the capillary pressure and permeability factors.

The transport of small and large voids was also assessed by means of SXCT. Small voids were transported along the tow direction through the empty spaces between individual fibers. They were trapped when the distance between fibers was below a critical value because the pressure gradient required to overcome the capillary pressure was too high. As a result, a large volume fraction of very small voids was trapped in the microstructure. The propagation of a large void spanning dozens of fibers was also observed in the experiments. In this case, the void migrated easily along the fiber tow driven by the vacuum pressure gradient. Very interestingly, the internal pressure of the void was large enough to produce significant fiber and bag movements during the void transport, leaving a trail of smaller voids in the wake.

Chapter 5

Level set model of vacuum infusion

This chapter presents the model developed to simulate the vacuum infusion process by means of the level set method coupled to the standard Darcy's flow equation. The liquid/gas interface, known as fluid front, moves along during filling and divides the bag into dry and wet regions, whose boundary changes continuously during the process. These kind of problems, also referred as moving boundary or Stefan problems, are particularly complex to solve because the precise evolution of fluid front has to be determined as part of the solution. In this thesis, the fluid front position is tracked as the zero level curve of a general level surface that evolves with time, following the strategy of the level set method. This methodology was originally developed by J. A. Sethian [100, 101] and has been successfully applied to solve combustion, phase change, fluid and solid mechanics problems, etc. due to its easy integration and compatibility with traditional finite element algorithms.

5.1 A level set formulation for 2D flow propagation

The model is based on the resolution of the Darcy's equations for the fluid flow through a porous media. Darcy's equation establishes a linear relationship between the average fluid velocity through the fiber preform, $\mathbf{v}$, and the externally imposed pressure gradient, ∇p. The

proportionality factor is related with the fabric permeability tensor $\mathbf{K}$ and the fluid viscosity μ according to,

$$\mathbf{v} = -\frac{\mathbf{K}}{\mu}\nabla p \tag{5.1}$$

Darcy's equation is strictly valid for laminar flow propagation through porous medium under low Reynolds number and this regime is usually attained during resin impregnation in liquid moulding. In addition, this equation should be adapted in those cases where fabric deformability plays an important role, such as vacuum infusion. Invoking the mass conservation law, the Darcy's modified equation is given by

$$\rho\nabla\cdot\mathbf{v} + \frac{\partial\rho}{\partial t} = 0 \tag{5.2}$$

where ρ is the current density of the infused material within the volume considered. Assuming that the compaction takes place in the through-the-thickness direction of the fabric (normal compaction), the conservation law can be expressed in terms of the change in the fiber volume fraction as [19, 25, 102],

$$\nabla\cdot\mathbf{v} = \frac{1}{V_f}\frac{\partial V_f}{\partial t} \tag{5.3}$$

The partial differential equation for the pressure field evolution $p(\mathbf{x}, t)$ can be obtained from equations (5.1) and (5.2) as

$$\nabla(\frac{\mathbf{K}}{\mu}\cdot\nabla p) = -\frac{1}{V_f}\frac{\partial V_f}{\partial t} \tag{5.4}$$

In addition, the stress partition between the fiber bed, σ_{fiber}, and the infusion fluid, p, is established by means of Terzaghi's effective stress theory according to

$$\sigma_{fiber} = p_{atm} - p \tag{5.5}$$

where p_{atm} is the atmospheric pressure in the case of vacuum infusion. The fiber volume fraction, V_f, is also pressure dependent so the final thickness of the composite will depend on the pressure transferred from the resin to the fiber preform and, therefore, $V_f = V_f(p_{atm} - p)$ (see experimental results in Chapter 3). Similarly, the permeability tensor, $\mathbf{K}$, is a function of the fiber volume fraction, leading to a non-linear partial differential equation for the pressure field given by

$$\nabla(\frac{\mathbf{K}(V_f)}{\mu} \cdot \nabla p) = -\frac{\partial V_f/\partial p}{V_f}\frac{\partial p}{\partial t} \tag{5.6}$$

where the physical parameters in this equation (namely, the in-plane permeability of the fabric, $\mathbf{K}(V_f)$, the fiber bed compressibility, $V_f(\sigma_{fiber})$, and the fluid viscosity, μ) were measured in Chapter 3 for the system under consideration. Equation (5.6) has to be solved under the appropriate boundary (prescribed pressure or fluid velocity) and initial conditions. However, this equation is only valid when the fluid completely fills the solution domain which is not the case of the infusion problem as the fluid front propagates through the dry preform. As a result, a numerical strategy has to be developed to deal with this new scenario.

5.1.1 The level set method

In the level set method, the fluid front position is defined with the aid of an auxiliary function $\phi(\mathbf{x}, \mathrm{t})$, which stands for the distance of the point $\mathbf{x}$ to the flow front at a given time t [100, 101]. Thus, the flow front is identified by $\phi(\mathbf{x}, \mathrm{t}) = 0$ and the position of the fluid front is given at any time by the zero level of the evolving function ϕ during infusion. For the sake of clarity, the zero level set curves, in the $x - y$ space, for two different times, initial and t=t_1 are depicted in Figures 5.1 a) and b), respectively. They can be viewed as evolving $x - y$ curves in planes normal to the time axis.

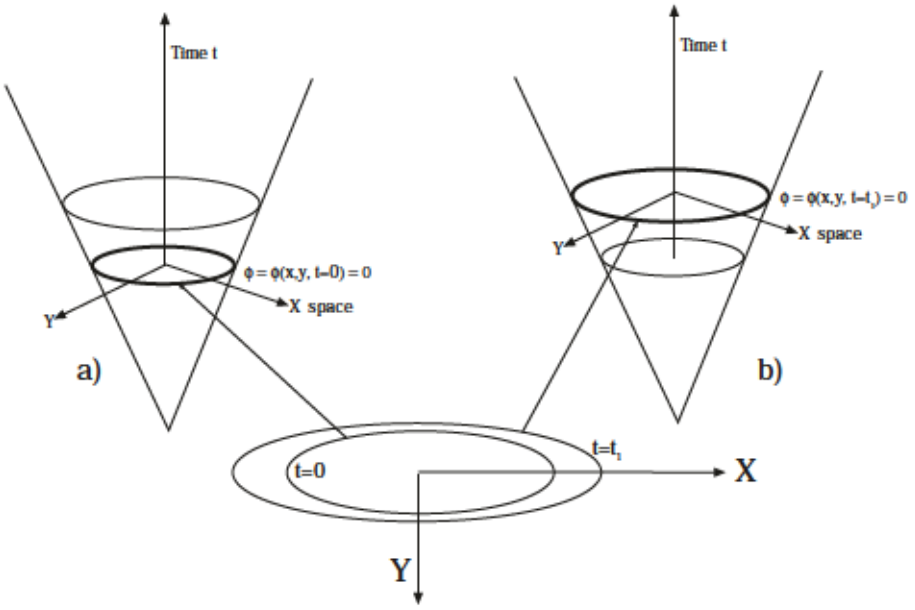

FIGURE 5.1: Transformation of the front flow motion into the level set method [100, 101]. a) Initial flow front position $\phi(\mathbf{x}, t) = 0$, b) Flow front position at time $t=t_1$ $\phi(\mathbf{x}, t_1) = 0$.

Differentiating $\phi(\mathbf{x}, t)$ using the chain rule, the evolution equation for the level set function ϕ is given by

$$\frac{\partial \phi}{\partial t} + \frac{\partial \phi}{\partial \mathbf{x}} \frac{\partial \mathbf{x}}{\partial t} = \frac{\partial \phi}{\partial t} + \nabla \phi \cdot \mathbf{v} = \frac{\partial \phi}{\partial t} + F|\nabla \phi| = 0 \tag{5.7}$$

where the relation $\vec{n} = \nabla\phi/|\nabla\phi|$ between the normal to the level set surface and the gradient is used. $F = \mathbf{v} \cdot \mathbf{n}$ is the velocity normal to the fluid front, Figure 5.2 a) and $|\nabla\phi|$ is the norm of the gradient of the level set function which is equal to 1 when the distance function to the front flow is used. The integration of the differential equation (5.7) provides the evolution of the level set function and thus the position of the flow front given by $\phi(\mathbf{x}, t) = 0$.

In general, the propagation velocity F may depend on local variables such as the curvature, normal vector, etc. However, it can be useful to make F dependent on global variables as the shape, position, or underlaying flow velocity depending on the physical problem to be solved (diffusion, fluid mechanics, etc). In our problem, the flow front moves according

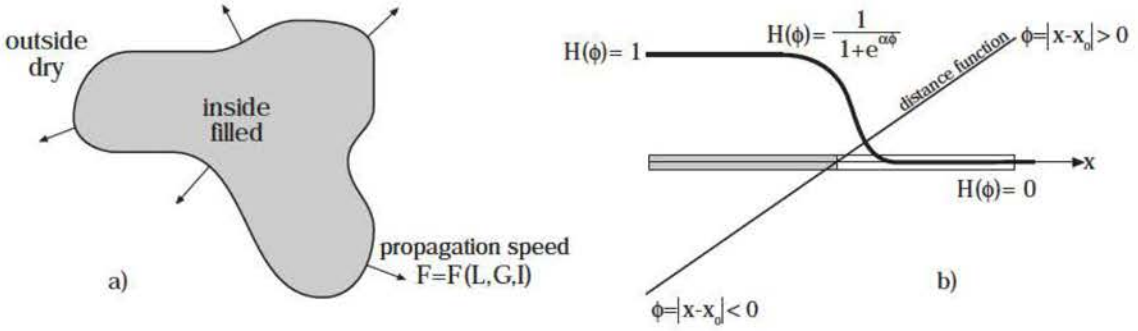

FIGURE 5.2: Propagation of the front flow [100, 101].

to the Darcy's velocity (proportional to the derivative of the pressure field) at the flow front position. The velocity is determined from equation (5.1) using the Carman-Kozeny expression (3.4) for the permeability factor.

Thus, equation (5.6) can be modified using the level set function to indicate whether or not the region is filled by the fluid according to

$$H(\phi)\nabla(\frac{\mathbf{K}(p)}{\mu}\nabla p) = -\frac{\partial V_f/\partial p}{V_f}\frac{\partial p}{\partial t} \tag{5.8}$$

where $H(\phi)$ is an approximation of the Heaviside like function whose value is equal to 1 in the regions filled with fluid ($\phi < 0$) and zero in the dry regions ($\phi > 0$), Figure 5.2 b). Thus, according to equation 5.5, $p = p_{vac}$ in the dry region. $H(\phi)$ has to be smoothed out in a narrow transition zone around the fluid front in order to avoid numerical problems during the integration of the partial differential equation. In this case,

$$H(\phi) = \frac{1}{1 + e^{\alpha\phi}} \tag{5.9}$$

where α ($>> 1$) is a numerical parameter that controls the width of the transition region.

5.1.2 Numerical strategy and discretization

Equations (5.8) and (5.7) should be solved simultaneously within a 2D domain with the appropriate initial and boundary conditions. In this thesis, the equations are solved in a rectangular domain for both infusion problems described in the previous chapters corresponding to the fluid flow through fiber preforms with and without a mesh distribution medium. Therefore, the discrete pressure field evolution and the fluid front position can be obtained using the finite differences method on a rectangular grid. The extension of the model to arbitrary geometries requires its implementation within the framework of the finite element which is considered out of the scope of this thesis.

A rectangular spatial domain of LxB is discretized using a uniform grid (i, j) with equally spaced increments Δx, Δy. The first and second order spatial derivatives at a given point from Darcy's equation (5.8) are approximated with the $O(h^2)$ central differences scheme as $df/dx(x_0,t) \approx (f(x_0+h,t)-f(x_0-h,t))/2h$ and $d^2f/dx^2(x_0,t) \approx (f(x_0+h,t)-2f(x_0,t)+f(x_0-h,t))/h^2$, where h is the grid spacing. The time derivatives of the same equations are discretized with a standard forward Euler method using Δt as the time increment using $df/dt(x_0,t) = (f(x_0,t+\Delta t)-f(x_0,t))/\Delta t$ with the same truncation error $O(\Delta t^2)$.

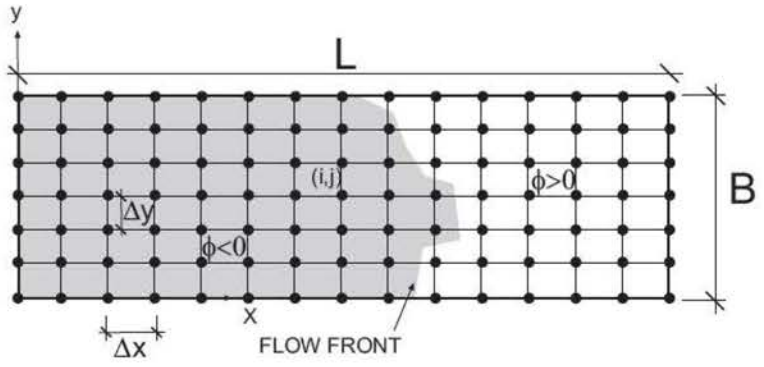

FIGURE 5.3: Domain discretization in a rectangular grid.

The level set differential equation (5.7) is hyperbolic and it should be solved by the application of specific numerical algorithms for the spatial discretization. In this thesis, a combination of the forward Euler integrator for the time discretization and the upwind spatial

algorithm for the spatial discretization is adopted [100, 101]. Other higher-order integrators such as Runge-Kutta and multistep methods can lead to lower local truncation errors so the time step could be increased and the efficiency improved. Within this context, the level set equation differential equation (5.7) can be integrated using the following scheme

$$\phi_{i,j}^{n+1} = \phi_{i,j}^{n} - \Delta t[\max(F_{i,j}, 0)\nabla^{+} + \min(F_{i,j}, 0)\nabla^{-}] \tag{5.10}$$

where $\phi_{i,j}^{n}$ is the current level set value at the local position i, j and time t, $\phi_{i,j}^{n+1}$ the prediction for the incremented time $t+\Delta t$ and $F_{i,j}$ stands for the flow front velocity at the local position i, j and time t. The upwind operators read as follows

$$\nabla^{+} = [\max(D_{i,j}^{-x}, 0)^2 + \min(D_{i,j}^{x}, 0)^2 + \max(D_{i,j}^{-y}, 0)^2 + \min(D_{i,j}^{y}, 0)^2]^{1/2} \tag{5.11}$$

$$\nabla^{-} = [\max(D_{i,j}^{x}, 0)^2 + \min(D_{i,j}^{-x}, 0)^2 + \max(D_{i,j}^{y}, 0)^2 + \min(D_{i,j}^{-y}, 0)^2]^{1/2} \tag{5.12}$$

where $D_{i,j}^{x} = (\phi_{i+1,j}^{n} - \phi_{i,j}^{n})/\Delta x$ and $D_{i,j}^{-x} = (\phi_{i,j}^{n} - \phi_{i-1,j}^{n})/\Delta x$ stand for the forward and backward first order operators, respectively, for the x-direction spatial derivatives (the same definitions correspond to the y-direction). This upwind integrator scheme allows to recover the overall information of the flow front variations and propagation directions. For instance, $D_{i,j}^{x}$ use the information of the level set variation from i to $i+1$ grid points and the solution, therefore, propagates from the right to the left, while $D_{i,j}^{-x}$ is just the opposite.

The pressure and level set functions are updated according to the forward Euler integrator and, therefore, a stable time increment Δt satisfying the Courant-Friedreichs-Lewy stability condition should be given. In this case, the maximum propagation of the flow front in a given time increment Δt should not exceed the grid dimensions according to

$$\max(F\Delta t) \leq \Delta x, \Delta y. \tag{5.13}$$

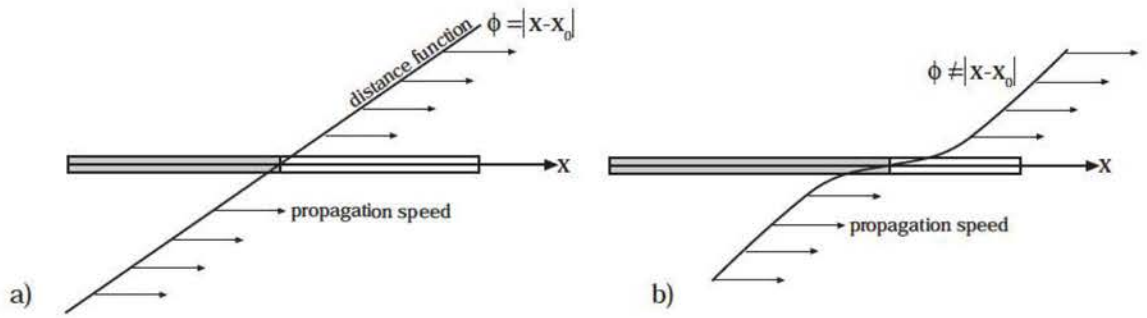

FIGURE 5.4: a) Initial level set function that gives the distance to the flow front position, b) Degradation of the level set function after flow propagation.

From a practical viewpoint, a time increment is assumed *a priori* on the basis of previous experience.

It should be noted that nothing guarantees that the updated level set function $\phi_{i,j}^{n+1}$, equation (5.10), provides the actual distance of each point to the flow front and this can generate convergence problems after a few time increments, Figure 5.4 b). To avoid this problem, several reinitialization schemes for the level set function after each time increment were proposed in the literature [103, 104] based on resolution of the following standard differential equation. For instance,

$$\frac{\partial \phi}{\partial \tau} = S(\phi_0)\left(1 - \sqrt{(\frac{\partial \phi}{\partial x})^2 + (\frac{\partial \phi}{\partial y})^2}\right) \tag{5.14}$$

$$\phi(\mathbf{x}, \tau = 0) = \phi_0(\mathbf{x}) \tag{5.15}$$

where S is the sign function that is usually smoothed-out to $S(\phi_0) = \phi_0/\sqrt{\phi_0^2 + \epsilon^2}$ due to numerical reasons, being ϵ a small positive number and τ a fictitious time. When using this strategy, the updated level set function will provide the distance of each point to the flow front given by $\phi_0(\mathbf{x})$.

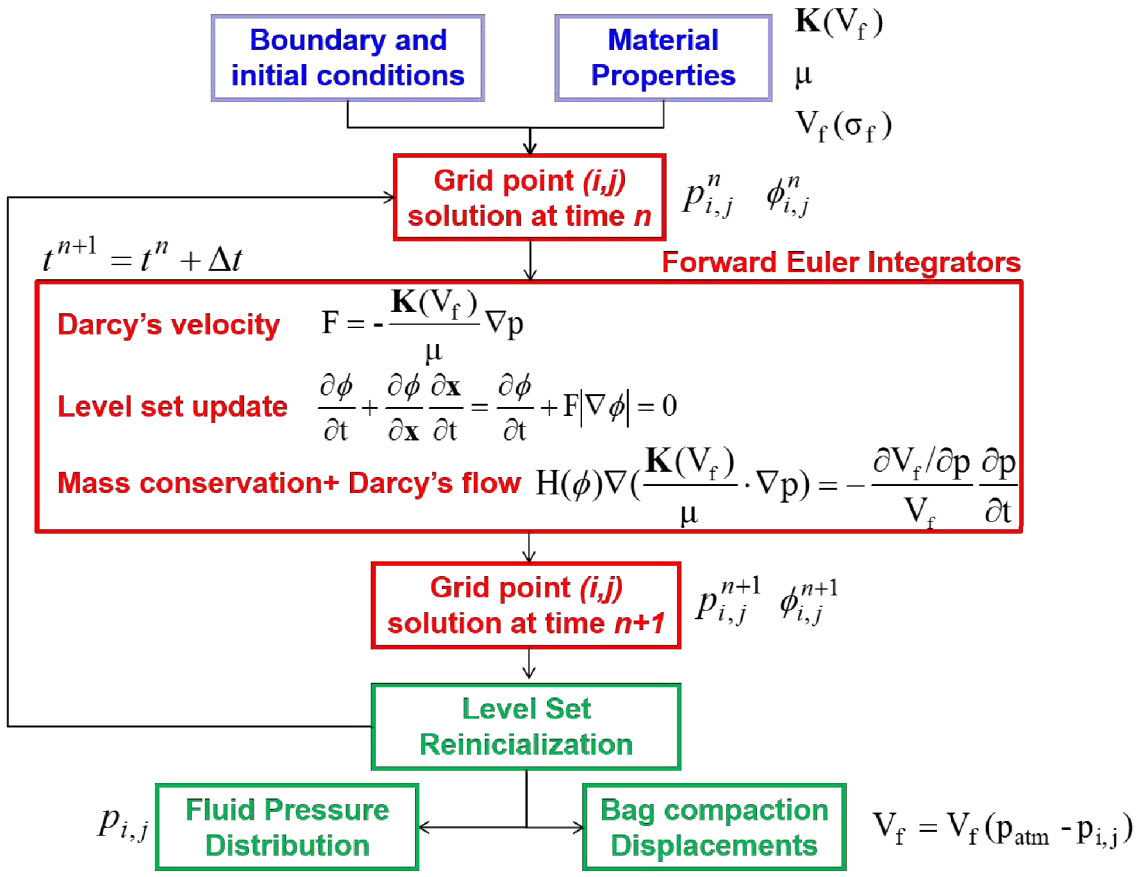

FIGURE 5.5: Modeling flowchart of the level set approach for vacuum infusion.

The numerical strategy previously detailed was programed in the MATLAB R2010a environment. The basic scheme of the approach is summarized the flow chart depiected in Figure 5.5. The inputs of the model are the material properties (fabric permeability $\mathbf{K}(V_f)$, fluid viscosity μ and fiber bed compaction law $V_f = V_f(p_{atm} - p)$) and the boundary and initial conditions for the pressure and level set discrete field. The forward Euler scheme gives the predictions at time t^{n+1} of the fluid pressure and of the level set function, $p_{i,j}^{n+1}$ and $\phi_{i,j}^{n+1}$, respectively, at the discrete grid points i, j of the domain from the solutions in the previous time step $p_{i,j}^n$ and $\phi_{i,j}^n$. Pressure and level set function at the grid points were recorded to compare with the experimental results. The fluid pressure was used to compute the final volume fraction of the fabric V_f and, hence, the vacuum bag displacements Δh.

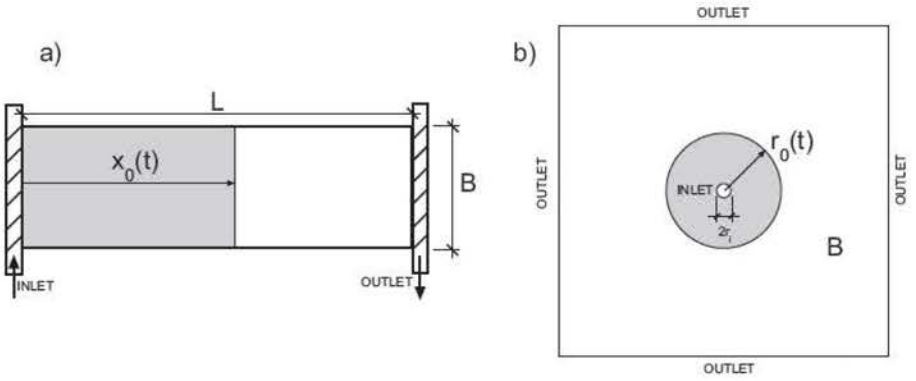

FIGURE 5.6: Validation case studies: a) one dimensional flow. b) Radial flow.

5.2 Model validation: one dimensional and radial flow

The validity and the effectiveness of the level set strategy to simulate infusion was demonstrated by comparison with two cases for which an analytic solution is available: one dimensional flow and radial flow, Figure 5.6. In both cases, the fiber preform is assumed to behave as an incompressible solid and, therefore, the permeability factor is independent of the fluid pressure, so an exact analytical solution can be obtained. The isotropic permeability factor was $K = 4.28\ 10^{-11}$ m^2, corresponding to 60% fiber volume fraction for configuration stack $[0°]_8$, and the fluid viscosity $\mu = 2.35$ Pa· s.

5.2.1 One dimensional flow

The simulation of the one dimensional flow was carried out using a rectangular domain of $L = 250$ mm and $B = 80$ mm in the $x - y$ plane, Figure 5.6 a), discretized with an uniform grid with $\Delta x = 3.125$ mm and $\Delta y = 2$ mm. Inlet ($x = 0$) and outlet ($x = L$) pressure were set, respectively to the atmospheric, p_0, and vacuum pressure. Slip free conditions at the running edges were applied to constraint the flow parallel to the x axis. Time integration was carried out using $\Delta t = 0.01$ s as the stable time increment.

The exact analytical solution of this problem can be obtained from the integration of Darcy's equation as follows. Taking into account that the flow was one dimensional and that the fabric was incompressible, equation 5.4 yields

$$\frac{\partial}{\partial x}(\frac{K}{\mu}\frac{\partial p(x)}{\partial x}) = 0 \Rightarrow \frac{d^2p}{dx^2} = 0 \Rightarrow p(x) = p_0(1 - \frac{x}{x_0}) \tag{5.16}$$

In this case, the Darcy's velocity at the flow front position at $x = x_0$ is also the time derivative dx_0/dt that can be integrated according to

$$v_x = -\frac{K}{\mu}\frac{dp}{dx} = \frac{Kp_0}{\mu x_0} = \frac{dx_0}{dt} \Rightarrow \frac{\mu}{Kp_0}\int_0^{x0(t)} x_0\, dx_0 = \int_0^t dt \Rightarrow t(x_0) = \frac{\mu}{2Kp_0}x_0^2 \tag{5.17}$$

The flow front position x_0 as a function of time in equation 5.17 is compared with the simulation results obtained with the level set method in Figure 5.7 a). The agreement between both was excellent. The pressure profiles were also included in Figure 5.7 b) for the sake of completion. They show a linear shape in agreement with the predictions of equation 5.16

5.2.2 Radial flow

Radial flow was simulated by means of an square domain of $L = 250$ mm in the $x - y$ plane, Figure 5.6 b), discretized using an uniform grid with $\Delta x = 3.125$ mm. Vacuum pressure was prescribed in all the edges of the square domain while atmospheric pressure was imposed to the grid node at the center of the domain. Although the solution domain does not present cylindrical symmetry, the solution obtained verifies such condition because the level set methodology leads to the radial transport of the vacuum pressure from the prescribed boundaries to the flow front position. Obviously, the axial symmetry condition is lost once the flow front reach the boundaries, and the comparison with the analytical

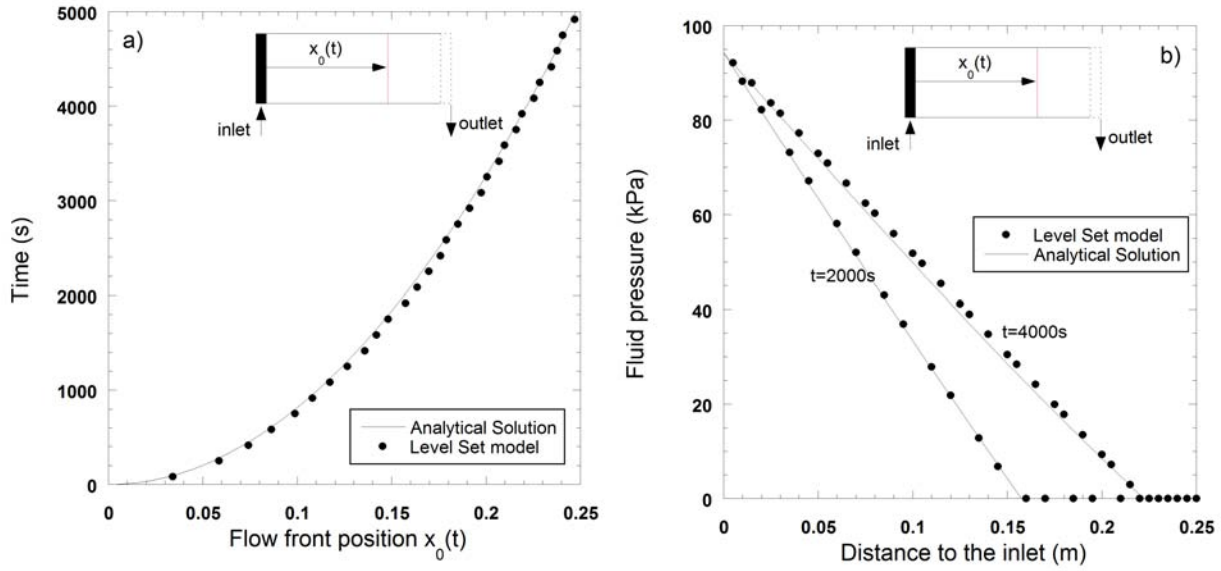

FIGURE 5.7: Analytical and level set model solution for one dimensional incompressible flow: a) evolution of the flow front with time. b) Fluid pressure profiles for $t = 2000$ s and $t = 4000$ s.

solution is no longer possible. Time integration was carried out using $\Delta t = 0.01s$ as the stable time increment.

The simulation results were compared with the exact analytical solution obtained from the integration of the Darcy's equation in cylindrical coordinates. The velocity field will be radial $v(r)$ and the continuity equation for the incompressible flow in cylindrical coordinates reads as

$$v(r) = -r\frac{dv}{dr} \tag{5.18}$$

and Darcy's equation relating the fluid flow radial velocity with the gradient in the same direction is expressed as

$$v(r) = -\frac{K}{\mu}\frac{dp}{dr} \tag{5.19}$$

By combining both incompressibility and Darcy's equation, a second order differential equation is obtained for the radial pressure field which admits a logarithmic solution of the form

$$-r\frac{d^2p}{dr^2} = \frac{dp}{dr} \Rightarrow p(r) = A + B\log r \Rightarrow p(r) = p_0\frac{\ln\frac{r}{r_0}}{\ln\frac{r_i}{r_0}} \tag{5.20}$$

where the coefficients A and B were determined from the boundary conditions. To avoid singularities at injection point ($r = 0$), the inlet pressure is imposed in a circle of radius r_i, while the vacuum pressure is prescribed at the flow front position r_0. Then, the flow front velocity, dr_0/dt, is obtained from the Darcy's velocity at $r = r_0$ as

$$v(r) = -\frac{K}{\mu}\frac{dp}{dr} \Rightarrow v(r = r_0) = \frac{Kp_0}{\mu}\frac{1}{r_0\ln\frac{r_0}{r_i}} = \frac{dr_0}{dt} \tag{5.21}$$

which can be integrated by splitting x_0 and t variables as

$$\frac{\mu}{Kp_0}\int_0^{r_0(t)} r_0\ln\frac{r_0}{r_i}\,dr_0 = \int_0^t dt \Rightarrow t(r_0) = \frac{\mu}{2Kp_0}\left[r_0^2\ln\frac{r_0}{r_i} - \frac{1}{2}(r_0^2 - r_i^2)\right] \tag{5.22}$$

The analytical flow front position r_0 given by equation 5.22 is compared with the simulation results obtained with the level set method in Figure 5.8 a). The agreement between analytical and level set solution was again excellent. Likewise in the previous case study, the pressure profiles were plotted in Figure 5.8 b) showing the logarithmic dependence indicated by equation 5.20. It should be mentioned that the injection radius used in the analytical solution is computed with the 2x2 grid points influence area as $r_i = 2\cdot\Delta x/\sqrt{\pi}$.

Both case studies showed very good agreement of the numerical results with the analytical solutions and demonstrate the ability of the level set strategy to track the flow front evolution during the propagation of viscous fluids through porous medium. Therefore, the model can be applied to analyze the fluid flow during the infusion experiments presented in Chapter 3. These cases correspond with the flow propagation through a porous compressible medium

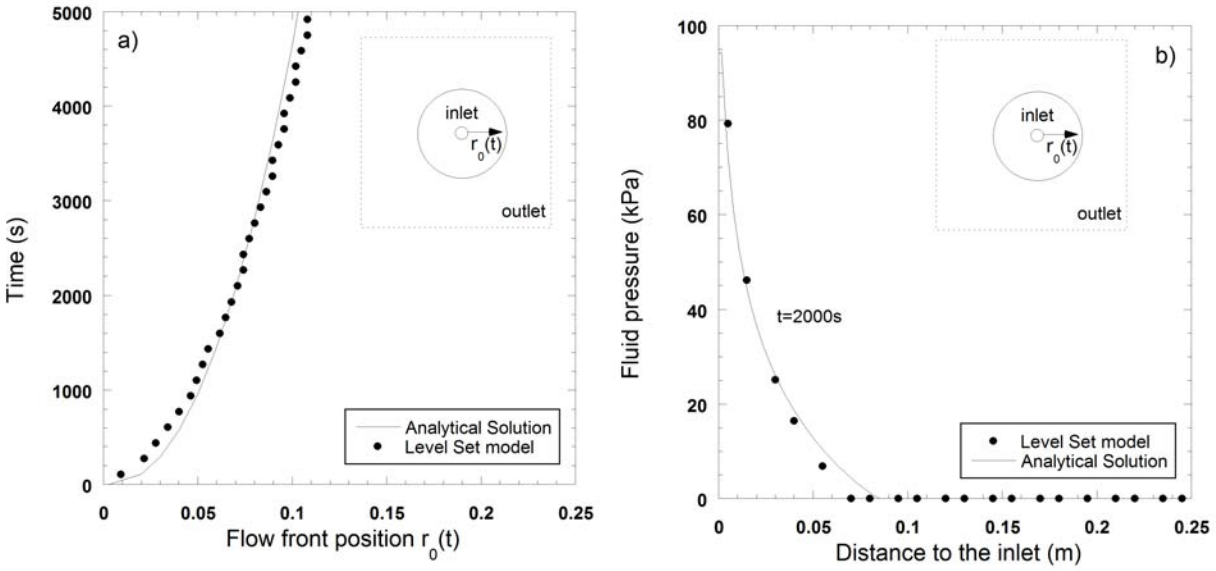

FIGURE 5.8: Analytical and level set solution for radial incompressible flow: a) Evolution of the flow front with time. b) Fluid pressure profiles at $t = 2000$s and $t = 4000$s.

where the permeability changes due to the stress transfer between the fluid and the fiber preform.

5.3 Simulation of vacuum infusion experiments

This section is devoted to model the infusion experiments in Chapter 3 by means of the level set model previously described. Two set of infusion experiments, with and without distribution medium, were carried out on rectangular strips of an E-glass fabric lay-up using corn syrup blends as the infusion fluid. The experimental set-up was the same in both cases although the fluid flow was essentially unidimensional and in the plane of the laminate in the experiments without distribution medium. On the contrary, the flow was a combination of in-plane flow through the laminate lay-up and out-of-plane or through-the-thickness flow when using the distribution net on the top of the laminate. The simulation scheme used for both infusion cases is sketched in Figure 5.9. The first case, Figure 5.9 a), represents the in-plane infusion without distribution medium. The flow is essentially unidimensional

along the x direction and corresponds with the mid plane of the laminate. The second case, Figure 5.9 b) represents to the mixed flow in a representative through-the-thickness section $x - z$ when the distribution medium is placed on top of the laminate.

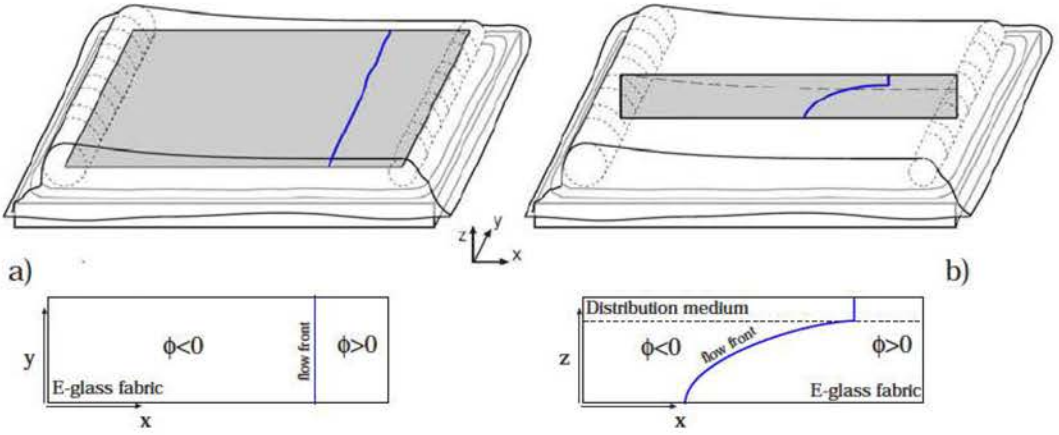

FIGURE 5.9: Simulation of the infusion test experiments: a) Without distribution medium, b) With distribution medium.

5.3.1 Infusion experiments without distribution medium

The rectangular fabric strip of L =250 mm and B =80 mm was discretized with an uniform grid with $\Delta x = 3.125$ mm and $\Delta y = 2$ mm to capture the evolution of the flow front during the experiments. The model parameters (fabric permeability, fluid viscosity and fiber bed compaction law) were determined from independent experiments and were summarized in Chapter 3 for the different laminate configurations $[0°]_8$, $[0°]_4$ and $[0°]_2$. The simulation was carried out in two stages. Firstly, the dry fabric was impregnated by applying vacuum at the venting port while fluid was infused from the inlet port. After the fabric was fully impregnated at time T_f, the inlet port was closed and the vacuum pressure maintained the until bag displacements were fully stabilized. This last stage is also known as the post filling stage.

Initial and boundary conditions are imposed over the discretized domain for both pressure and level set fields, Figure 5.9 a). Vacuum pressure is prescribed in the grid points belonging to the venting port at $x = L$

$$p(x = L, y, t) = 0 \tag{5.23}$$

while the pressure of the inlet is increased using a smooth exponential function rising from the initial vacuum to the reference atmospheric pressure p_0 according to

$$p(x = 0, y, t) = p_0(1 - e^{-A_f t}) \tag{5.24}$$

The parameter A_f controls the pressure build up speed and was adjusted from the experimental results. In addition, fluid flow at $y = 0$ and $y = B$ has to be parallel to the longitudinal edges. Thus the slip free condition (zero Darcy's velocity normal to the boundaries, $\mathbf{v}\cdot\mathbf{n} = 0$) at both fabric edges at $y = 0$ and $y = B$ was also prescribed to simulate one dimensional flow with no fluid race-tracking in the x fabric strip direction. Therefore, the pressure derivatives along $y = 0$ and $y = B$ edges are constrained according to

$$\frac{\partial p}{\partial y}(x, y = 0, t) = \frac{\partial p}{\partial y}(x, y = B, t) = 0 \tag{5.25}$$

Once the fluid reaches the venting port at $x = L$, the post filling stage starts by modifying the pressure at the inlet port. In this case, the inlet port is closed and the resin velocity, proportional to the x derivative of the pressure, at the entrance gate progressively decays to zero using the exponential function $\partial p(x = 0, y, t)/\partial x = v_0 e^{-A_p(t-T_f)}$ where A_p is a numerical parameter that controls the inlet gate closing speed and was adjusted from the experimental results, and v_0 was the inlet fluid velocity when the filling stage finishes at $t = T_f$.

The level set function was also initialized with the distance to the flow front. Hence, as the initial position of the flow front was the inlet edge at $x = 0$, the corresponding value

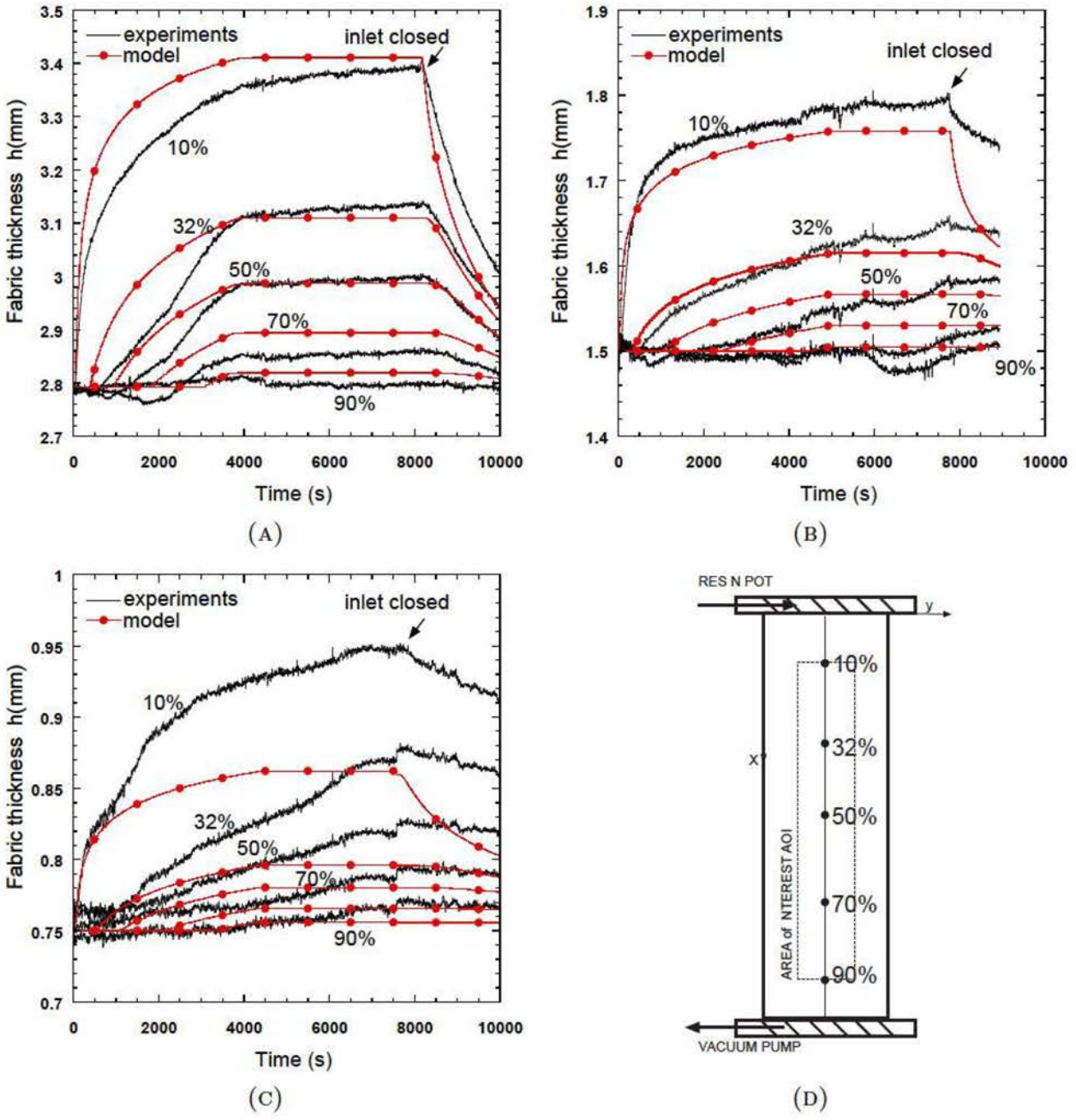

FIGURE 5.10: Evolution of the vacuum bag thickness with time at different locations along the infusion length (10%, 32%, 50%, 70% and 90%) A) $[0°]_8$ B) $[0°]_4$ C) $[0°]_2$ D) Sketch of the panel with the different positions.

of the level set function was $\phi(x, y, t = 0) = |x|$. Similar zero derivative conditions were applied to the level set function along the running edges ($y = 0$ and $y = B$) to prevent race-tracking and to constraint the unidimensional fluid propagation along the x direction

of the fabric strip. It should be remarked that the time evolution of the level set function is $\phi(x, y, t) = |x(t) - x_0|$ where x_0 is the flow front position at time t.

This set of boundary conditions leads to the propagation of the flow front along the x direction according to the experimental results. The integration of the differential equations was carried out using the finite differences algorithm in the previous section using a time increment of $\Delta t = 0.01s$ to fulfill the stability condition, 5.13, during the whole analysis. The fluid pressure values at the grid point were obtained and the stress carried by the fibers was computed from Terzaghi's effective stress theory (5.5) which allows the determination of the thickness change and fiber volume fraction from the fiber bed compaction curve determined from experiments carried out under wet conditions (3.6).

The experimental results of the evolution of the fabric thickness with time at various distances from the inlet port (10, 32, 50, 70 and 90% of the infused length) are compared with the corresponding simulation results in Figure 5.10. The model captured reasonably well the changes in fabric thickness with time at the different locations during the filling and post-filling stages specially in the two thicker laminates $[0°]_8$ and $[0°]_4$, Figure 5.10 A) and B). After the flow front reaches an specific position, the fluid pressure builds up and the atmospheric pressure is shared with the fiber bed resulting in the corresponding thickness increase also known as spring-back. Of course, the model was not able to capture the initial thickness reduction when the flow front reached a location because of the lubrication effect (responsible for this behavior) was not accounted for in the simulations.

The experimental results of the time evolution of the fluid pressure at the locations of the three pressure sensors along the infusion length are compared with the simulation in Figure 5.11. The agreement between them was very good for the three cases analyzed in terms of maximum fluid pressure attained at the given points although the specific temporal evolution and the time to reach the maximum showed some minor discrepancies. Small ripples and other irregularities found in the experimental curves were likely due to void transport and/or inhomogeneous local fiber distribution.

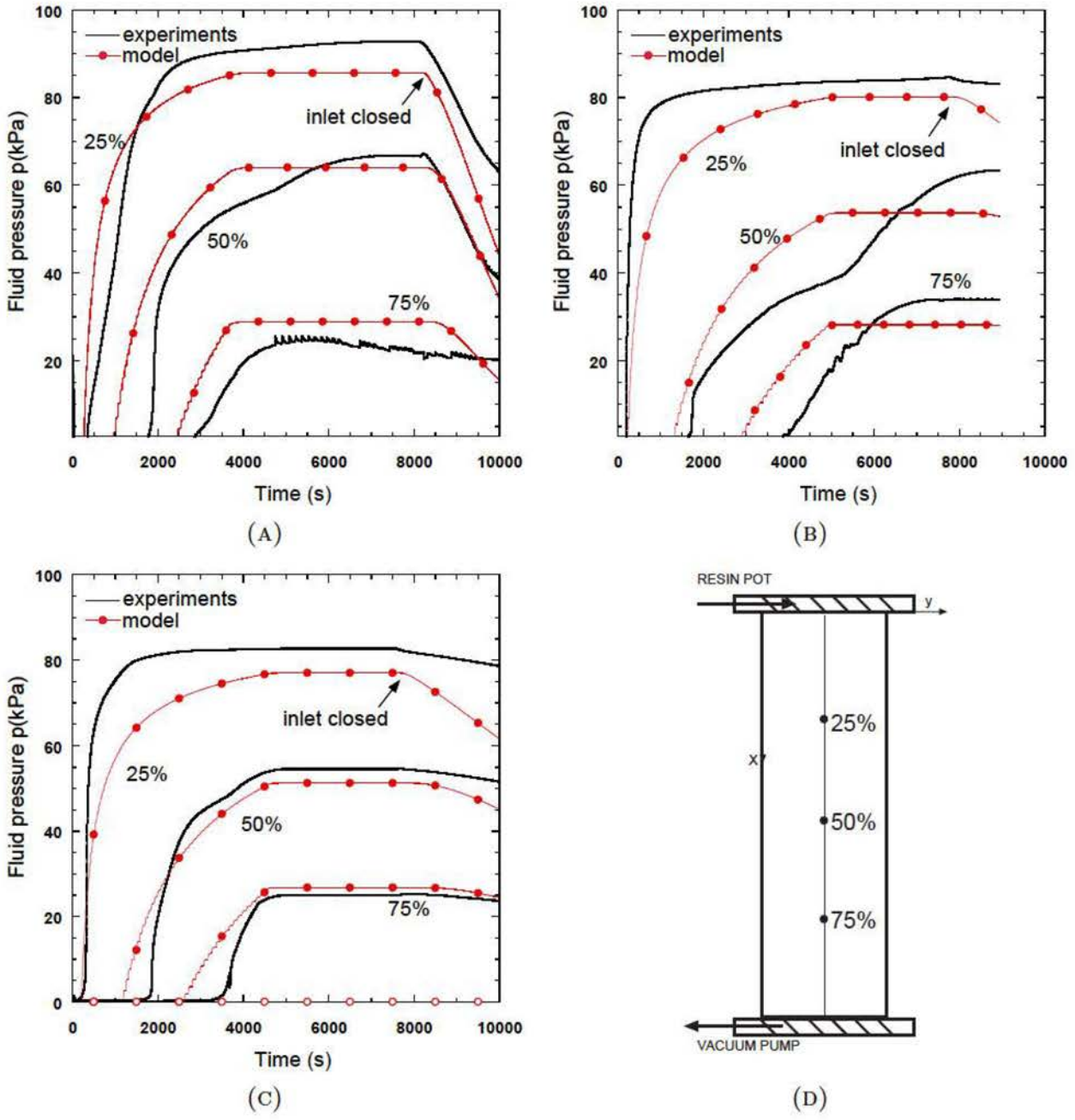

FIGURE 5.11: Evolution of fluid pressure at different positions of the strip located at 25%, 50% and 75% along the infusion line. A) $[0°]_8$ B) $[0°]_4$ C) $[0°]_2$ D) Sketch of the panel with the different positions of the pressure transducers.

It should be pointed out the lack of accuracy of the model predictions of the bag displacements for the thinnest laminate configuration ($[0°]_2$ laminate in Figure 5.10 C)). In this case, the bag displacements are underestimated and this result can be probably due to the

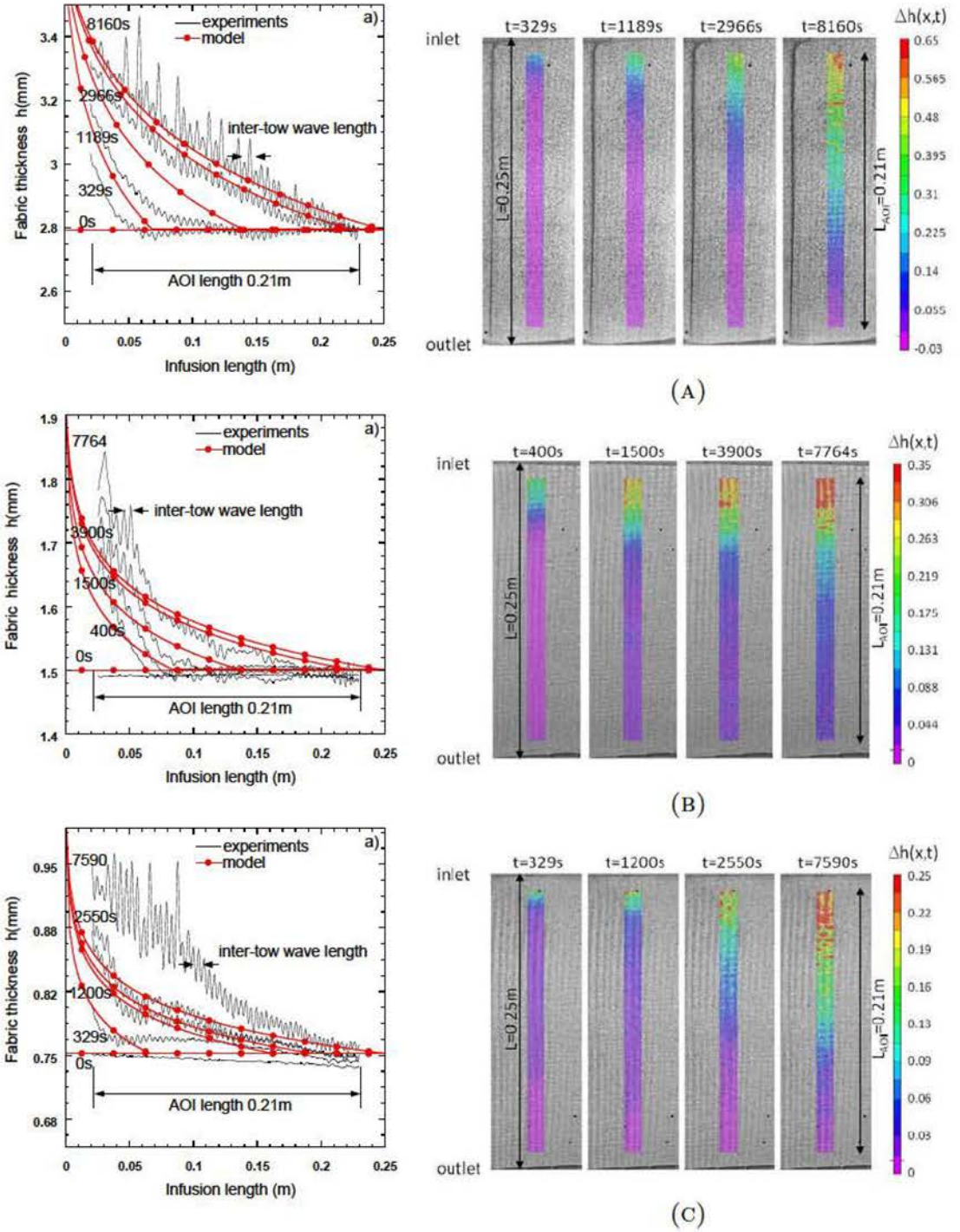

FIGURE 5.12: a) Evolution of the bag thickness profile along the infusion length within the AOI for different infusion times. b) Contour plot of the increment in the fabric thickness, $\Delta h(x,t)$, within the AOI for different infusion times. A) $[0°]_8$ B) $[0°]_4$ C) $[0°]_2$.

limitations of the wet fiber bed compaction test for very thin laminates. As it was shown above, the model was able to reproduce, within the experimental scatter, the fluid pressure distribution along the infusion length independently of the number of layers, Figure 5.11. Consequently, the model was able to capture accurately the stress transfer between the fluid and the infused fabric but failed to determine the compaction displacements for the thinnest laminate configuration. In addition, the experimental scatter in the fiber bed compaction tests could contribute to this effect, specially for the thinnest laminate configuration.

The experimental pressure build up recorded by the sensors presented a time lag with respect to the numerical predictions obtained with the level set method, Figure 5.11. As it was already mentioned in the experimental techniques (Chapter 2), sensors were inserted in a drill machined into the PMMA tool. The cavity of the sensor was bridged during the tests by the woven fabric so the sensor was able to measure the fluid pressure rather than the mechanical force transmitted by the fabric. This small cavity between the fabric and the sensor surface should be filled by the fluid during the infusion and can produce the aforementioned delay observed.

The shape of the vacuum bag at different instants during during the filling stage is shown in Figure 5.12 a). The contour plot of the increment in the fabric thickness, $\Delta h(x,t)$, obtained by digital image correlation is also plotted in Figure 5.12 b) for the same infusion times. As in the previous cases, the agreement is reasonable for the thicker laminate configurations $[0°]_8$ and $[0°]_4$ but this is not the case for the thinnest laminate $[0°]_2$ configuration. However, the general shape of the vacuum bag profile (which essentially describes the stress sharing between the fiber bed and the infusion fluid in these experiments) was well captured in all cases.

An important manufacturing parameter in vacuum infusion manufacturing is the filling time that should be compared with the gel time of the resin to prevent the formation of dry spots. The comparison between the experimental and numerical results of filling the time is presented in Figure 5.13. The agreement between both was excellent in all cases showing a quadratic dependence with the distance to the inlet, as demonstrated in [19]. The results

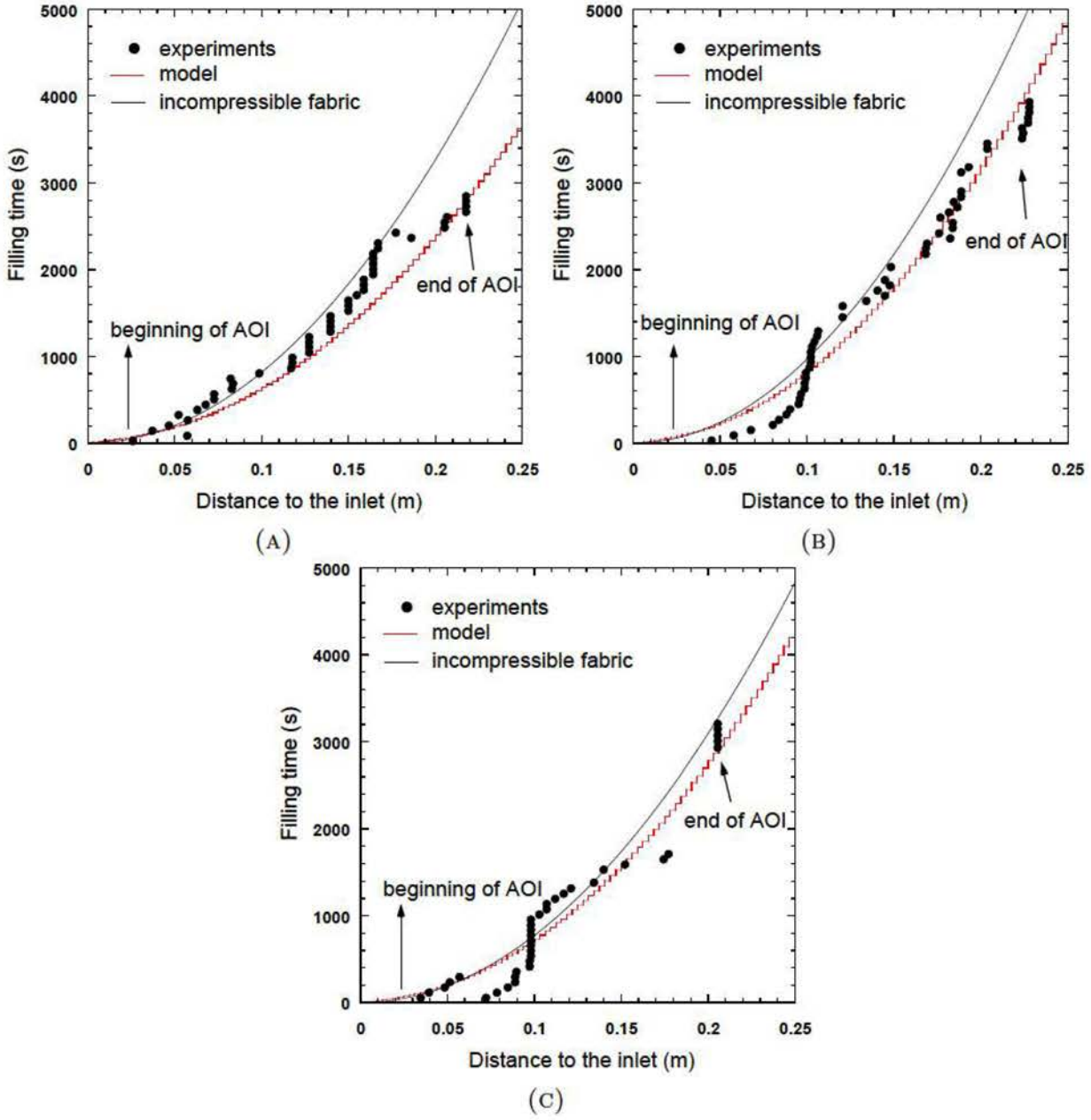

FIGURE 5.13: Evolution of the flow front with filling time. A) $[0°]_8$ B) $[0°]_4$ C) $[0°]_2$.

for the case of a rigid mould (no fabric compressibility) are also plotted for comparison purposes in this figure. In this case, the fabric permeability does not change with the fluid pressure and Darcy's equation is simplified to $\partial^2 p/\partial x^2 = 0$ (linear pressure variation between inlet and outlet). The filling time can be easily determined by direct integration yielding $t_{fill} = \mu L^2/2Kp_{atm}$ and the results in Figure 5.13 correspond to a fiber volume fraction

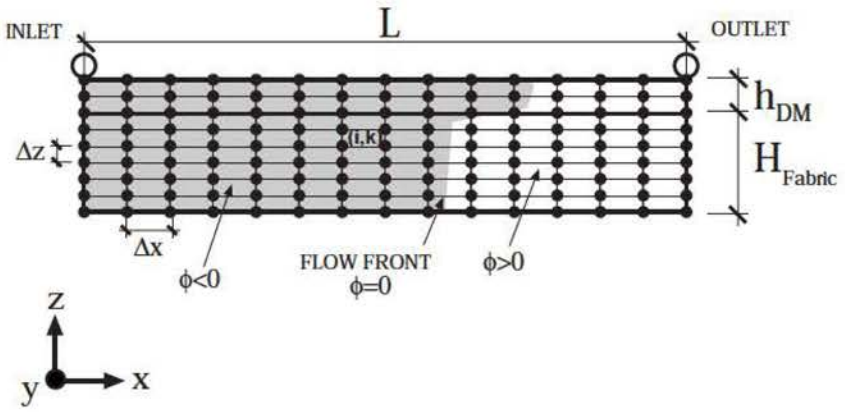

FIGURE 5.14: Discretization grid used in the models of the infusion tests with distribution medium.

in wet conditions (Section 3.2) at maximum pressure p_0. The longer filling times for the incompressible case are a result of the constant permeability of the fiber preform, which did not increase with time during the filling process due to the fiber spring-back.

5.3.2 Infusion experiments with distribution medium

Similarly to the previous case, the level set model was applied to determine the bag displacements and the pressure evolution during the infusion experiments when a distribution net is placed on the top of the E-glass laminate. As it was aforementioned, the distribution medium induces the easy flow of the fluid through the top surface of the laminate and the infiltration is a combination of in-plane and through-the-thickness flow. In this case, a representative cross section in the flow direction in the plane $x - z$ is modelled rather than the laminate mid-plane, Figure 5.9 b).

It should be mentioned that Darcy's equation (equation 5.6) is only valid when the fluid pressure profile is constant through the thickness of the laminate as in the case of in-plane flow propagation. In such case, the thickness experiences a uniform and homogeneous deformation along the z axis. However, the pressure profile along the z axis is not homogeneous in the case of the infusion experiments with distribution medium, and the fiber compaction

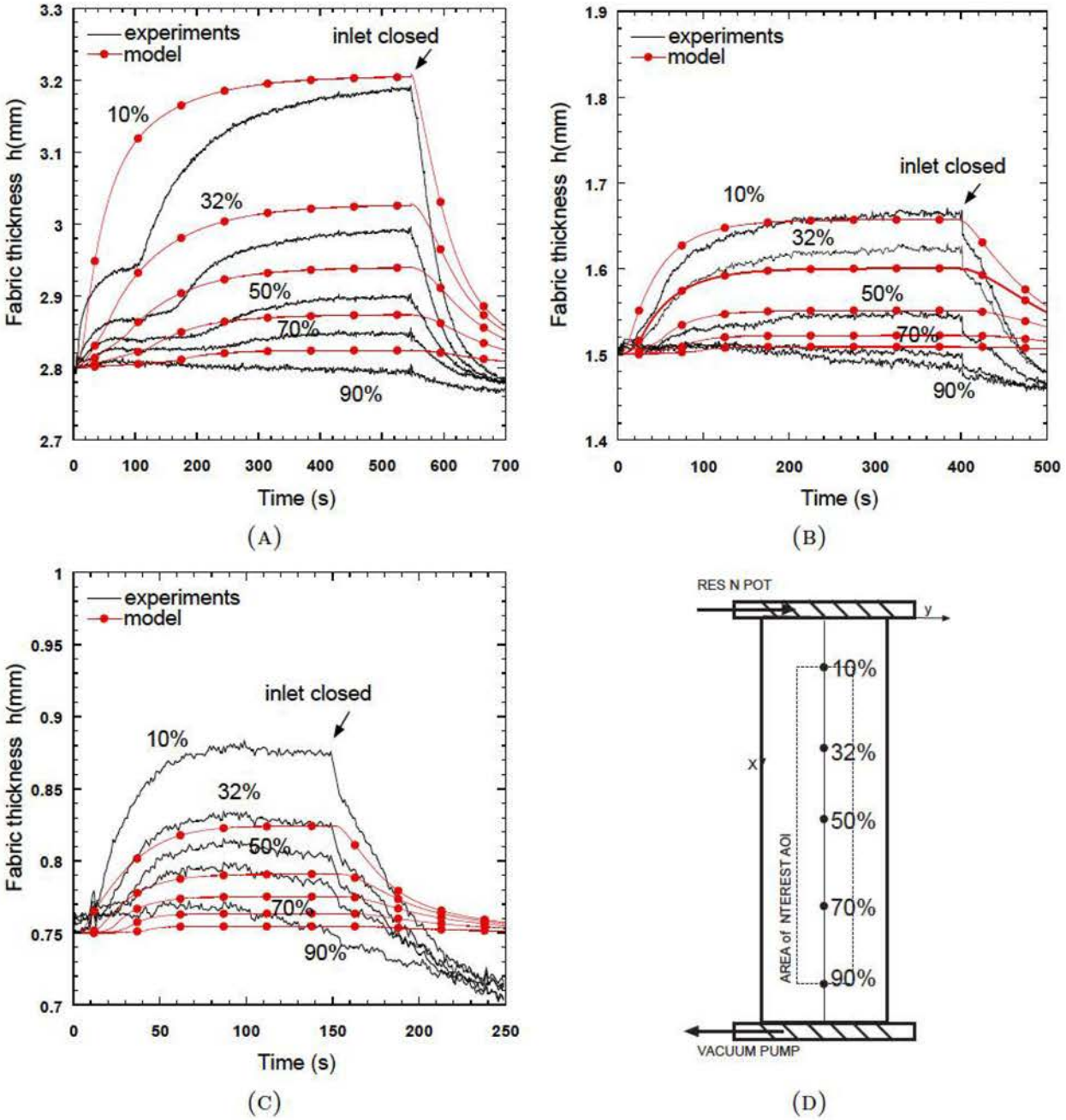

FIGURE 5.15: Evolution of the vacuum bag thickness with time during infusion at different positions of the strip located within the AOI. A) $[0°]_8$ B) $[0°]_4$ C) $[0°]_2$ D) Sketch of the panel with the different positions. Experiments with distribution medium.

velocity along z has to be introduced in the analysis. Kang *et al.* [23] suggested to modify the continuity equation 5.3 by the inclusion of an additional term to account for the fiber velocity along the through-the-thickness direction according to

$$\nabla \cdot \mathbf{v} = \frac{1}{V_f}\frac{\partial V_f}{\partial t} + \frac{1}{V_f}\frac{\partial V_f}{\partial z} v_z^f \tag{5.26}$$

where v_z^f is the fiber velocity in the z direction due to the compaction. In this thesis, the analysis was simplified and it was assumed that the fiber velocity during the compaction process was very low. Thus, the contribution of the term $v_z^f/V_f(\partial V_f/\partial z)$ was neglected in the analysis. The length of the cross section domain was equal to the one in the previous case L=250 mm while the thickness depended on the particular laminate configuration in the experiments: $[0°]_8$, $[0°]_4$ and $[0°]_2$ with the additional distribution medium. The thickness of the distribution medium $h_{DM} = 0.94$ mm was held constant following the experimental results presented in Section 3.2. The grid spacing in the flow direction was $\Delta x = 4.167$ mm while the corresponding spacing in the through-the-thickness direction Δz was adjusted to account for the different material properties, permeability and fiber bed compaction, of the laminate configuration (Δz_{8Ly}= 0.187 mm, Δz_{4Ly}= 0.122 mm and Δz_{2Ly}= 0.085 mm), Figure 5.14.

It should be indicated that the permeability factors and their dependence with respect to the fiber volume fraction in Chapter 3 were valid for in-plane flow $K_x(V_f)$. However, the simulations with distribution medium lead to the development of through-the-thickness flow and it is necessary to estimate the corresponding permeability factor in this direction $K_z(V_f)$. In the absence of more detailed data, the permeability factor $K_z(V_f)$ was assumed to be a constant fraction of the in-plane permeability. The ratio of the in-plane to the out-of-plane permeability factors K_x/K_z was 220, 350 and 1780 for the $[0°]_8$, $[0°]_4$ and $[0°]_2$ laminates, respectively. This ratio is consistent with the experimental results obtained for the filling time, as shown in Figure 3.8, and is also within the range reported by other authors [105–107].

The same boundary (prescribed pressure at the inlet and outlet and slip-free at the tool and bag surface) and initial conditions were imposed. The solution of the governing equations provides the fluid pressure field in the corresponding domain. It should be mentioned that neither the fluid flow evolution nor the pressure field are homogeneous as a result of the

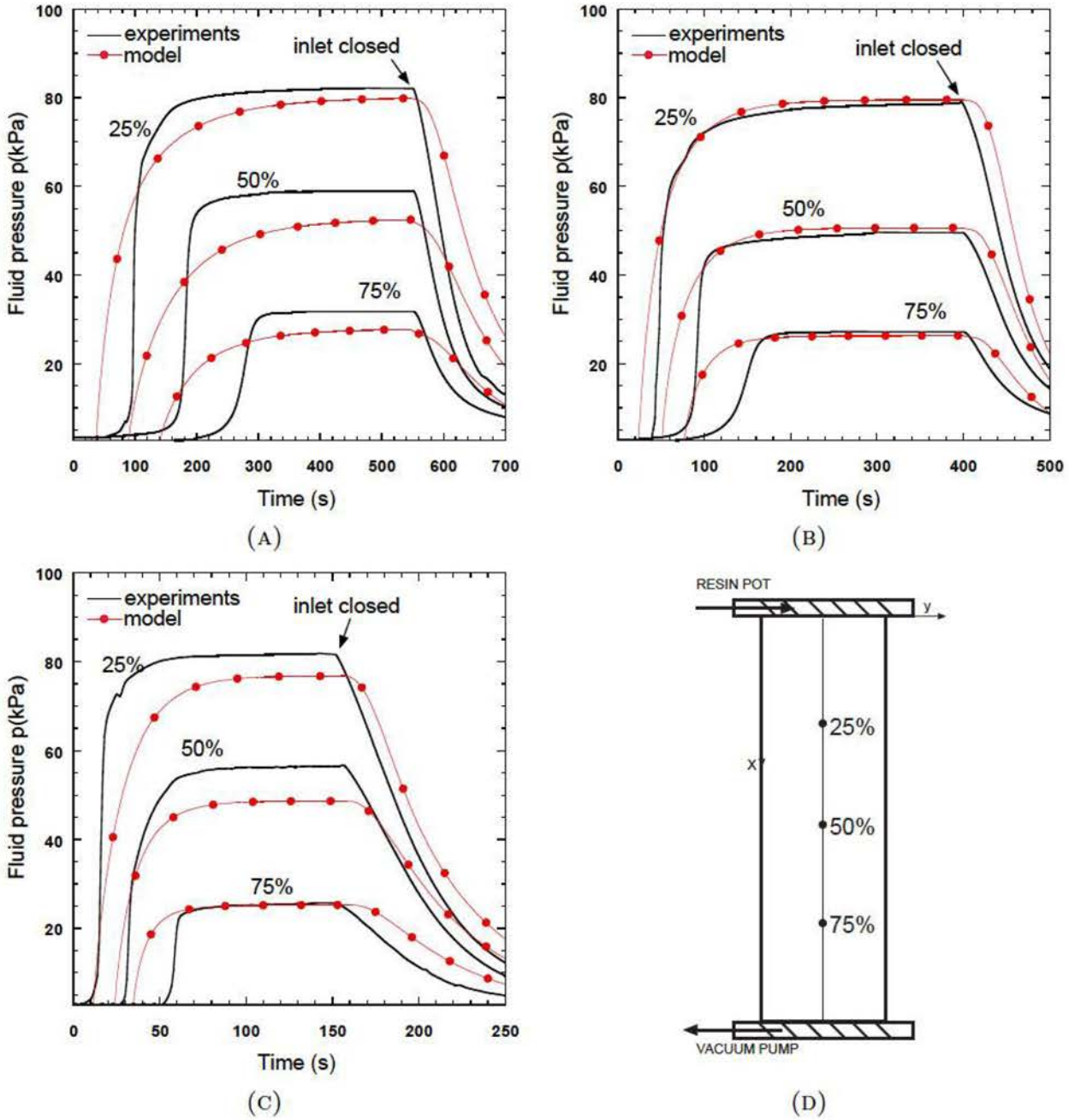

FIGURE 5.16: Evolution of fluid pressure at different positions of the strip located within the AOI. A) $[0°]_8$ B) $[0°]_4$ C) $[0°]_2$ D) Sketch of the panel with the different positions. Experiments with distribution medium.

different permeability factors. The fluid pressure field $p(x, z)$ as a function of time during the infiltration of the $[0°]_8$ fabric lay-up is plotted in Figure 5.17. The fluid propagated faster in the upper layer (see t=72 s in Figure 5.17) because of the highly permeable distribution

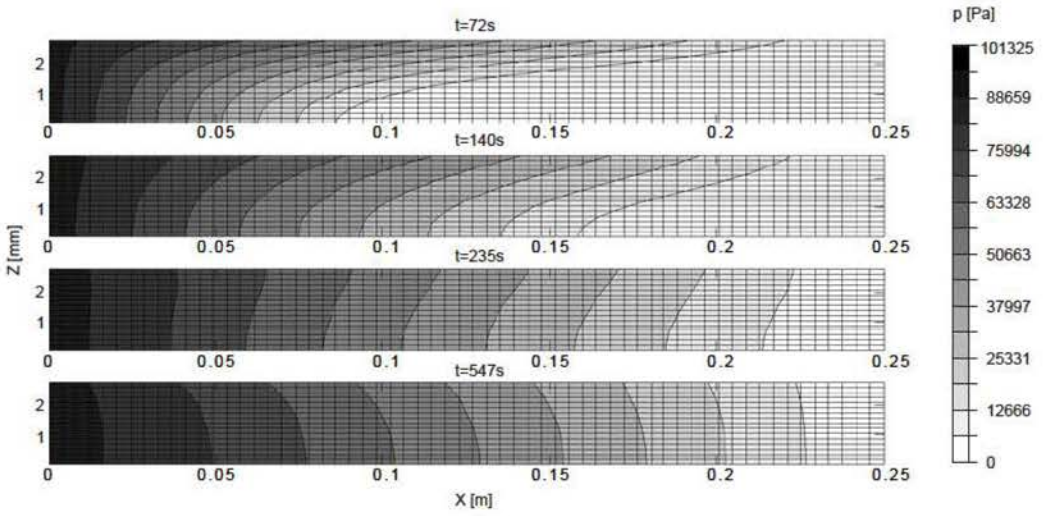

FIGURE 5.17: Time evolution of the fluid pressure field $p(x, z)$ with for the $[0°]_8$ laminate infused with distribution medium.

medium, leading to a mixed in-plane and through-the-thickness flow. Afterwards, the flow becomes more uniform in the thickness direction as well as the pressure profile (t= 547 s in Figure 5.17) after the fabric is completely impregnated. Very interestingly, this latter plot shows a slight change of the pressure profile in the thickness direction reversing the prior gradient towards the upper part of the laminate during the post filling operations. After closing the inlet gate, the fluid pressure tends to homogenize in the part and the distribution medium can act as a reservoir uptaking resin from the squeezed fabric.

Accordingly, the stress carried out by the fiber fabric is also inhomogeneous across the thickness and the deformation should be integrated at any given time to determine the vacuum bag displacements. The pressure profiles in the experiments across the thickness direction for a specific position within the infused length were sketched in Figure 5.18 a) and b) for infusions carried out with and without distribution medium, respectively. Therefore, the pressure profile $p(z, t)$ at a given position within the laminate length x is used to compute the local fabric deformation by direct integration over the thickness $\Delta h(x, t) = \int_0^{h_0} \varepsilon(p_{atm} - p(x, z, t))\, dz$. In this integration, the local fabric deformation ε was obtained from the fiber bed compaction tests carried out in wet conditions as it was showed (Chapter 3).

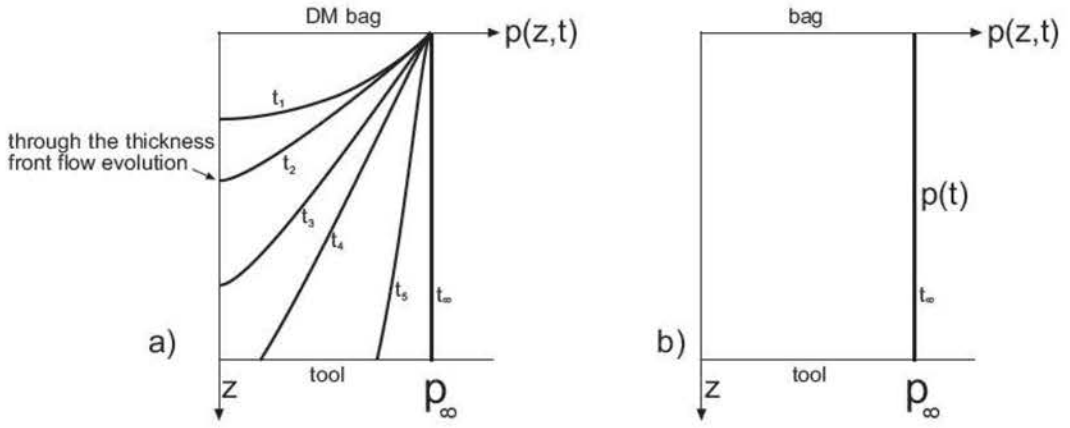

FIGURE 5.18: Sketch of the theoretical fluid pressure profiles in the thickness direction: a) with distribution medium, b) without distribution medium.

The predictions of the vacuum bag displacements at specific points along the infusion length are compared with the experimental results in Figure 5.15 for the different laminate configurations. Similar to the in-plane infusion results, the predictions of the bag displacements at specific positions along the infusion length were in good agreement with the experiments, specially for the thicker laminates ($[0°]_8$ and $[0°]_4$ in Figure 5.15 A) and B)). However, the model was not able to capture the bag deformation for the thinnest ($[0°]_2$ in Figure 5.15 C)) configuration. The experimental results of the time evolution of the fluid pressure at three different locations along the infusion length are compared with the simulations results in Figure 5.16 for the three laminate configurations. The agreement between simulation and experiments was remarkable again in terms of maximum pressure recorded by the sensors and its evolution. As it was already mentioned in simulations carried out without distribution medium, the lack of agreement with the experimental bag displacements can be probably attributed to the lack of representativity of the fiber bed compaction curves in the thinnest laminate configuration $[0°]_2$. Finally, the shape of the vacuum bag at different instants during the filling stage is shown in Figure 5.19 a) for these experiments. The contour plot of the increment in the fabric thickness, $\Delta h(x,t)$, was obtained by digital image correlation and is also plotted in Figure 5.19 b) for the same infusion times for comparison purposes.

As a concluding remark, the model was able to represent adequately the stress transfer

mechanisms in both experimental conditions, with and without distribution medium, and the pressure and bag displacements were in reasonable agreement with the corresponding experimental results. However, the model was not able to capture adequately the deformation of the fabric for the thinnest laminate configurations. This limitation has to be attributed to the lack of reliability of the wet fiber compaction tests for very thin laminates.

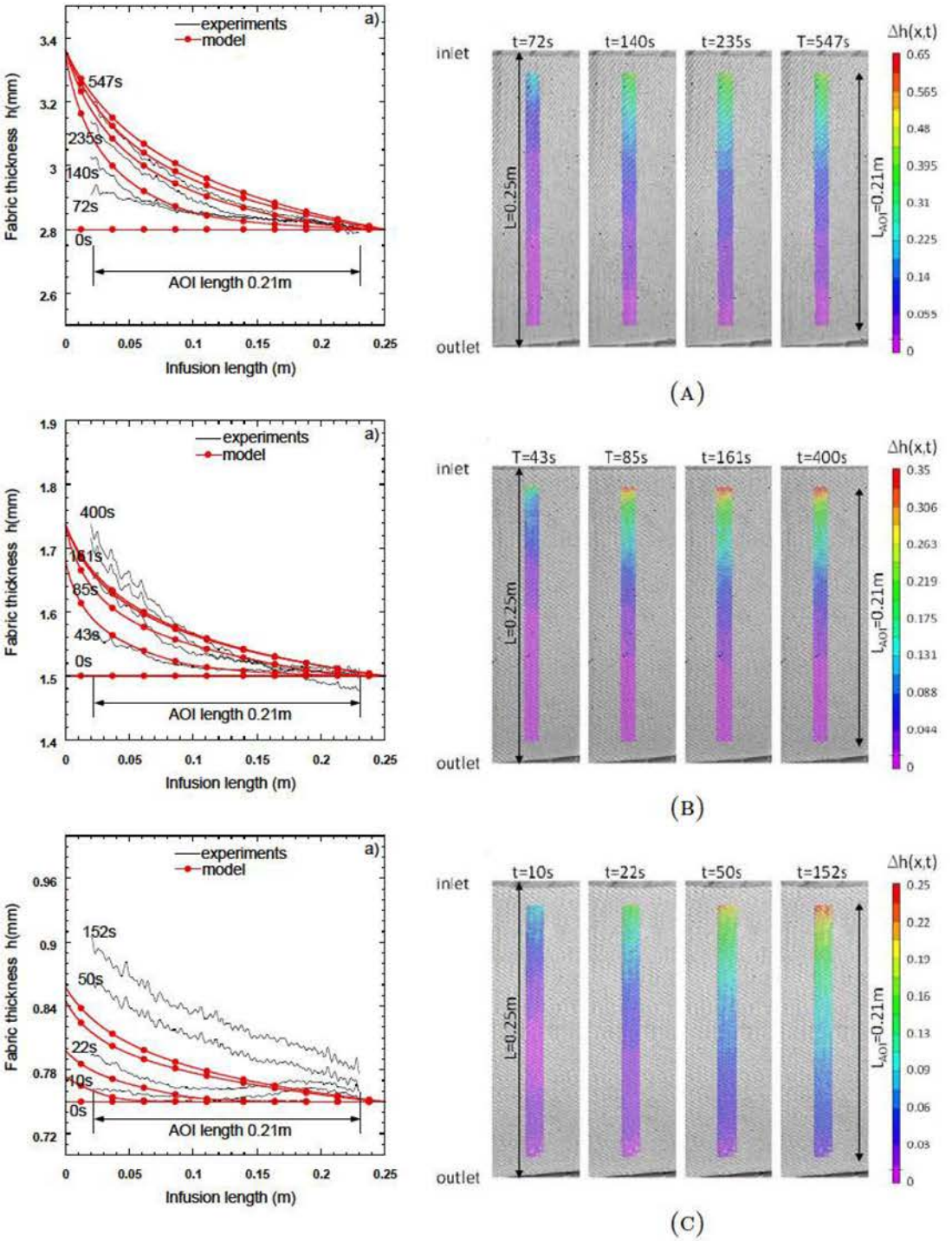

FIGURE 5.19: a) Evolution of the bag thickness profile along the infusion length within the AOI for different infusion times. b) Contour plot of the increment in the fabric thickness, $\Delta h(x,t)$, within the AOI for different infusion times. A) $[0°]_8$ B) $[0°]_4$ C) $[0°]_2$.

"The existence of reality is the most mysterious, most sublime, most surrealist thing of all"

Empordanès painter Salvador Dalí

Chapter 6

Conclusions and future work

Liquid molding techniques (and, particularly, vacuum-assisted resin infusion, VARI) are very promising strategies to reduce the large costs associated with autoclave processing to manufacture high performance polymer-matrix composites. Standard reinforcements used in composite manufacturing are formed by tows containing thousands of fibers in specific fabric architectures (unidirectional, woven, non-crimp, stitched, etc.), leading to microporosity (the free space in between individual fibers within the tow) and mesoporosity (the free space between tows). Viscous flow dominated by the resin pressure gradient takes place through the high permeable channels between adjacent fiber tows while tow impregnation perpendicular to the fiber is mainly driven by capillary forces. This dual-scale flow (micro-meso) is partially responsible for the generation of voids during liquid molding of composite parts because of the competition between viscous and capillary forces. Macrodefects, resulting from dry –or poorly impregnated– zones, appear when the resin flow reaches the outlet gate before completely filling the component. They are due to an inadequate distribution of the injection/infusion/venting ports in the component. In addition, microdefects (voids) can also appear, even if the part has been completely filled with resin during infusion. These voids and air entrapments reduce significantly the mechanical properties of the composite

and hinder the application of liquid molding in aerospace, sports and other sectors which require outstanding mechanical properties.

The investigations presented in this doctoral thesis were aimed at obtaining a deeper understanding of the physical mechanisms controlling resin flow during infiltration together with the development of modeling tools capable of simulating the complex mechanisms of resin flow and load transfer between matrix and fibers during infiltration. The main results and conclusions are summarized below.

6.1 Conclusions

- An experimental set-up has been designed and built to study resin flow during VARI in the laboratory under well controlled boundary and initial conditions. The set-up allows the use of a distribution medium on top of the fiber preform to account for in-plane and through-the thickness infiltration and includes several pressure gauges to monitor the fluid pressure in different locations time. Moreover, the evolution of the out-of-plane displacement of the vacuum bag (due to changes in the fabric compaction) was continuously measured by means of digital image correlation. The detailed information provided by this system (in terms of fluid pressure evolution, propagation of the flow front, fiber compaction, etc.) is critical to fully understand the mesoscopic flow as a function of the characteristics of the fluid, of the fiber preform and of the infiltration domain.

- *in situ* VARI experiments were carried out in the synchrotron beam to study the mechanisms of microfluid flow within a fiber tow by means of synchrotron X-ray computer tomography (SXCT) using an apparatus designed and built for this purpose. A single tow of E glass fibers was infused with a water and syrup blend in several steps by controlling the fluid volume delivered at the inlet needle and radiographies at different angles were taken after each step to reconstruct the three dimensional microstructure of the infiltrated tow. The high resolution of the SXCT images allows the detailed

reconstruction of individual fibers within the tow while the contrast between the different phases (air, fluid and fibers) was enough to track the fluid front position and shape as well as the void transport during infiltration. The ability of this technique to analyze the details of microfluid flow and void transport in composite materials was clearly established for the first time.

- The high resolution SXCT images showed an obtuse contact angles between the fluid and the fibers at the flow front. This behavior, which was opposed to the wetting contact angles measured in air, seemed to be a surface effect triggered in vacuum by the interaction between the fluid and the fiber sizing. One consequence of the phenomenon is that the capillary pressure acted as a drag force on the fluid flow. As a result, fluid flow was favored through areas with low fiber volume fraction which presented higher permeability and lower capillary forces. It was found that the complexity of the microflow depended markedly on the microstructure and the presence of convergent/divergent individual fiber trajectories played a significant role. Convergent fiber trajectories tend to arrest the fluid propagation by capillary forces and the detailed reconstruction of the fiber distribution allowed the interpretation of the flow progression in terms of the capillary pressure and permeability factors.

- The transport of small and large voids within the fiber tow was also assessed by means of SXCT. Small voids were transported along the tow direction through the empty spaces between individual fibers. They were trapped when the distance between fibers was below a critical value because the pressure gradient required to overcome the capillary pressure was too high. As a result, a large volume fraction of very small voids was trapped in the microstructure. The propagation of a large void spanning dozens of fibers was also observed in the experiments. In this case, the void migrated easily along the fiber tow driven by the vacuum pressure gradient. Very interestingly, the internal pressure of the void was large enough to produce significant fiber and bag movements during the void transport, leaving a trail of smaller voids in the wake.

- A level set based model was developed to simulate the fluid flow and fabric compaction during VARI of composite materials. Fluid infusion through the fiber preform was modeled using Darcy's equations for the fluid flow through a porous media, including the continuity condition. The stress partition between the fluid and the fiber bed was included by means of Terzaghi's effective stress theory, leading to a non-linear partial differential equation. This equation is only valid in the infused region and its necessary to separate both regions. This was achieved by introducing a level set function ϕ in the partial differential equation which is defined at any given time as the distance to the flow front. The partial differential equations were discretized and solved approximately using the finite differences method with a uniform grid discretization of the spatial domain. Darcy's equation was solved using a standard Euler method for the time integration and a central differences algorithm for the spatial integration. The time integration of the level set equation was approximated with the forward Euler method while the upwind algorithm was used for the spatial integration to account for the hyperbolic nature of the evolution equation.

- The model predictions were compared with experimental results of fluid flow in unidirectional E glass laminates with different thicknesses with and without distribution medium. The physical parameters of the model, including the fluid viscosity, the in-plane fabric permeability and the fiber bed compressibility, were also independently measured. The model results (in terms of fabric thickness, pressure and fluid front evolution) were in very good agreement with the experimental data in the case of infiltrations without distribution medium and thick laminates and validated the novel level set approach to model VARI. Discrepancies in the case of thin laminates were attributed to the lack of reliability of the fiber bed compaction tests for such thin laminates due to anomalous yarn nesting. The discrepancies between the numerical simulations and the experiments in the case of infiltration with distribution medium were attributed to the lack of reliable experimental values for the through-the-thickness permeability of the fabric and to neglecting the pressure gradient through the thickness (and, thus, the variation of the fiber compaction in this direction).

6.2 Future work

Taking into account the results achieved in this thesis, the following tasks are proposed for the future work:

- Develop an experimental set-up to measure the preform permeability in the through-the-thickness direction as well as its dependence with the fiber volume fraction.
- Exploit the *in situ* SXCT system to quantify the effect of the fiber spatial distribution within the fiber tow on the fluid flow and void transport along and perpendicular to the fibers. In addition, this experimental set-up can be used in the future to carry out "on the fly" SXCT experiments that can capture the influence of dynamic effects during infiltration.
- The equations governing of the infiltration long the through-the thickness direction should be modified to include the the pressure gradient through the thickness (and, thus, the variation of the fiber compaction in this direction).
- The kernel of the level set method can be used within the finite element method to simulate the VARI of components with complex geometries. In addition, thermo-chemical effects on the viscosity of the fluid due to the curing of the resin can be taken into account in this framework, including heat generation and heat transfer to provide a comprehensive simulation tool of VARI.

Bibliography

[1] K. K. Chawla. *Metal matrix composites*. Wiley Online Library, 2006.

[2] A. Mortensen and J. Llorca. Metal matrix composites. *Annual review of materials research*, 40:243–270, 2010.

[3] K. K. Chawla. *Ceramic matrix composites*. Springer, 1998.

[4] G. Savage. *Carbon-carbon composites*. Springer Science & Business Media, 1993.

[5] H. Soebroto, C. Pastore, F. KO, and T. Hager. Engineering design of braided structural fiberglass composites. In *International SAMPE Symposium and Exhibition, 35 th, Anaheim, CA*, pages 687–696, 1990.

[6] F. C. Campbell Jr. *Manufacturing technology for aerospace structural materials*. Elsevier, 2011.

[7] F. AL. Dullien. *Porous media: fluid transport and pore structure*. Academic press, 1991.

[8] H. Darcy. *Les fontaines publiques de la ville de Dijon*. 1856.

[9] P. C. Carman. Fluid flow through granular beds. *Transactions, Institution of Chemical Engineers*, 15:150–166, 1937.

[10] B. R. Gebart. Permeability of unidirectional reinforcements for RTM. *Journal of Composite Materials*, 26(8):1100–1133, 1992.

[11] T. G. Gutowski, T. Morigaki, and Z. Cai. The consolidation of laminate composites. *Journal of Composite Materials*, 21(2):172–188, 1987.

[12] T. G. Gutowski. Resin flow/fiber deformation model for composites. *SAMPE Quartiles*, 16(4), 1985.

[13] R. Gauvin and F. Trochu. Comparison between numerical and experimental results for mold filling in resin transfer molding. *Plastics, Rubber and Composites Processing and Applications*, 19:151–157, 1993.

[14] M. Um and W. I. Lee. A study on the mold filling process in resin transfer molding. *Polymer Engineering and Science*, 31(11):765–771, 1991.

[15] C. A. Fracchia, J. Castro, and C. L. Tucker. A finite element/control volume simulation of resin transfer mold filling. In *Proceedings of the American society for composites, fourth technical conference*, pages 157–166, 1989.

[16] H. P. Wang and H. S. Lee. Numerical techniques for free and moving boundary problems. *Fundamentals of Computer Modeling for Polymer Processing*, pages 340–401, 1989.

[17] ESIS. PAM-RTM, 2015.

[18] M. V. Bruschke and S. G. Advani. A finite element/control volume approach to mold filling in anisotropic porous media. *Polymer Composites*, 11(6):398–405, 1990.

[19] N. C. Correia, F. Robitaille, A. C. Long, C. D. Rudd, P. Šimáček, and S. G. Advani. Analysis of the vacuum infusion moulding process: I. analytical formulation. *Composites Part A: Applied Science and Manufacturing*, 36(12):1645–1656, 2005.

[20] A. Hammami and B. R. Gebart. Analysis of the vacuum infusion molding process. *Polymer Composites*, 21(1):28–40, 2000.

[21] A. E. Scheidegger. Physics of flow through porous media. In *Physics of flow through porous media*. University of Toronto, 1963.

[22] K. Han, S. Jiang, C. Zhang, and B. Wang. Flow modeling and simulation of scrimp for composites manufacturing. *Composites Part A: Applied Science and Manufacturing*, 31(1):79–86, 2000.

[23] M. K. Kang, W. I. Lee, and H. T. Hahn. Analysis of vacuum bag resin transfer molding process. *Composites Part A: Applied Science and Manufacturing*, 32(11):1553–1560, 2001.

[24] R. Davé. A unified approach to modeling resin flow during composite processing. *Journal of Composite Materials*, 24(1):22–41, 1990.

[25] P. Simacek, D. Heider, J. W. Gillespie Jr, and S. Advani. Post-filling flow in vacuum assisted resin transfer molding processes: Theoretical analysis. *Composites Part A: Applied Science and Manufacturing*, 40(6):913–924, 2009.

[26] Karl T. *Theoretical Soil Mechanics*. John Wiley and Sons, Inc, 1943.

[27] M. A. Biot. General theory of three-dimensional consolidation. *Journal of Applied Physics*, 12:155–164, 1941.

[28] T. G. Gutowski, T. Morigaki, and C. Zhong. The consolidation of laminate composites. *Journal of Composite Materials*, 21(2):172–188, 1987.

[29] T. G. Gutowski, Z. Cai, S. Bauer, D. Boucher, J. Kingery, and S. Wineman. Consolidation experiments for laminate composites. *Journal of Composite Materials*, 21(7): 650–669, 1987.

[30] R. Dave, J. L. Kardos, and M. P. Duduković. A model for resin flow during composite processing part 2: Numerical analysis for unidirectional graphite/epoxy laminates. *Polymer Composites*, 8(2):123–132, 1987.

[31] Y. R. Kim, S. P. McCarthy, and J. P. Fanucci. Compressibility and relaxation of fiber reinforcements during composite processing. *Polymer Composites*, 12(1):13–19, 1991.

[32] S. Hernández, F. Sket, C. González, and J. LLorca. Optimization of curing cycle in carbon fiber-reinforced laminates: void distribution and mechanical properties. *Composites Science and Technology*, 85:73–82, 2013.

[33] S. Hernández, F. Sket, J. M. Molina-Aldaregui, C. González, J. LLorca, et al. Effect of curing cycle on void distribution and interlaminar shear strength in polymer-matrix composites. *Composites Science and Technology*, 71(10):1331–1341, 2011.

[34] E. Ruiz, V. Achim, S. Soukane, F. Trochu, and J. Bréard. Optimization of injection flow rate to minimize micro/macro-voids formation in resin transfer molded composites. *Composites Science and Technology*, 66(3):475–486, 2006.

[35] J. S. U. Schell, M. Deleglise, C. Binetruy, P. Krawczak, and P. Ermanni. Numerical prediction and experimental characterisation of meso-scale-voids in liquid composite moulding. *Composites Part A: Applied Science and Manufacturing*, 38(12):2460–2470, 2007.

[36] J. M. Lawrence, V. Neacsu, and S. G. Advani. Modeling the impact of capillary pressure and air entrapment on fiber tow saturation during resin infusion in lcm. *Composites Part A: Applied Science and Manufacturing*, 40(8):1053–1064, 2009.

[37] N. Kuentzer, P. Simacek, S. G. Advani, and S. Walsh. Correlation of void distribution to {VARTM} manufacturing techniques. *Composites Part A: Applied Science and Manufacturing*, 38(3):802 – 813, 2007.

[38] N. Patel and L. J. Lee. Modeling of void formation and removal in liquid composite molding. Part I: Wettability analysis. *Polymer Composites*, 17(1):96–103, 1996.

[39] N. Patel and L. J. Lee. Modeling of void formation and removal in liquid composite molding. Part II: Model development and implementation. *Polymer Composites*, 17 (1):104–114, 1996.

[40] N. Patel and L. J. Lee. Effects of fiber mat architecture on void formation and removal in liquid composite molding. *Polymer Composites*, 16(5):386–399, 1995.

[41] C. H. Park, A. Lebel, A. Saouab, J. Bréard, and W. I. Lee. Modeling and simulation of voids and saturation in liquid composite molding processes. *Composites Part A: Applied Science and Manufacturing*, 42(6):658 – 668, 2011.

[42] C. Ravey, E. Ruiz, and F. Trochu. Determination of the optimal impregnation velocity in resin transfer molding by capillary rise experiments and infrared thermography. *Composites Science and Technology*, 99(0):96 – 102, 2014.

[43] Y. K. Hamidi, L. Aktas, and M. C. Altan. Formation of microscopic voids in resin transfer molded composites. *Journal of Engineering Materials and Technology*, 126(0): 420–426, 2004.

[44] Q. Govignon, S. Bickerton, J. Morris, and P. A. Kelly. Full field monitoring of the resin flow and laminate properties during the resin infusion process. *Composites Part A: Applied Science and Manufacturing*, 39(9):1412–1426, 2008.

[45] V. Tiwari, M. A. Sutton, and S. R. McNeill. Assessment of high speed imaging systems for 2d and 3d deformation measurements: methodology development and validation. *Experimental Mechanics*, 47(4):561–579, 2007.

[46] W. Tong. An evaluation of digital image correlation criteria for strain mapping applications. *Strain*, 41(4):167–175, 2005.

[47] W. H. Peters and W. F. Ranson. Digital imaging techniques in experimental stress analysis. *Optical Engineering*, 21(3):213427–213427, 1982.

[48] Z. L. Kahn-Jetter and T. C. Chu. Three-dimensional displacement measurements using digital image correlation and photogrammic analysis. *Experimental Mechanics*, 30(1): 10–16, 1990.

[49] DIC-3D. Correlated solutions, 2010. `http://www.correlatedsolutions.com`.

[50] G. N. Hounsfield. Apparatus for examining a body by radiation such as x or gamma radiation, March 16 1976. US Patent 3,944,833.

[51] L. Salvo, P. Cloetens, E. Maire, S. Zabler, J. J. Blandin, J. Y. Buffière, W. Ludwig, E. Boller, D. Bellet, and C. Josserond. X-ray micro-tomography an attractive characterisation technique in materials science. *Nuclear Instruments and Methods in Physics Research Section B: Beam Interactions with Materials and Atoms*, 200:273–286, 2003.

[52] E. Maire, J. Y. Buffiere, L. Salvo, J. J. Blandin, W. Ludwig, and J. M. Letang. On the application of x-ray microtomography in the field of materials science. *Advanced Engineering Materials*, 3(8):539–546, 2001.

[53] C.D. Williams, S.M. Grove, and J. Summerscales. The compression response of fibre-reinforced plastic plates during manufacture by the resin infusion under flexible tooling method. *Composites Part A: Applied Science and Manufacturing*, 29(1–2):111 – 114, 1998.

[54] B. W. Grimsley, H. Pascal, S. Xiaolan, R. Cano, A. Loss, and P. R. Byron. Flow and compaction during the vacuum assisted resin transfer moulding process. *Int SAMPE Tech Conf*, 33:141–153, 2001.

[55] L. Fang, J. Jiang, J. Wang, C. Deng, D. Li, and F. Liu. Effect of layer shift on the out-of-plane permeability of $0°/90°$ noncrimp fabrics. *Journal of Reinforced Plastics and Composites*, 2014.

[56] L. Fang, J. Jiang, J. Wang, and C. Deng. Effect of nesting on the out-of-plane permeability of unidirectional fabrics in resin transfer molding. *Applied Composite Materials*, 22(3):231–249, 2015.

[57] C. A. Grattoni, H. H. Al-Sharji, C. Yang, A. H. Muggeridge, and R. W. Zimmerman. Rheology and permeability of crosslinked polyacrylamide gel. *Journal of colloid and interface science*, 240(2):601–607, 2001.

[58] A. C. Rust and M. Manga. Bubble shapes and orientations in low re simple shear flow. *Journal of Colloid and Interface Science*, 249(2):476–480, 2002.

[59] H. C. Stadtfeld, M. Erninger, S. Bickerton, and S. G. Advani. An experimental method to continuously measure permeability of fiber preforms as a function of fiber volume fraction. *Journal of Reinforced Plastics and Composites*, 21(10):879–899, 2002.

[60] J. B. Alms, N. Correia, S. G. Advani, and E. Ruiz. Experimental procedures to run longitudinal injections to measure unsaturated permeability of lcm reinforcements. *Permeability Measurement Standard, Permeability Benchmark II, http://cchp. meca. polymtl. ca/permeabilityBenchmarkII html*, 2010.

[61] B. Yenilmez, M. Senan, and S. E. Murat. Variation of part thickness and compaction pressure in vacuum infusion process. *Composites Science and Technology*, 69(11-12): 1710–1719, 2009.

[62] S. Bickerton and S. G. Advani. Characterization and modeling of race-tracking in liquidcomposite molding processes. *Composites Science and Technology*, 59(15):2215–2229, 1999.

[63] A. W. Chan and R. J. Morgan. Modeling racetracking effects in liquid composite molding. In *Proceedings of the 1997 ASME International Mechanical Engineering Congress and Exposition*, volume 79, pages 361–367, 1997.

[64] Q. Govignon, S. Bickerton, and P. A. Kelly. Simulation of the reinforcement compaction and resin flow during the complete resin infusion process. *Composites Part A: Applied Science and Manufacturing*, 41(1):45–57, 2010.

[65] D. Yuexin, T. Zhaoyuan, Z. Yan, and S. Jing. Compression responses of preform in vacuum infusion process. *Chinese Journal of Aeronautics*, 21(4):370–377, 2008.

[66] B. Chen and T. W. Chou. Compaction of woven-fabric preforms: nesting and multilayer deformation. *Composites Science and Technology*, 60(12):2223–2231, 2000.

[67] B. Yenilmez, M. Senan, and E. Murat Sozer. Variation of part thickness and compaction pressure in vacuum infusion process. *Composites Science and Technology*, 69 (11):1710–1719, 2009.

[68] N. Pearce and J. Summerscales. The compressibility of a reinforcement fabric. *Composites Manufacturing*, 6(1):15–21, 1995.

[69] J. Vilà, F. Sket, F. Wilde, G. Requena, C. González, and J. LLorca. An in situ investigation of microscopic infusion and void transport during vacuum-assisted infiltration by means of x-ray computed tomography. *Composites Science and Technology*, 119: 12–19, 2015.

[70] N. Kuentzer, P. Simacek, S. G. Advani, and S. Walsh. Permeability characterization of dual scale fibrous porous media. *Composites Part A: Applied Science and Manufacturing*, 37(11):2057 – 2068, 2006.

[71] T. Nowak and J. H. Chun. Optical measurement of preform impregnation in resin transfer molding. In *Symposium I – High-Performance Polymers and Polymer Matrix Composites*, volume 305 of *MRS Proceedings*, 1 1993.

[72] Y. Chen, H. T. Davis, and C. W. Macosko. Wetting of fiber mats for composites manufacturing: I. visualization experiments. *AIChE Journal*, 41(10):2261–2273, 1995.

[73] Y. Chen, C. W. Macosko, and H. T. Davis. Wetting of fiber mats for composites manufacturing: Ii. air entrapment model. *AIChE Journal*, 41(10):2274–2281, 1995.

[74] L. Francois, F. Amir Ershad, R. Edu, and T. Francois. Experimental characterization by fluorescence of capillary flows in the fiber tows of engineering fabrics. *Open Journal of Inorganic Non-metallic Materials*, 2012, 2012.

[75] J. Vilà, C. González, and J. LLorca. A level set approach for the analysis of flow and compaction during resin infusion in composite materials. *Composites Part A: Applied Science and Manufacturing*, 67(0):299 – 307, 2014.

[76] V. Neacsu, A. Abu Obaid, and S. G. Advani. Spontaneous radial capillary impregnation across a bank of aligned micro-cylinders. Part II: Experimental investigations. *International Journal of Multiphase Flow*, 32(6):677 – 691, 2006.

[77] N. Gupta and R. Sundaram. Fiber optic sensors for monitoring flow in vacuum enhanced resin infusion technology (verity) process. *Composites Part A: Applied Science and Manufacturing*, 40(8):1065 – 1070, 2009.

[78] C. Lekakou, S. Cook, Y. Deng, T. W. Ang, and G. T. Reed. Optical fibre sensor for monitoring flow and resin curing in composites manufacturing. *Composites Part A: Applied Science and Manufacturing*, 37(6):934 – 938, 2006.

[79] S. Thomas, C. Bongiovanni, and S. R. Nutt. In situ estimation of through-thickness resin flow using ultrasound. *Composites Science and Technology*, 68(15-16):3093 – 3098, 2008.

[80] T. Stoven, F. Weyrauch, P. Mitschang, and M. Neitzel. Continuous monitoring of three-dimensional resin flow through a fibre preform. *Composites Part A: Applied Science and Manufacturing*, 34(6):475 – 480, 2003.

[81] J. Leisen and H. W. Beckham. Quantitative magnetic resonance imaging of fluid distribution and movement in textiles. *Textile Research Journal*, 71(12):1033–1045, 2001.

[82] V. Neacsu, J. Leisen, H.W. Beckham, and S.G. Advani. Use of magnetic resonance imaging to visualize impregnation across aligned cylinders due to capillary forces. *Experiments in Fluids*, 42(3):425–440, 2007.

[83] A. Endruweit, P. Glover, K. Head, and A. C. Long. Mapping of the fluid distribution in impregnated reinforcement textiles using magnetic resonance imaging: Application and discussion. *Composites Part A: Applied Science and Manufacturing*, 42(10):1369 – 1379, 2011.

[84] A. Endruweit, P. Glover, K. Head, and A. C. Long. Mapping of the fluid distribution in impregnated reinforcement textiles using magnetic resonance imaging: Methods and issues. *Composites Part A: Applied Science and Manufacturing*, 42(3):265 – 273, 2011.

[85] J. Bréard, A. Saouab, and G. Bouquet. Dependence of the reinforcement anisotropy on a three dimensional resin flow observed by x-ray radioscopy. *Journal of Reinforced Plastics and Composites*, 18(9):814–826, 1999.

[86] F. Sket, A. Enfedaque, C. Alton, C. González, J.M. Molina-Aldareguia, and J. Llorca. Automatic quantification of matrix cracking and fiber rotation by x-ray computed tomography in shear-deformed carbon fiber-reinforced laminates. *Composites Science and Technology*, 90(0):129 – 138, 2014.

[87] R. Seltzer, C. González, R. Muñoz, J. LLorca, and T. Blanco-Varela. X-ray microtomography analysis of the damage micromechanisms in 3d woven composites under low-velocity impact. *Composites Part A: Applied Science and Manufacturing*, 45(0): 49 – 60, 2013.

[88] T. Centea and P. Hubert. Measuring the impregnation of an out-of-autoclave prepreg by micro-ct. *Composites Science and Technology*, 71(5):593 – 599, 2011.

[89] T. Centea and P. Hubert. Modelling the effect of material properties and process parameters on tow impregnation in out-of-autoclave prepregs. *Composites Part A: Applied Science and Manufacturing*, 43(9):1505 – 1513, 2012.

[90] S. Hernández, F. Sket, J.M. Molina-Aldareguía, C. González, and J. LLorca. Effect of curing cycle on void distribution and interlaminar shear strength in polymer-matrix composites. *Composites Science and Technology*, 71(10):1331 – 1341, 2011.

[91] S. Hernández, F. Sket, C. González, and J. LLorca. Optimization of curing cycle in carbon fiber-reinforced laminates: Void distribution and mechanical properties. *Composites Science and Technology*, 85(0):73 – 82, 2013.

[92] F. LeBel, A. E. Fanaei, E. Ruiz, and F. Trochu. Experimental characterization by fluorescence of capillary flows in dual-scale engineering fabrics. *Textile Research Journal*, 2013.

[93] K. E. Scher. *Comparison of wicking and single filament techniques for determining contact angles*. 1983.

[94] M. Li, S. Wang, Y. Gu, Z. Zhang, Y. Li, and K. Potter. Dynamic capillary impact on longitudinal micro-flow in vacuum assisted impregnation and the unsaturated permeability of inner fiber tows. *Composites Science and Technology*, 70:1628–1636, 2010.

[95] J. Verrey, V. MIchaud, and J. A. E. Manson. Dynamic capillary effects in liquid composite moulding with non-crimp fabrics. *Composites: Part A*, 37:92–102, 2006.

[96] V. M. Karbhari and G. R. Palmese. Sizing related kinetic and flow considerations in the resin infusion of composites. *Journal of Materials Science*, 32(21):5761–5774, 1997.

[97] K. J. Ahn, J. C. Seferis, and J. C. Berg. Simultaneous measurements of permeability and capillary pressure of thermosetting matrices in woven fabric reinforcements. *Polymer Composites*, 12(3):146–152, 1991.

[98] M. P. Krishna and G. A. Suresh. Wicking across a fiber-bank. *Journal of Colloid and Interface Science*, 183(1):100 – 110, 1996.

[99] T. S. Lundstrom. Bubble transport through constricted capillary tubes with application to resin transfer molding. *Polymer Composites*, 17(6):770–779, 1996.

[100] J. A. Sethian. *Level Set Methods and Fast Marching Methods: Evolving Interfaces in Computational Geometry, Fluid Mechanics, Computer Vision, and Materials Science*. Cambridge Monographs on Applied and Computational Mathematics. Cambridge University Press, 1999.

[101] S. Osher and J. A. Sethian. Fronts propagating with curvature-dependent speed: algorithms based on hamilton-jacobi formulations. *Journal of Computational Physics*, 79(1):12–49, 1988.

[102] P. Šimáček, D. Heider, J. J. W. Gillespie, and S. G. Advani. Post-filling flow in vacuum assisted resin transfer molding processes: Theoretical analysis. *Composites Part A: Applied Science and Manufacturing*, 40:913–924, 2009.

[103] M. Sussman, P. Smereka, and S. Osher. A level set approach for computing solutions to incompressible two-phase flow. *Journal of Computational Physics*, 114(1):146–159, 1994.

[104] D. Hartmann, M. Meinke, and W. Schröder. Differential equation based constrained reinitialization for level set methods. *J. Computational Physics.*, 227(14):6821–6845, 2008.

[105] A. Gokce, M. Chohra, S. G. Advani, and S. M. Walsh. Permeability estimation algorithm to simultaneously characterize the distribution media and the fabric preform in vacuum assisted resin transfer molding process. *Composites Science and Technology*, 65(14):2129–2139, 2005.

[106] V. Calado and A. Suresh. Effective average permeability of multi-layer preforms in resin transfer molding. *Composites Science and Technology*, 56(5):519 – 531, 1996.

[107] D. Heider, P. Simacek, A. Dominauskas, H. Deffor, A. Suresh, and J.W. Gillespie. Infusion design methodology for thick-section, low-permeability preforms using interlaminar flow media. *Composites Part A: Applied Science and Manufacturing*, 38(2): 525 – 534, 2007.